الجمهورية الجزائرية الديمقراطية الشعبية

People's Democratic Republic of Algeria

Ministry of Higher Education and Scientific Research

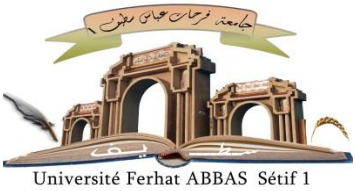

FERHAT ABBAS UNIVERSITY SETIF 1

INSTITUTE OF OPTICS AND PRECISION MECHANICS

THESIS

Presented to the Precision Mechanics Department

For obtaining the diploma of:

DOCTORATE

Domain: Science and Technology

Field: Optics and Precision Mechanics **Specialty:** Applied Mechanics

By

TAIEB Kahina

THEME

Parametric Study of Precision Abrasive Machining Processes for Ultra-Precise Finishing

Defended on 19/07/2025, In front of the jury :

NOM Prénom	**Professor**	**Ferhat Abbas University Setif 1**	**President**
BELKHIR Nabil	**Professor**	**Ferhat Abbas University Setif 1**	**Supervisor**
BIZARRI Gregory	**Professor**	**Cranfield University UK**	**Co-supervisor**
BENHIZIA Abdennour	**Professor**	**University of Batna 2**	**Examinator**
HAMDI Amine	**MCA**	**University of Tissemssilt**	**Examinator**

Dedication

In the name of Allah, the Most Gracious, the Most Merciful,
All praise and thanks are due to Allah alone, whose infinite mercy and guidance have carried me through every challenge and blessed me with the strength to reach this milestone.

الحمد لله الذي هدانا لهذا وما كنا لنهتدي لولا أن هدانا الله

I humbly dedicate this work to the two most precious souls in my life, my beloved parents:
To my father, **Taieb Khider**, whose unwavering strength, boundless patience, and endless sacrifices have been my shelter and my guide. Your quiet determination and steadfast belief in me have been the pillars on which I have built my dreams. Without your love and support, none of this would have been possible.
To my mother, **Diab Chahrazed**, whose tenderness, endless prayers, and unconditional love have been my light in the darkest times. Your nurturing heart and selfless spirit have taught me resilience and kindness, shaping the person I am today. I am forever grateful for your presence in my life.

To my cherished sisters, **Dr. Imane** and **Romaissa**,
your encouragement and faith have lifted me higher than words can express. I am blessed to walk this journey with you both beside me, and I pray for your happiness and success always.

I also extend my heartfelt thanks to their devoted husbands, **Haouam Zakaria** and, **Stambouli Fateh**
and their beautiful children, **Racim**, **Aline**, and **Bayram**. Your joy enriches our family and gives me happiness when I needed it most.

Finally, I take a moment to acknowledge myself, for the perseverance, courage, and unwavering spirit that carried me through the long nights and difficult days.
This achievement is not only a testament to my effort but a reflection of the love and support that surrounds me from my family.

Acknowledgement

I would like to express my profound gratitude to my supervisor, **Professor BELKHIR Nabil**, whose exceptional mentorship, unwavering patience, and constant encouragement have been the cornerstone of this research. His insightful guidance, constructive feedback, and deep expertise have profoundly shaped this work. Without his invaluable support and trust, completing this thesis would not have been possible.

I am deeply thankful to my co-supervisor, **Professor BIZARRI Gregory**, for warmly welcoming me to Cranfield University in United Kingdom and generously hosting me within his distinguished center and research group. His expert advice, encouragement, and the stimulating research environment he fostered have greatly enriched my academic experience and contributed immensely to the advancement of this project.

My sincere thanks also go to my esteemed colleague, **Dr. KHANNAB Abdelghani**, whose generous help, technical support, and collaborative spirit were instrumental throughout this journey. His readiness to assist and insightful discussions have been of great benefit, and I am truly grateful for his professionalism. The thanks go also to the Laboratory of Mechanics of Structures and Materials at the University of Batna 2 for the support.

I am also sincerely grateful to **Dr. ROGERS Edith** and **Dr. GIUSCA Claudiu**, whose guidance and collaboration at the Surface Engineering Precision Centre in Cranfield University were invaluable. Their availability and expertise made a difference in the progression of my work. Warm thanks go to **POPE Steve** for his kind support and for making my daily life in Cranfield University easier and more enjoyable.

I also wish to express my sincere appreciation to the members of the jury, Professors **Pr. DJEDDOU Ferhat, Pr. BENHIZIA Abdennour** and **Pr. HAMDI Amine,** for accepting to evaluate this work and for the time, attention, and insightful remarks they will bring to the defense of this thesis.

Finally, I would also like to sincerely thank all my professors at the Institute of Optics and Precision Mechanics, both during my student years and throughout my doctoral studies. Their teachings, encouragement, and knowledge have been fundamental to my academic growth.

This page is blank, but like the late hours of work, its emptiness holds the weight of everything that led me here.

TABLE OF CONTENTS

LIST OF FIGURES

LIST OF TABLES

List of Abbreviations

UPP: Ultra-Precision Processes
UPM: Ultra-Precision Machining
CMP: Chemical Mechanical Polishing
MRF: Magneto-Rheological Finishing
AFF: Abrasive Flow Finishing
UV-DWS: Ultrasonic Vibration-Assisted Wire Sawing
ED-DWS: Electrical Discharge-Assisted Wire Sawing
EC-DWS: Electrochemical-Assisted Wire Sawing
SEM: Scanning Electron Microscope
CNC: Computer Numerical Control
CAM: Computer-Aided Manufacturing
MRR: Material Removal Rate
α-Al_2O_3: Alpha Alumina (aluminum oxide)
γ-Al_2O_3: Gamma Alumina (aluminum oxide)
ZrO_2: Zirconium Dioxide (Zirconia)
CeO_2: Cerium Dioxide (Ceria)
BGO: Bismuth Germanate ($Bi_4Ge_3O_{12}$)
µm: Micrometer
TEM: Transmission Electron Microscope
AFM: Atomic Force Microscopy
CdTe: Cadmium Telluride
CTR: Coincidence Timing Resolution
LOR: Line of Response
MRI: Magnetic Resonance Imaging
PET: Positron Emission Tomography
SSD: Subsurface Damage
TOF: Time of Flight
TOF-PET: Time-of-Flight Positron Emission Tomography
Ra: Average Roughness
Rq: Root Mean Square Roughness
Rz: Peak-to-Valley Height
EM-CCD: Electron-Multiplying Charge-Coupled Device
SiPM: Silicon Photomultiplier
LSO:Ce: Lutetium Oxyorthosilicate doped with Cerium
UV-VIS: Ultraviolet–Visible Spectroscopy
XRG: X-ray Generator
JH-2: Johnson-Holmquist II Model
FEM: Finite Element Method

GENERAL INTRODUCTION

1. Context

Ultra-precision machining (UPM) represents the frontier of advanced manufacturing, where tolerances and surface finishes approach nanometric scales. This field is critical in domains such as aerospace, optics, and medical imaging, where mechanical precision directly impacts system performance. Among the materials used in these areas, brittle single crystals like Bismuth Germanate ($Bi_4Ge_3O_{12}$ or BGO) are crucial because they have excellent functional properties.

BGO is widely employed as a scintillator material in high-resolution radiation detection, especially in Time-of-Flight Positron Emission Tomography (TOF-PET). However, its intrinsic brittleness, low toughness, and high hardness present significant challenges during machining and finishing. To address these issues, modern ultra-precision machining strategies are required, including advanced control systems for material removal, surface quality, and process optimization.

2. Problem Statement and Research Objectives

BGO possesses significant optical and scintillation properties; however, its processing is challenging due to a propensity for fracturing under mechanical stress. Attaining smooth, defect-free surfaces is crucial for enhancing light transmission and ensuring timing precision in TOF-PET detectors.

Moreover, while there is a substantial body of research on the behavior of brittle materials during machining, the particular response of BGO to ultra-precision cutting, polishing, and micromachining has not been thoroughly investigated. A comprehensive parametric study is essential to understand and control the brittle-to-ductile transition, optimize surface roughness, and assess machining damages.

This research investigates the impact of machining parameters on surface quality and defect formation in BGO, focusing on the challenges posed by its brittle nature. This research aims to measure surface roughness and the progression of damage throughout the different phases of sample preparation, ranging from initial cutting to final polishing.

The research includes a high-precision micromachining simulation using the Johnson-Holmquist II (JH-2) material model, validated by experimental data, to enhance the prediction of BGO's response under ultra-precision conditions.

3. Methodological Contributions

This study offers a deep and systematic analysis of the machining behavior of BGO single crystals in ultra-precision settings. The research focuses on creating a full experimental process, starting with the preparation of BGO samples by wire sawing and lapping, followed by a mechanical polishing. Key polishing parameters, such as grain size, pressure, and speed, systematically were evaluated to see their influence on final surface roughness. To ensure the polishing results were reliable and consistent, a statistical method was used. The link between surface roughness and optical transmittance was also investigated; results indicated that better polishing resulted in better light transmission, a key factor for TOF-PET detector performance.

This thesis includes a numerical simulation of the micromachining process, using the Johnson-Holmquist II (JH-2) constitutive model in Abaqus/Explicit in addition to the experimental work. The simulation offers comprehensive insights into the cutting forces, stress distributions, and fracture behavior of BGO under ultra-precision conditions, validated against experimental micro-milling data. This study combines experiments and computer simulations to greatly improve the understanding and management of ultra-precision machining processes for brittle crystal materials used in advanced optical and detection technologies.

This thesis comprises four chapters, structured as follows:

- Chapter I offers a foundational overview of ultra-precision processes, outlining machining principles, finishing techniques, and critical parameters that affect material removal and surface quality.
- Chapter II examines the behavior of brittle materials, particularly in relation to ultra-precision machining. This work discusses the theoretical and practical challenges associated with materials such as BGO, focusing on surface quality and removal mechanisms. Next, it addresses the requirements for high surface quality and its implications for applications such as TOF-PET.
- Chapter III presents the materials and methods employed in the research conducted for the thesis, detailing each step of the process.
- Chapter IV details the experimental results and initial machining processes of BGO single crystals. This includes wire sawing, lapping, and mechanical polishing, in addition to a comprehensive Taguchi-based study of polishing conditions, surface roughness curve interpretation and transmittance analysis.

- Chapter V discusses the advanced micromachining study of BGO, which has been modeled and validated using the Johnson-Holmquist II (JH-2) model. This study evaluates the impact of micromachining parameters on cutting behavior, stress distribution, and surface results via simulation and experimental data comparison.

The general conclusion encapsulates the findings and contributions of this research while also suggesting future avenues for enhancing machining protocols and simulation frameworks for brittle crystalline materials in high-performance applications.

CHAPTER I

OVERVIEW OF ULTRA-PRECISION PROCESSES

I.1. Introduction

This chapter presents the domain of ultra-precision processes (UPP), which are essential in contemporary manufacturing that demands strict tolerances and superior surface quality. These techniques are critical in sectors like aerospace, medical device manufacturing, and optical systems production, where even slight surface irregularities or dimensional deviations can undermine performance or reliability.

Ultra-precision machining (UPM) denotes a category of manufacturing processes that can attain sub-micron accuracy and nanometric surface finishes. The processes depend on sophisticated equipment, stable platforms, and specific chosen tools, in addition to stringent control of machining parameters including feed rate, depth of cut, and spindle speed. The aim is to reduce damage caused by machining while maintaining consistency and dimensional accuracy.

In conjunction with UPM, surface finishing techniques are frequently necessary to enhance the workpiece. These techniques serve to remove micro-scale imperfections and restore surface quality potentially compromised during prior machining stages.

This chapter presents the theoretical framework essential for comprehending the principles underlying ultra-precision machining and finishing. This section presents the primary concepts, technologies, and process variables that will be elaborated upon in subsequent chapters, especially concerning their application in the precision processing of brittle materials.

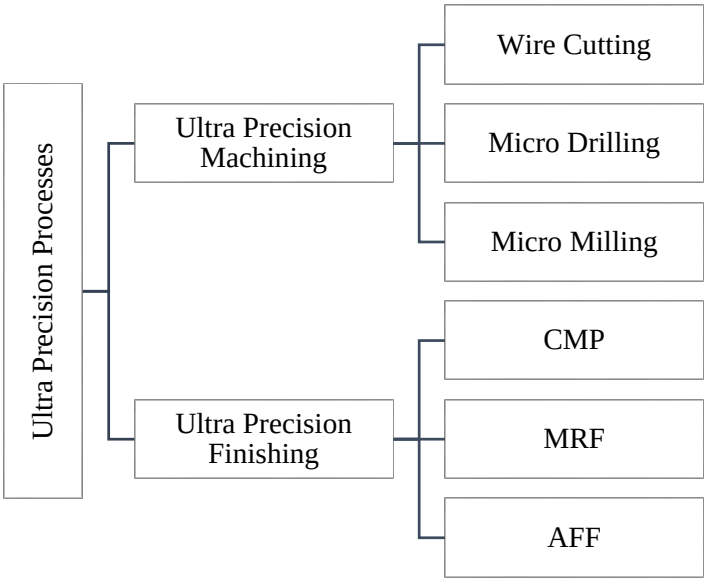

Figure I.1. Ultra precision processes examples.

I.2. Ultra precision machining techniques

Ultra-precision machining techniques are advanced manufacturing processes designed to produce components with extremely high tolerances and superior surface finishes. The techniques entail the systematic removal of material from a workpiece to attain exact dimensions and intricate shapes. This form of machining has evolved significantly over the years relative to other processes, as demonstrated in Figure I.2. Ultra-precision machining fundamentally relies on its capacity to manufacture components with exceptional accuracy and consistency, which is crucial for applications requiring high precision and reliability. The processes employ advanced equipment to guarantee that each component adheres to rigorous quality standards. Accuracy is a critical aspect of modern manufacturing, with achievable surface roughness of less than 10 nm [1].

Various ultra-precision processes are available, each designed for particular material characteristics, geometric intricacies, and application requirements. This chapter outlines essential machining techniques such as cutting, drilling, and milling, emphasizing their operational principles, advantages, and appropriateness for micro-scale applications.

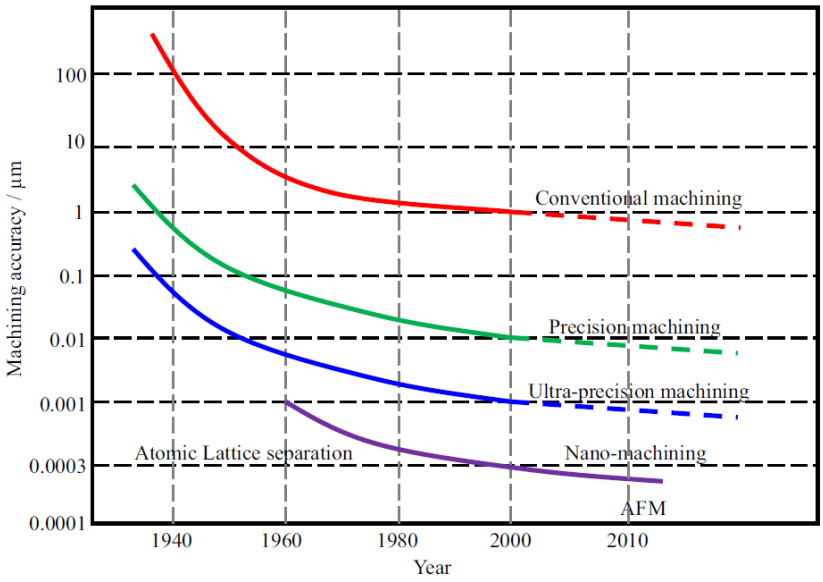

Figure I.2. Progress of machining accuracy for the different machining. [1]

I.2.1. Ultra-Precision Cutting:

Ultra-precision cutting is a manufacturing technique characterized by cutting materials with exceptional accuracy, typically at the micron or sub-micron scale.

Advanced cutting tools composed of materials such as diamonds are commonly employed in ultra-precision cutting, enabling the production of surfaces characterized by minimal roughness. This technique is essential for applications where minor deviations from the specified dimensions or surface finish can substantially impact the performance of the final product. This machining technique employs various ultra-precision cutting processes, each offering distinct advantages and applications. Wire sawing is a prevalent precision machining process that employs a thin wire or cable to cut through various materials. The filament, functioning as the cutting tool, is typically classified into two categories according to the abrasive grain method [2-5], as illustrated in Figure I.3.

- This method employs loose grains (free abrasive) along with an external abrasive slurry during the cutting process.
- Employing fixed grains, wherein the wire is coated with abrasive particles, usually diamond, as illustrated in Figure I.4.

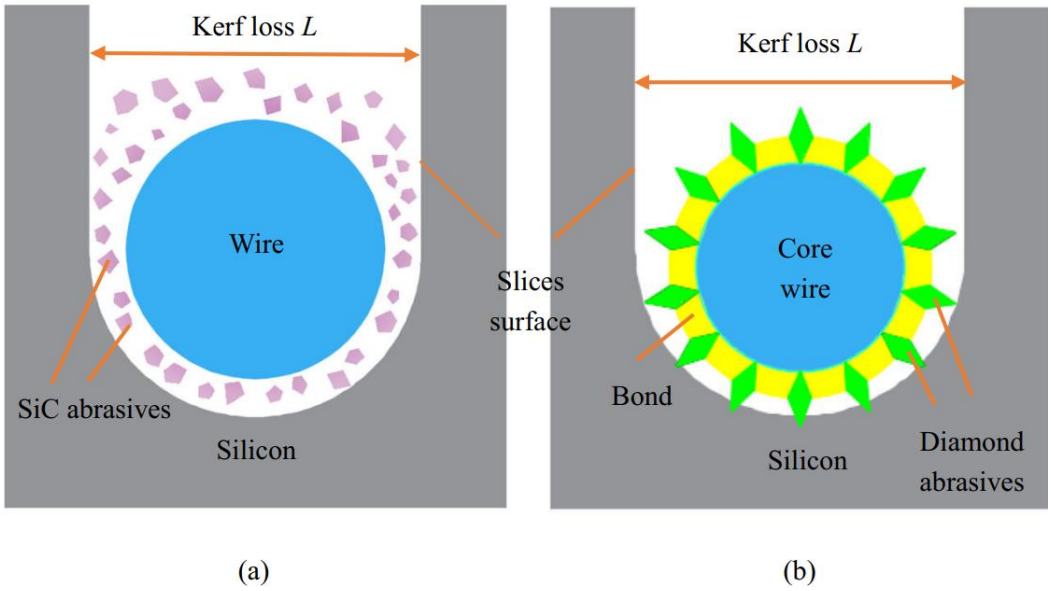

Figure I.3. Schematic diagram of wire sawing. (a) Loose abrasive wire sawing. (b) Fixed abrasive wire sawing. [6]

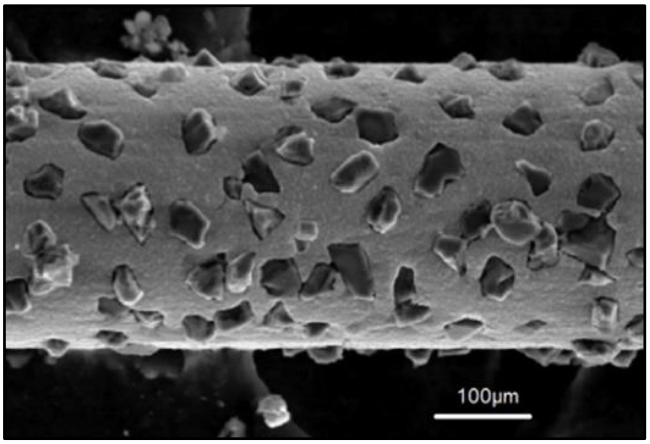

Figure I.4. Coated wire with abrasive grains. [5]

Wire sawing may utilize a single-wire configuration, where a continuous wire encircles the cutting area, or a multi-wire setup, in which several wires operate in parallel, facilitating the concurrent cutting of multiple slices [6, 7]. The sample's positioning may vary; it can remain stationary while the wire moves, or the wire can be fixed while the sample moves, contingent upon the application and equipment design, as illustrated in Figure I.5.

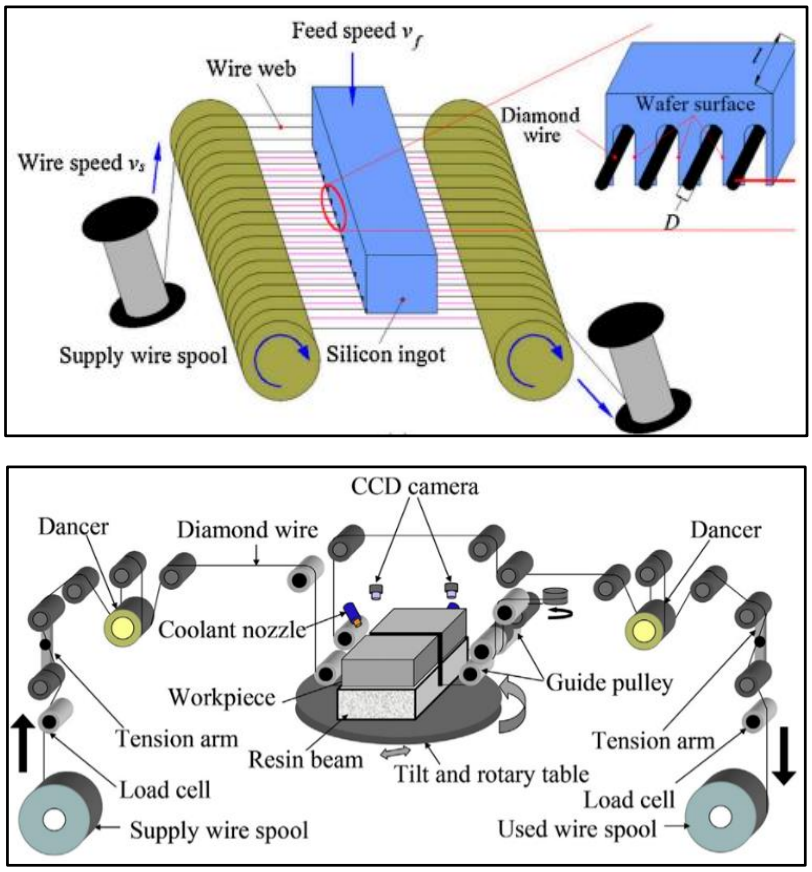

Figure I.5. Wire sawing configurations: (a) multi-wire arrangement, (b) single-wire setup. [7,8]

A hybrid approach in wire sawing integrates elements from multiple process methodologies, achieving an optimal balance between precision and efficiency. This mixed technique is primarily utilized in specialized cutting tasks, including:

- Ultrasonic Vibration-Assisted Wire Sawing (UV-DWS), which employs ultrasonic vibrations to improve cutting efficiency.

- Electrical Discharge-Assisted Wire Sawing (ED-DWS) employs electrical discharges to enhance the cutting process of conductive materials.

- Electrochemical-Assisted Wire Sawing (EC-DWS) utilizes electrochemical processes to facilitate cutting, particularly effective for materials that are difficult to cut with conventional techniques.

These innovative combinations facilitate enhanced control and efficiency in wire sawing operations, addressing specific requirements in complex and precision cutting. [7]

I.2.2. Ultra-Precision Drilling

Micro drilling is a precision machining technique that produces small holes, generally with diameters from a few micrometers to under a millimeter [9, 10]. As illustrated in Figure I.6, this process can achieve micro-holes of exceptionally small diameter, demonstrating the capabilities of ultra-precision drilling across various materials, including metals, polymers, and ceramics. This process requires a high degree of accuracy and precision. Micro-drilling has major challenges, such as keeping the size accurate, reducing tool wear, and handling material properties, because even small mistakes can seriously impact how well the drilled part works.

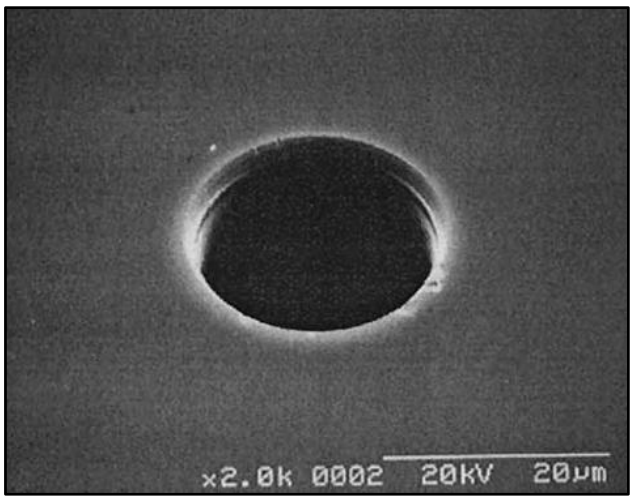

Figure I.6. A drilled micro-hole of 6.7 µm diameter. [10]

Advanced micro-drilling techniques can be divided into two categories:

Nonconventional techniques:

- The laser drilling process [11] removes materials using thermal energy. It is a contactless drilling process with no tool wear and not restricted to only conductive materials. This method uses a thermal heating source to melt and vaporize the workpiece. It is a great choice for creating holes with minimum hole chips and perfect roundness, as these two characteristics are always desired when drilling holes.
- Ultrasonic drilling (USD) [12]: This method utilizes the energy of ultrasound that is used to vibrate the cutting tool to drill relatively shallow holes in low ductile materials. It is a form of mechanical drilling that fabricates holes without any recast layer and alteration of the microstructure of workpiece materials.
- Abrasive water jet drilling (AWJD) [13]: This method includes abrasives mixed in water jet where materials are removed by high pressure through a slurry. Abrasive water jet drilling, on the other hand, is a process with the absence of heat, and abrasive particles are combined with water at high speed and pressure to erode material from the workpiece.

Conventional ultra-precision drilling is a high-accuracy subtractive manufacturing process that uses rotary cutting tools, typically twist drills or micro-drills under tightly controlled machining conditions to produce small-diameter holes (often in the micrometer to sub-millimeter range) with tight dimensional tolerances and surface quality. This method relies on advanced CNC (Computer Numerical Control) machines as precision drilling equipment to achieve consistent hole placement. [14, 15]

I.2.3. Ultra-Precision Milling

Ultra-precision milling is a manufacturing process that involves the accurate reproduction of specific shapes on a workpiece through material removal, as illustrated in Figure I.7. Various techniques exist for ultra-precision milling, including laser milling [16], electrochemical milling [17], and micro milling [18]. These techniques are advantageous for producing small, intricate components that necessitate high precision, frequently at the microscale [19].

The capacity to generate intricate features on different materials such as metals, polymers, and ceramics renders them crucial and adaptable equipment in contemporary manufacturing. Micro milling resembles conventional milling but operates on a significantly smaller scale and uses finer tools [20, 21]; an example of such a tool is illustrated in Figure I.8.

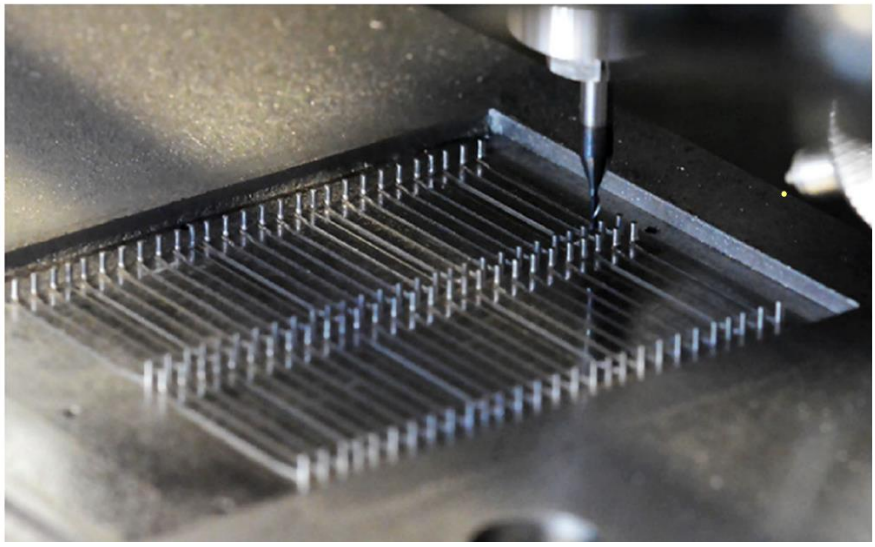

Figure I.7. Micro-milling of a lab-on-a-chip microfluidic mold: 4 arrays of 28 pins with 0.8 mm diameter and 2 mm height. [21]

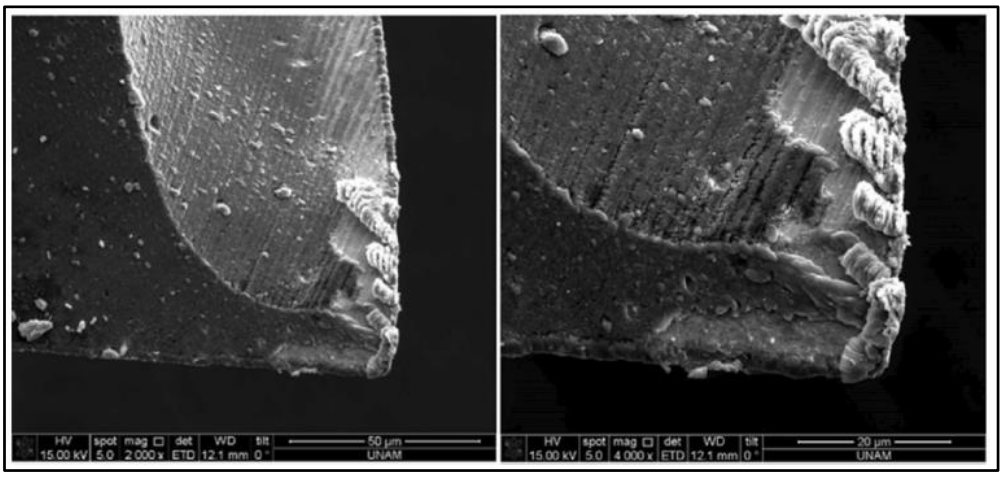

Figure I.8. One edge SEM image of micro milling tool. [21]

I.3. Ultra-Precision Machining Parameters

The parameters for ultra-precision machining depend on the specific requirements of the part being produced. Common factors include process-related and machine-specific variables that influence surface quality, dimensional accuracy, and material integrity. In ultra-precision settings, even minor fluctuations in cutting conditions, environmental stability, or tool geometry can profoundly affect the results. Thus, the careful selection and understanding of these parameters is crucial, particularly when machining brittle or high-performance materials.

This section outlines the essential parameters necessary for maintaining nanometric finishes and sub-micron accuracy in ultra-precision machining processes.

I.3.1. Tool Material and Geometry

The material and geometry of the tool in ultra-precision machining are critical factors that significantly affect the quality of the machining process and the final shape and surface quality of the machined part. The tool material must possess several essential properties; for example, hardness indicates that the material needs to be exceptionally difficult to endure the elevated pressures and temperatures experienced during machining. The second property of material tools is wear resistance, indicating enhanced durability against wear. This characteristic is crucial for maintaining precision over prolonged periods and minimizing the need for tool replacements. Thermal stability refers to the requirement for materials to possess a low coefficient of thermal expansion, ensuring dimensional stability across varying temperatures. [22-24]

A single-crystal diamond is widely used as a material tool in ultra-precision cutting processes due to its status as one of the hardest known materials [3], providing remarkable wear resistance and thermal conductivity. Various tool geometries are employed in ultra-precision machining [22]. Figure I.9 illustrates several examples, depending on the selected operation and the intended configuration of the machine. In general, the tool should possess a cutting edge with specific shape specifications such as:

- Sharpness [23]: Ultra-precision tools require sharp edges to attain fine finishes and precise dimensions.

- Edge radius [24]: A reduced edge radius facilitates finer cuts; however, it may exhibit increased susceptibility to wear and breakage.

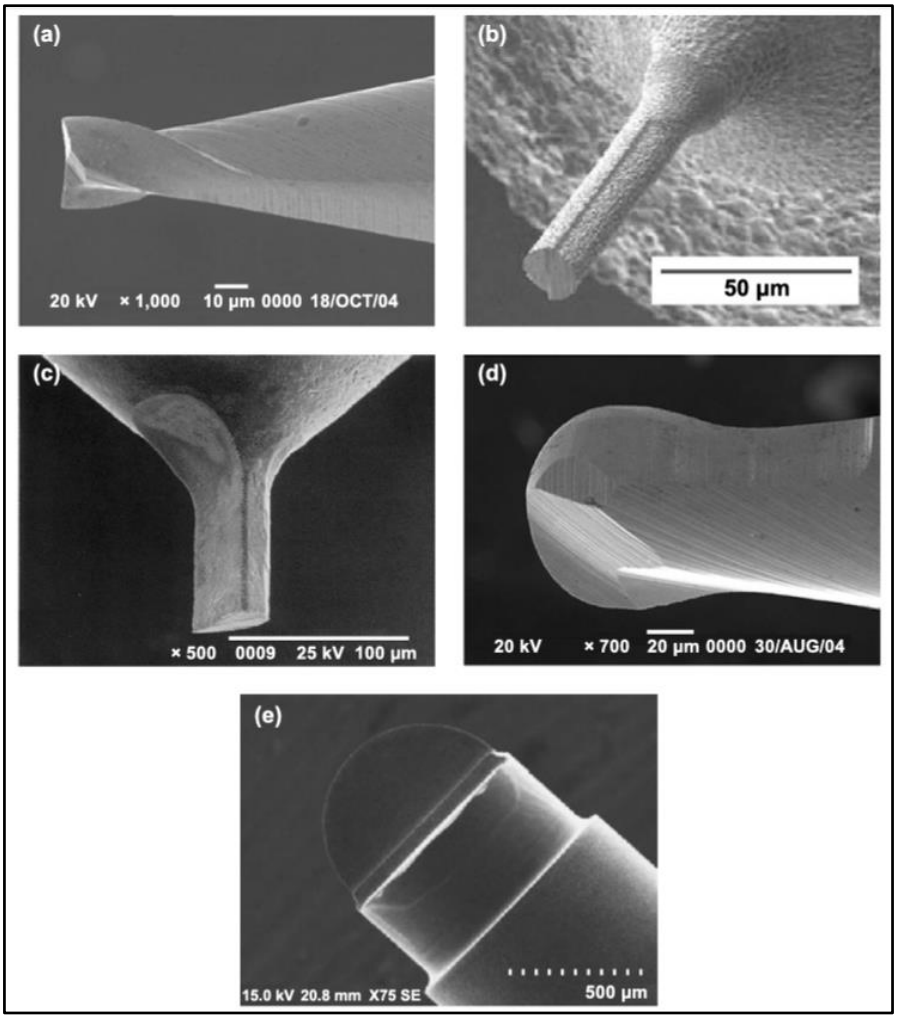

Figure I.9. Different cutting tool used in micro milling tool. [22]

Recent investigations into micro milling processes have highlighted the significant influence of cutting edge integrity on surface quality. Aramcharoen et al. (2009) investigated the impact of different tool edge geometries, including chipped, cracked, and multi-edge conditions, on surface finish in the micro milling of hardened steel. The results presented in Figure I.10 indicate that tools featuring rounded and well-defined edge radius yield smoother surfaces consistently, in contrast to tools with damaged geometries, which result in heightened roughness due to irregular material removal and vibration. This finding show the importance of selecting hard and wear-resistant tool materials while also maintaining the integrity of their edge geometry during machining, particularly in ultra-precision applications. Cutting-edge geometry significantly influences burr formation in micro milling, alongside its impact on surface roughness.

Figure I.11 illustrates that tools exhibiting damaged edges, including chipped or multi-edge configurations, produce considerably larger burrs than those with rounded or chamfered edges.

This phenomenon primarily results from uneven plastic deformation and uncontrolled material flow, which are attributed to irregular cutting profiles. Maintaining a stable and well-defined edge geometry enhances the surface finish and minimizes the burr size, thereby improving dimensional precision and machining quality.

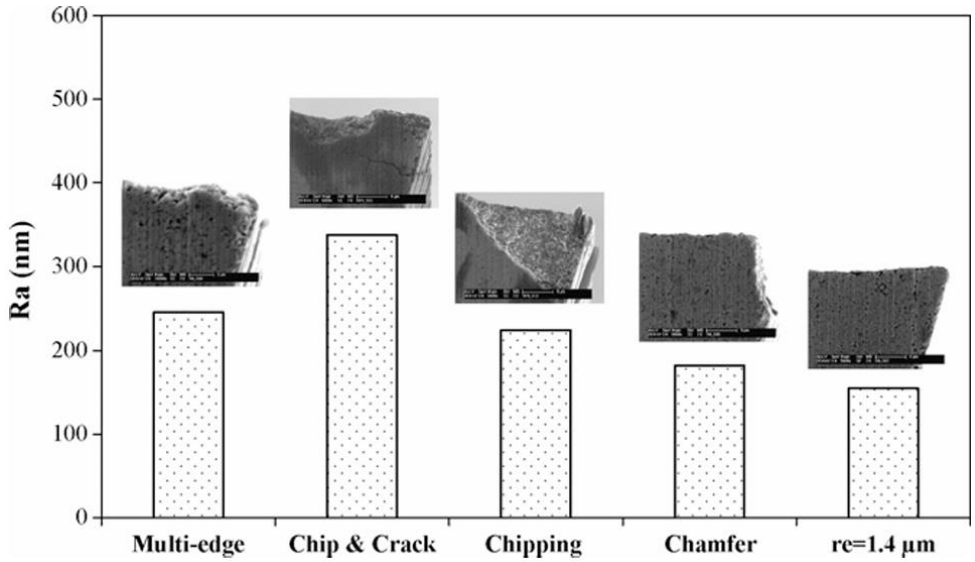

Figure I.10. Influence of cutting edge geometry on surface finish in micro milling. [25]

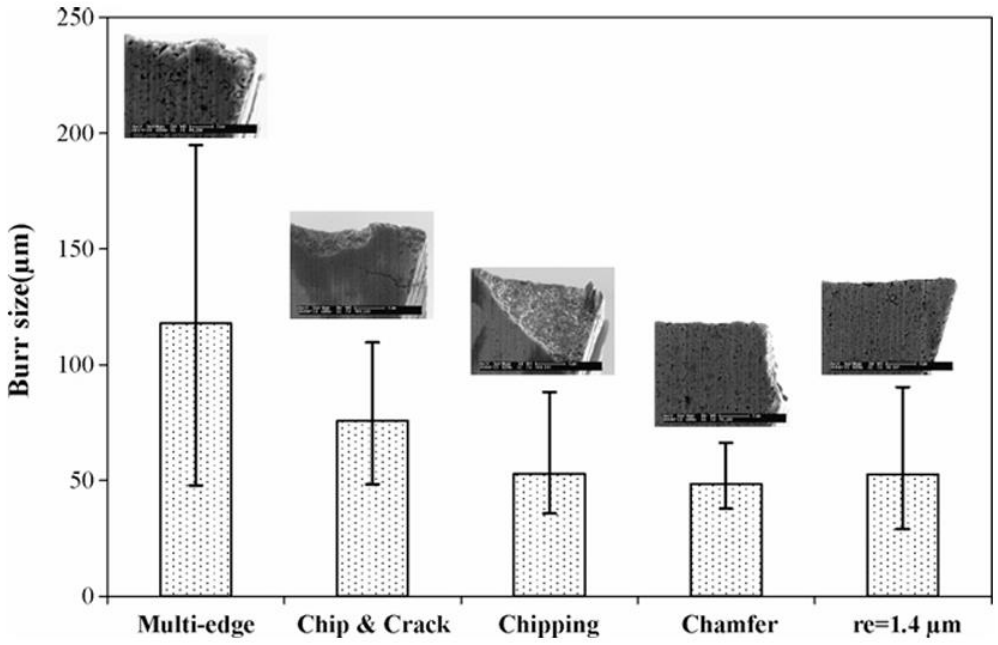

Figure I.11. Effect of cutting edge geometry on burr formation in micro milling. [25]

I.3.2. Cutting Speed and Feed Rate

Cutting speed and feed rate are more precise and controlled parameters compared to conventional machining processes, enabling the production of high surface quality with minimal material deformation. The cutting speed in ultra-precision machining refers to the velocity at which the tool's cutting edge traverses in relation to the workpiece. This parameter significantly affects heat generation, tool wear, and the quality of the machined surface. Maintaining an optimal cutting speed is essential for achieving the desired surface finish and dimensional accuracy. Precise control of speed is essential to reduce thermal effects and mechanical stresses that may compromise surface quality [26, 27].

In ultra-precision machining, the feed rate refers to the speed at which the workpiece advances towards the cutting tool or the tool moves across the workpiece (can be in the two ways). It is generally quantified in micrometers per revolution or pass. It is essential to regulate the feed rate meticulously to attain the intended surface quality. An excessively high feed rate may result in heightened tool wear and possible damage to the workpiece, while an overly low feed rate can cause inefficiency and prolonged machining time [26, 27].

The equilibrium between cutting speed and feed rate is crucial in ultra-precision machining. Both parameters require optimizations to achieve the desired surface finish and dimensional accuracy. The values for cutting speed and feed rate are contingent upon the material being machined, the tool material, the complexity of the part, and the specific requirements for surface roughness and dimensional tolerance. Advanced control systems and feedback mechanisms are used in ultra-precision machining to adjust parameters in real time, ensuring optimal performance.

Experimental studies in micro-milling contexts have validated the influence of cutting speed and feed rate on surface quality and burr formation. Zariatin et al. (2018) performed a detailed analysis of aluminum alloy 1100, demonstrating that surface roughness significantly increases with machining time and feed rate, especially at low spindle speeds. Figure I.12 demonstrates that increased feed rates (e.g., 1 mm/s) result in a significant increase in surface roughness, whereas reduced feed rates (0.05 mm/s) contribute to the preservation of finer finishes over time.

This study underscores the necessity for balanced parameters to regulate tool–workpiece interaction and heat accumulation. Additionally, the SEM analysis (Figure I.13) indicates that burr formation is significantly influenced by feed and speed conditions. Reduced feed rates and increased spindle speeds significantly decrease burr size, resulting in cleaner cuts. The results highlight the significance of optimizing spindle speed and feed rate to enhance surface quality.

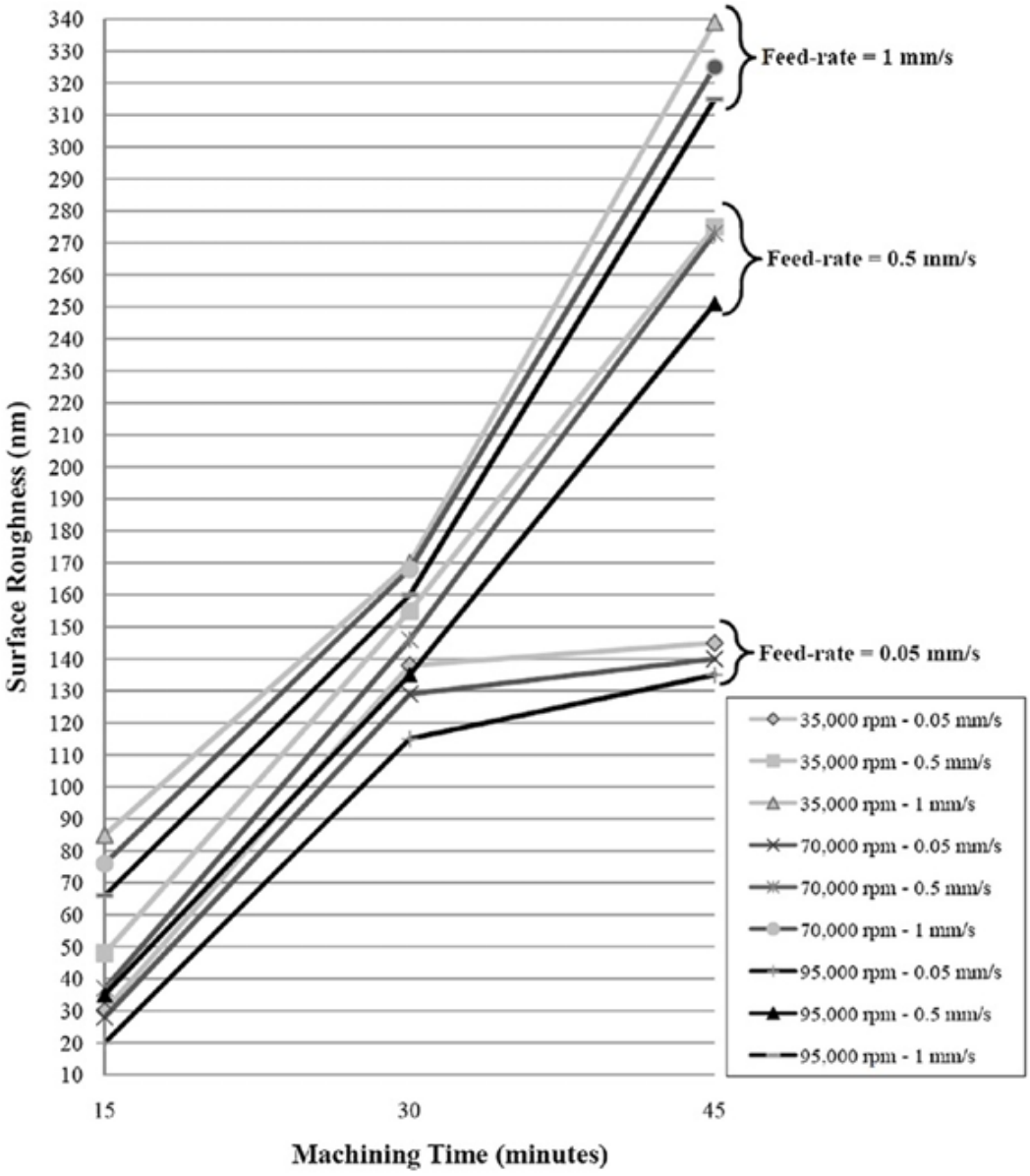

Figure I.12. Variation of surface roughness with machining time under different combinations of spindle speed and feed rate during micro-milling. [28]

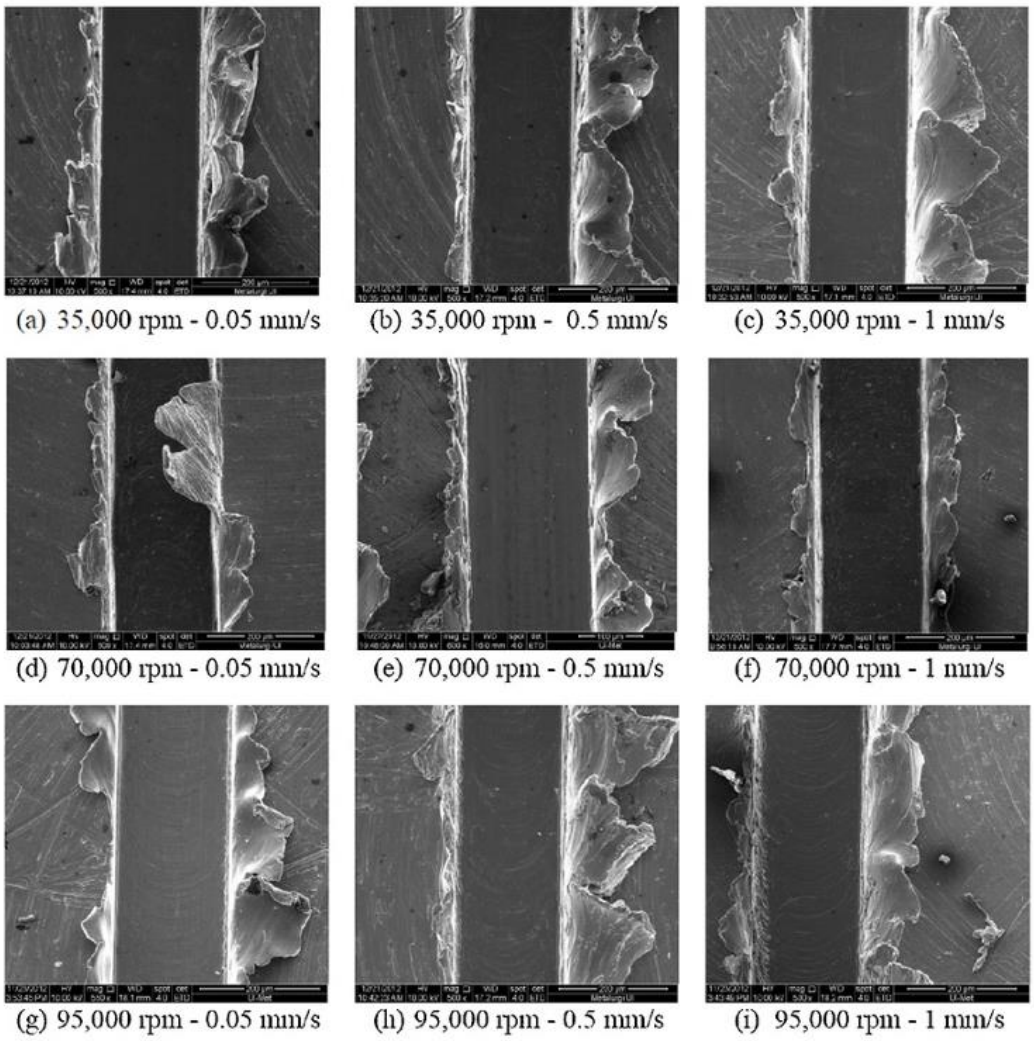

Figure I.13. SEM images of burr formation in micro-milling of Al 1100 for different spindle speeds and feed rates. [28]

I.3.3. Depth of Cut and Tool Path

During ultra-precision machining, the depth of cut and tool path concepts are also important for achieving the desired surface quality. The depth of cut refers to the thickness of the material being removed in one step down of the cutting tool (tool engagement into the material during machining); this measurement is often at the micron or sub-micron level. The depth of the cut is a critical parameter because it directly impacts the stress imposed on both the tool and the workpiece. A deeper cut can increase the material removal rate and cause more stress and potential tool deflection, compromising accuracy and surface quality. In ultra-precision machining, maintaining a very shallow depth of cut is essential to minimizing mechanical and thermal distortions [26].

However, this means more steps down are needed to remove material, which can increase machining time. The depth of the cut must be balanced efficiency with the quality requirements of the material being machined.

The tool path refers to the trajectory the cutting tool follows over the workpiece. UPM often involves a complex path that requires high precision control. The tool path determines the interaction between the tool and the workpiece and thus directly influences the surface finish and overall quality of the machined part. Precision in the tool path is crucial for achieving the high precise tolerances and surface finishes required in ultra-precision applications. Designing and controlling the tool path in ultra-precision machining involves accounting for factors like tool geometry, cutting forces, and material properties. The tool path must be optimized to avoid tool wear, reduce the risk of tool chatter, and ensure even material removal, especially for complex geometries [29, 30].

Advanced computer-aided manufacturing (CAM) software and high-precision CNC (Computer Numerical Control) machines are often used to control the depth of cut and the tool path accurately. These technologies allow for the precise execution of complex tool paths with minimal depth of cut to achieve the required surface finish and dimensional tolerances [31].

The specific strategies for depth of cut and tool path selection depend on the material, part geometry, desired surface finish, and machining equipment capabilities. An example of tool path generation is shown in Figure I.14.

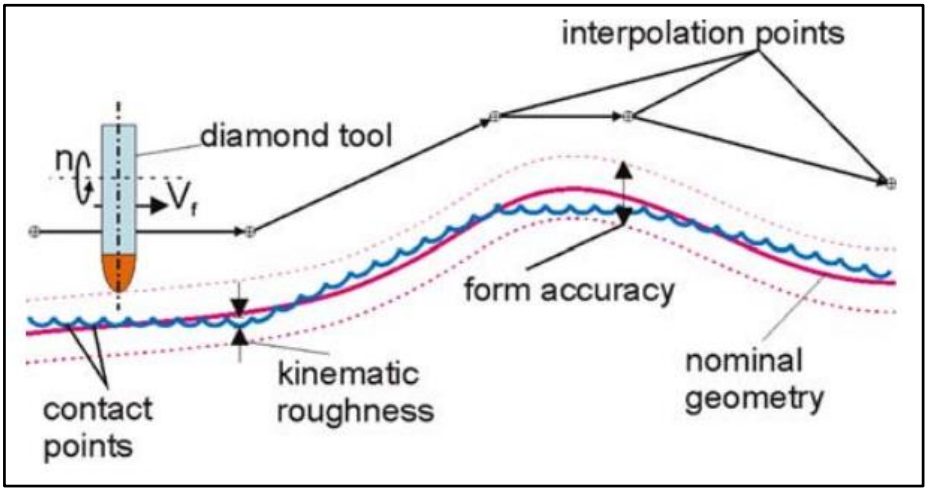

Figure I.14. Schematic of tool path generation during ultra-precision milling. [32]

The depth of cut is among the most influential parameters in determining both the mode of material removal and the resulting surface quality during micro-milling as example. In an experimental study by Huo et al. (2015), it was observed that increasing the axial depth of cut from 10 μm to 30 μm led to a marked deterioration in surface roughness. This change is primarily due to a shift from ductile mode cutting, characterized by smooth material shearing, to brittle fracture, where deeper penetration exceeds the critical stress threshold and initiates surface micro-cracks and chipping. As illustrated in Figure I.15, maintaining a shallow depth of cut is essential to preserving nanometric surface finishes and suppressing surface defects such as pits, chipping, and subsurface fractures, especially when machining brittle materials like monocrystalline silicon.

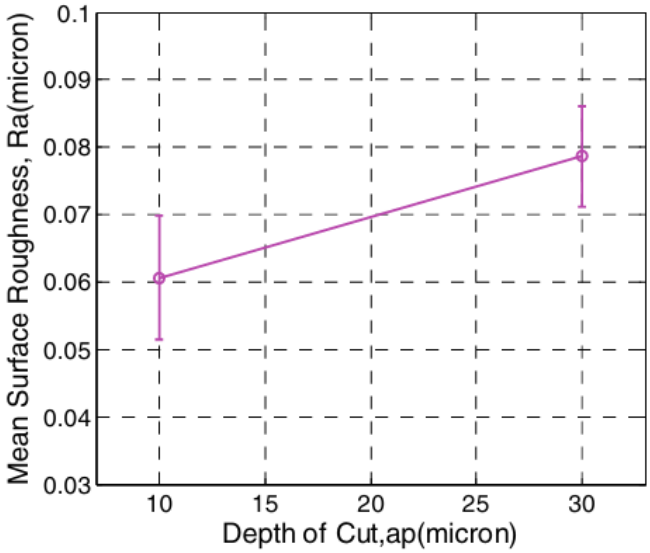

Figure I.15. Effect of axial depth of cut on surface roughness in micro-milling of monocrystalline silicon using diamond-coated tools. [33]

I.4. Ultra precise finishing techniques

Ultra-precise finishing represents one of the most critical aspects of advanced manufacturing, enabling the production of components with high surface quality and dimensional accuracy. These finishing techniques have become essential in industries, where surface imperfections measured in nanometers can significantly impact product performance. Polishing is one of the most widely used techniques that is crucial in achieving a high-quality surface finish, particularly in applications.

Several polishing techniques are suitable for different materials and desired outcomes. Here's an overview of some common polishing techniques.

I.4.1. Chemical Mechanical Polishing (CMP)

Chemical Mechanical Polishing (CMP) is a pivotal process in modern manufacturing. CMP is a hybrid technique combining elements' simultaneous chemical and mechanical actions to achieve high surface roughness and surface planarity levels. The principle of CMP is to use a combination of abrasive and chemical actions to remove material from the surface of a workpiece, which involves a polishing pad and a slurry. A polishing pad drives the mechanical aspect by exerting a physical force between the abrasive grains and the workpiece. Combined with the pad's motion, this force facilitates the gradual removal of material from the workpiece's surface. On the chemical side, we use a specially formulated slurry containing both abrasive particles and chemical reactants. These reactants chemically alter the surface of the workpiece, making it more susceptible to abrasion and aiding in the material removal and surface finishing process. [34]

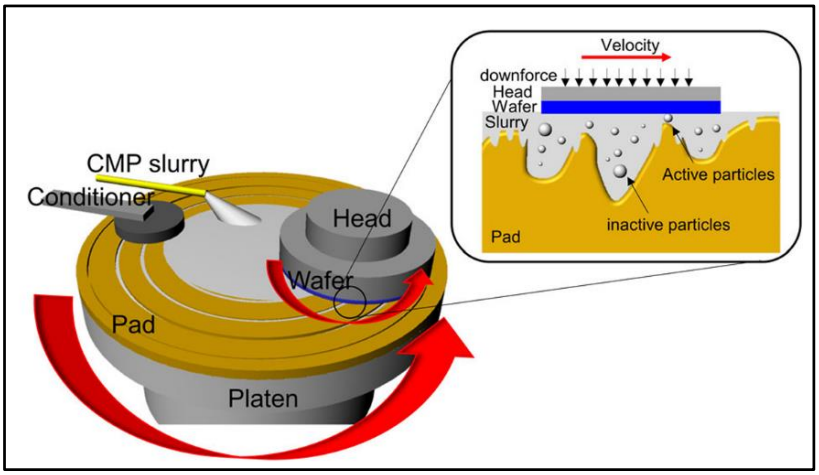

Figure I.16. Schematic diagram of a CMP tool interactions in the contact region. [38]

The effectiveness of CMP depends on the intricate interplay between these components, with the pad's texture, the slurry's composition, and the applied pressure and speed all contributing to the outcome [35, 36]; see Figure I.16. Diverse materials, including silicon, oxides, and metals, are processed using CMP. The significance of CMP in ultra-precision machining cannot be overstated; it is instrumental in achieving the nanometre-level flatness and roughness required in ultra-precision machining, where even the slightest surface irregularity can lead to significant performance issues in devices. In some CMP process techniques, a conditioner is integrated to perform a crucial function, maintaining the pad optimally throughout the polishing phase. The conditioner's presence is instrumental in preserving the pad's texture and properties, facilitating smooth and efficient polishing [37, 38].

I.4.2. Magneto-Rheological Finishing (MRF)

Magnetorheological Finishing (MRF) is an advanced polishing technique used mainly in optics. This process stands out due to its unique use of a magnetically sensitive fluid to achieve ultra-smooth surfaces [39]; see Figure I.17. Magnetorheological finishing is a subaperture polishing process that utilizes a magnetorheological (MR) fluid. This fluid comprises soft-magnetic iron particles, abrasive particles, and a carrier fluid. The defining characteristic of MRF is the ability to rapidly and precisely change the fluid's physical properties, such as viscosity and abrasiveness, by applying a magnetic field. RF can achieve surface finishes with extremely high precision, making it ideal for applications where surface accuracy is critical [40, 41].

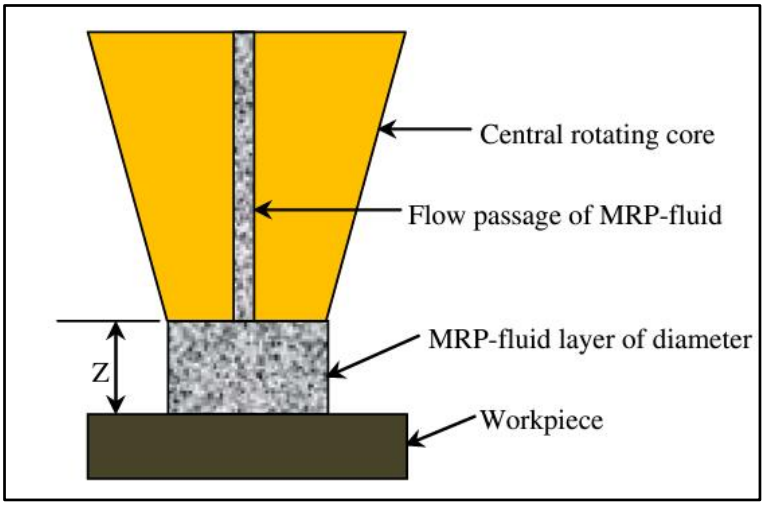

Figure I.17. Schematic diagram of Magneto-Rheological Polishing fluid interaction on the workpiece. [41]

I.4.3. Abrasive Flow Finishing (AFF)

Abrasive Flow Finishing (AFF) is an ultra-precise finishing process using abrasive grains to polish and finish complex internal shapes and surfaces. This technique is beneficial for finishing areas like internal channels and holes in parts [42, 43]; see Figure I.18.

The process works by flowing viscoelastic polymer and abrasive particle carriers through the part's surface to be finished. The flow is controlled by a hydraulic system, which can be adjusted to vary the pressure and flow rate, enabling precise control over the finishing process [44].

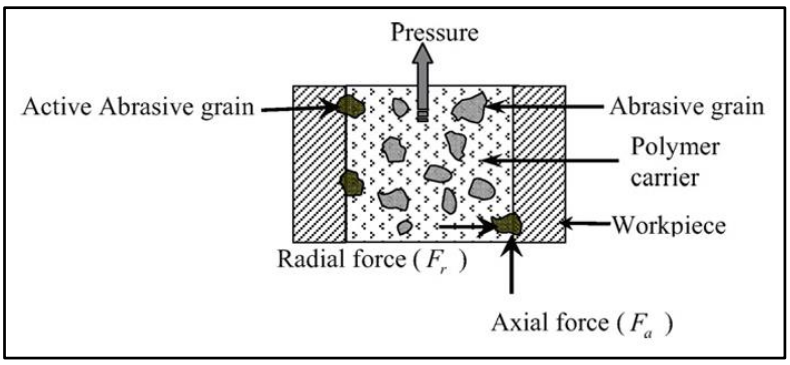

Figure I.18. Schematic diagram of Abrasive Flow Finishing abrasive action on the workpiece. [44]

I.5. Ultra precise finishing parameters

Finishing processes contribute not only to the surface appearance but also to the functional performance of the material. In this thesis, the investigation is limited to the mechanical aspect of finishing, with specific attention to the role of abrasive grains as the active tool in material removal. The polishing process is influenced by several parameters, including abrasive grain size, applied pressure, relative velocity, and polishing time. These factors are considered in the experimental methodology to evaluate their effect on surface quality.

I.5.1. Abrasive Type and Size

In ultra-precision finishing, the choice of abrasive grain type and size is of paramount importance, as it significantly influences the final quality, efficiency, and effectiveness of the finishing process. The precision range of these methods is critical, particularly since the amount of material removed during the finishing is very minimal, often less than a few microns [45]. This small scale of material removal is a feature of ultra-precision finishing techniques (Polishing), and it requires selection of abrasive grains; see Figure I.19.

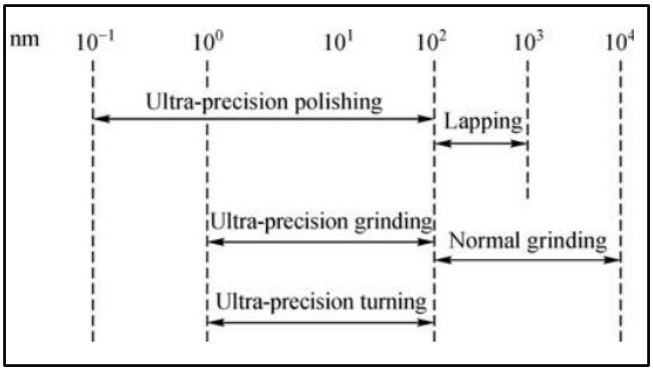

Figure I.19. The machining accuracy of ultra-precision methods. [45]

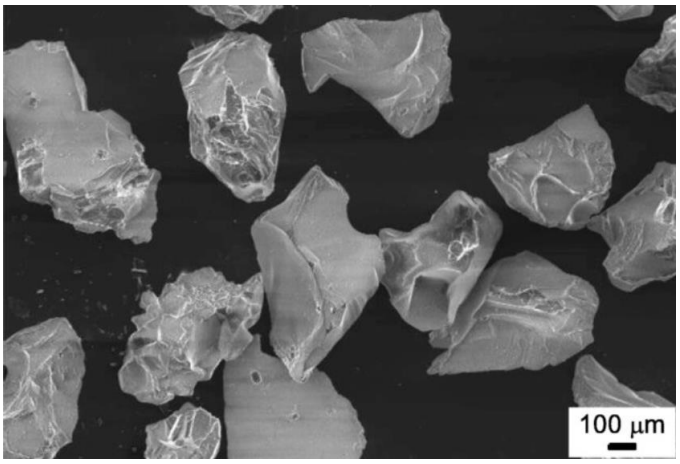

Figure I.20. SEM image of the abrasive grains (mean particle size: 425 µm). [46]

The selection of the appropriate abrasive grain type is crucial for achieving the desired surface finish and accuracy, with different grains producing varying levels of smoothness and precision; an example of grains is shown in Figure I.20. This choice is also pivotal in preventing surface defects, such as scratches or non-uniform textures, which are particularly detrimental in applications demanding high precision. [46]

Moreover, compatibility with the material of the workpiece is essential; different materials react differently to various abrasives, and the wrong choice can lead to excessive material removal or, worse, contamination that alters the material's properties. The efficiency of the polishing process is another critical consideration; the material removal rate is directly impacted by the type of abrasive used, affecting both processing time and throughput.

Furthermore, the choice of abrasive affects tool wear and longevity; durable abrasives like cubic boron nitride or synthetic diamond can reduce the frequency of the replacement and downtime. In ultra-precision fields, the right abrasive ensures that stringent requirements are met.

Thus, the selection of abrasive grains for ultra-precision finishing is a multifaceted decision that must be approached with a comprehensive understanding of their impact on the final product, process efficiency, and tool life [47, 48].

A wide variety of ultra-precision polishing methods have been developed to address the stringent requirements of surface quality across different materials and applications. As summarized in Table I.1, these methods can be broadly categorized based on the nature of the abrasive medium and the mechanism by which material removal is achieved.

Other techniques such as chemical mechanical polishing or mechanical chemical polishing use chemical solutions in conjunction with soft abrasive particles to promote surface smoothing through combined chemical and mechanical interactions as previously discussed. Techniques like magnetic fluid polishing, electrophoresis polishing, and magnetic abrasive finishing exploit electric or magnetic fields to control abrasive particle behavior, offering precise regulation of the polishing force and direction. Suspension polishing and elastic emission machining use fine abrasive suspensions to achieve uniform material removal, which is particularly suitable for brittle or soft materials. Each method presents distinct advantages depending on the target surface roughness, material sensitivity, and geometric complexity, making the choice of polishing technique a critical decision in ultra-precision manufacturing.

Table I.1. Classification of Ultra-Precision Polishing Techniques Based on Abrasive Mechanism. [46]

Polishing Method	Abrasive
Chemical mechanical polishing	Chemical solution and abrasive particle
Mechanical chemical polishing	Soft abrasive (solid phase reaction with the workpiece)
Hydration polishing	Super-heated steam
Non-pollution polishing	Pure water or ice
Hydroplane polishing	Chemical solution
Suspension polishing	Soft abrasive
Elastic emission machine	Soft abrasive
Magnetic fluid polishing	Magnetic fluid
Electrophoresis polishing	Electric control of abrasive
Magnetic levitation polishing	Magnetic fluid
Magnetic abrasive finishing	Magnetic abrasive

Table I.2 presents a comparative overview of abrasive materials commonly used in ultra-precision polishing processes, along with their physical characteristics, particle size distributions, and Mohs hardness values. The abrasives include both hard crystalline materials, such as monocrystalline and polycrystalline diamond, as well as a range of metal oxides, including alumina (α-Al_2O_3, γ-Al_2O_3), silica, zirconia (ZrO_2), and ceria (CeO_2). Each abrasive's effectiveness depends on factors such as its mean particle size, shape, and intrinsic hardness. For instance, diamond exhibits the highest Mohs hardness (10) and is available in particle sizes below 0.25 µm, making it suitable for applications demanding extremely smooth surfaces with minimal sub-surface damage. On the other hand, softer abrasives like ceria and silica are often selected for their gentle interaction with sensitive substrates. The table also distinguishes between SEM/TEM-measured particle sizes and Microtrac (laser diffraction) data, offering insight into particle distribution characterization.

These values, combined with vendor-specific data, provide critical information for selecting appropriate abrasives in the precision polishing of optical materials, semiconductors, and brittle crystals, like BGO.

Table I.2. Comparison of the particle size by vendor's data and characterization [48]

Abrasive	SEM/TEM (μm)	Microtrac MNd50, (μm)	Vendor/Product Code	Mean Particle Size (μm) by Vendor	Mohs Hardness
Monodiamond	~0.15	0.180/0.44	Warren/SYN S3R-8	(0–0.25)	10
Polydiamond	~0.15	0.234/0.7	Warren/Poly WDP 728Q-9	~0–0.25	~10
Polydiamond	-	N/A	Engis/Hyperz D1594	~0.5 (slurry)	~10
α-Al_2O_3	0.2	0.150/0.9	Ferro/1802	~0.16	9
α-Al_2O_3	0.2	N/A	Reynolds/RC-UFX-DBM BM-1819	~0.2	9
γ-Al_2O_3	~3	2.263/3.57	Reynolds/CB-116-98 AR*	~0.5	8
Diaspore	~0.6/2.9	0.629/3.8	Ward's/46 E 2605	~0.4 (slurry)	6.5–7
Silica	-	N/A	STI-4038	~0.2 (slurry)	7
ZrO_2	0.1	0.93/3.2	Tosoh/TZ-3Y	~0.2	7.5
CeO_2	0.2	1.86/3.11	Ferro/TRS 2270	~0.63	6

I.5.2. Polishing Pressure and Speed

The calibration of pressure and rotational speed is a critical factor in ultra-precision finishing, significantly affecting surface quality and operational efficiency. The parameters are essential for determining the accuracy of material removal from the surface, which directly affects the resulting surface topography. Effective regulation of pressure and speed is essential to reduce the incidence of surface defects, including micro-scratches, textural inconsistencies, and uneven material removal distribution, which are important.

The effective management of these variables is crucial for maximizing the material removal rate and minimizing processing time, thus improving the overall throughput of the finishing operation. Uniform application of pressure, coupled with a consistent speed profile, is instrumental in achieving homogeneity in the polished surface, a requisite for components necessitating high-dimensional accuracy and surface consistency. [49]

Furthermore, the longevity and performance of the finishing tools and equipment are significantly contingent upon these settings. Excessive application of pressure or overly high rotational speeds can precipitate accelerated tool wear, augmenting operational expenses and potentially inducing thermal or mechanical stress within the workpiece, leading to its compromise. Conversely, optimal settings can extend abrasive and pad life, thereby fostering cost-effectiveness and material conservation.

In summary, the strategic control of finishing pressure and speed in ultra-precision polishing is paramount for achieving desired surface characteristics, ensuring process efficiency, maintaining tool durability, safeguarding operational safety, and accommodating the unique requirements of diverse materials. [50, 51]

As illustrated in Figure I.21, the Material Removal Rate (MRR) of sapphire was evaluated under varying polishing conditions using range analysis across four levels of polishing pressure, carrier rotation speed, and polishing time.

The results show that polishing pressure and carrier speed are the most influential parameters, each demonstrating a significant increase in MRR from Level 1 to Level 4. The evidence indicates that higher pressure and speed levels enhance material removal efficiency. In contrast, polishing time exhibited a comparatively moderate effect on MRR. This example reinforces the importance of carefully calibrating both pressure and rotational speed to improve polishing outcomes for hard, brittle materials like sapphire.

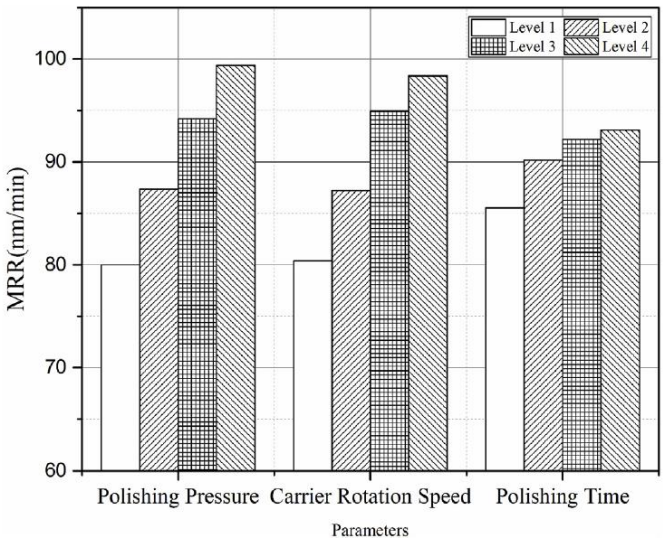

Figure I.21. The MRR of sapphire by range analysis. [51]

I.6. Material Considerations in Ultra Precision Processes

The choice of machining process is predominantly determined by the material's properties to be machined, depending on its application area later on, as these properties dictate how the material will respond to various machining techniques; see Figure I.22. Here is an example of material properties to consider when choosing machining processes:

Materials with distinct thermal characteristics require specific machining strategies to manage heat generation and dissipation effectively, ensuring dimensional accuracy and

preventing structural damage. Materials with low thermal conductivity retain heat in the cutting zone, which can lead to tool wear and thermal damage to the workpiece. Machining processes with efficient cooling systems or lower heat generation might be more suitable for such materials. [52]

The chemical properties of the material dictate its compatibility with various machining environments and substances, influencing decisions regarding coolants and lubricants to prevent corrosion or chemical degradation. Inert specific types of coolant may be necessary to prevent reactions like oxidation or corrosion, material characterizes and interaction with chemicals must be taking into consideration. [53]

Additionally, the material's mechanical properties, such as hardness, toughness, and ductility, directly influence the selection of machining processes, where these properties directly affect how the material behaves under mechanical stresses during machining. Materials with high hardness may need slower speeds or specialized cutting tools, while those with high ductility might require specific techniques to maintain precision. [54]

Thus, a comprehensive understanding of the material's properties guides selecting the most appropriate machining process to achieve high results regarding precision, surface finish, and overall part quality.

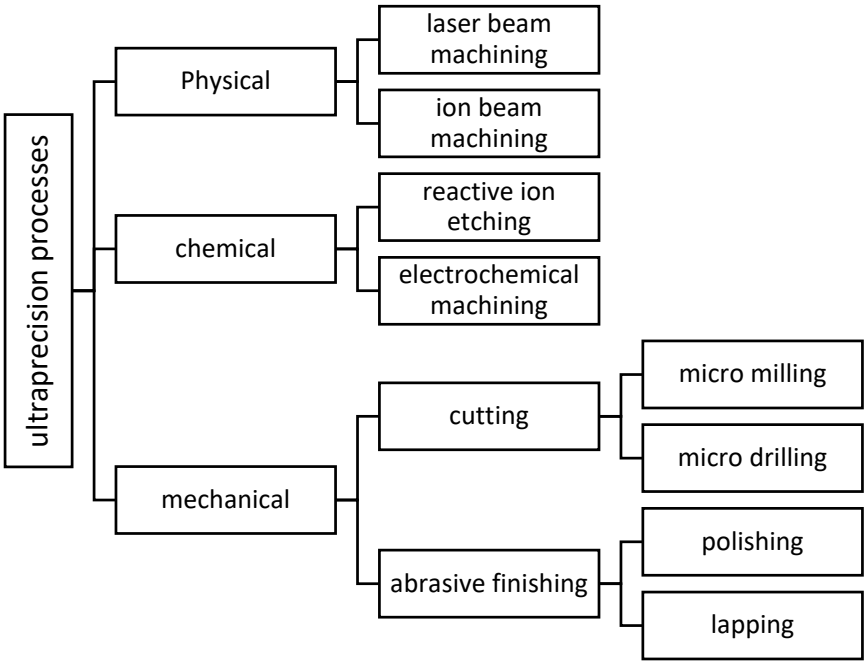

Figure I.22. Ultra precision processes classifications.

As shown in Figure I.22, ultra-precision processes methods are broadly categorized into three main groups: physical, mechanical, and chemical techniques [55]. Each category encompasses specific processes suited to different material characteristics and performance requirements.

Physical methods, such as laser and ion beam machining, are typically used for materials sensitive to thermal or beam-based energy interactions. Mechanical methods, which include both cutting (e.g., micro milling and drilling) and abrasive finishing techniques (e.g., lapping and polishing), are widely applied to hard and brittle materials requiring sub-micron surface finishes.

Chemical approaches, such as reactive ion etching and electrochemical machining, offer more control over material removal at the atomic level and are often used for delicate or micro-structured components.

This classification demonstrates the value of matching the machining approach to the material's physical behavior, especially in applications requiring extreme dimensional accuracy and surface quality.

I.7. Conclusion

This chapter has provided an overview of ultra-precision machining and finishing technologies, which are fundamental to modern high-accuracy manufacturing. It began by introducing the core principles and classification of ultra-precision processes, followed by a detailed look at machining techniques such as cutting, drilling, and milling. Particular focus was placed on the process parameters that influence machining outcomes, including tool geometry, feed rate, and depth of cut.

The chapter also examined advanced surface finishing methods such as chemical mechanical polishing (CMP), magnetorheological finishing (MRF), and abrasive flow finishing (AFF), each designed to meet the demanding surface quality requirements of nanometric applications. Key parameters such as abrasive grain size, applied pressure, and polishing speed were highlighted for their role in determining both efficiency and the final surface quality.

Finally, the influence of material properties on process behavior was discussed to demonstrate the value of thermal, mechanical, and chemical characteristics in guiding process selection and performance expectations.

Together, these theoretical foundations are essential for understanding the complex interactions between materials and processes in ultra-precision manufacturing. They establish the framework for the experimental approach, process optimization strategies, and application-specific studies that will follow in the next chapters.

CHAPTER II

SURFACE QUALITY AND MACHINING CHALLENGES IN BRITTLE MATERIALS FOR HIGH-PRECISION APPLICATIONS

II.1. Introduction

This chapter focuses on the surface quality and machining challenges specific to brittle materials, which are widely used in high-precision applications such as optics, photonics, and radiation detection. While the previous chapter introduced the fundamentals of ultra-precision machining and surface generation, this chapter extends the discussion to the behavior of brittle materials during machining and how surface quality affects their performance in real-world applications.

The chapter emphasizes the physical characteristics of brittle materials that make them challenging to machine, such as low ductility, high hardness, and a tendency to fracture. It also addresses the various mechanisms of material removal and explains how these influence the formation of microcracks, subsurface damage, and other defects that compromise surface quality. Then introduces the advanced measurement techniques used to assess surface roughness in such materials. Methods such as atomic force microscopy (AFM) are presented as essential tools for quantifying surface quality at micro- and nanoscales, supporting process evaluation and refinement.

Following this theoretical foundation, the focus shifts to a practical application where surface quality plays a critical role in Time-of-Flight Positron Emission Tomography (TOF-PET). The principles of PET imaging are reviewed, with particular emphasis on how surface conditions of scintillation crystals affect photon collection, timing accuracy, and spatial resolution.

Finally, the chapter outlines the technical and material-related challenges involved in fabricating these high-performance systems. From machining hard crystals with high precision to integrating different materials in heterostructure designs, these challenges demonstrate the importance of mastering both surface finishing and machining strategy.

II.2. Surface Topography: Evaluation and Measurement Techniques

II.2.1. Surface Characterization and Descriptions

The primary goal of UPP is achieving the desired shape with a low surface roughness. Surface roughness refers to the irregularities and defects on the surface of a material, as shown in Figure II.1, inherent to the manufacturing process. In ultra-precision processes, these irregularities are minimized to create a smooth surface. [56]

The surface quality is a critical factor in various industrial and manufacturing processes, as it significantly impacts the functionality and performance of machined parts. Surface roughness ensures proper fit and function for assemblies requiring precision fits. Additionally, it affects aesthetic qualities in consumer products, enhances corrosion resistance, and can impact heat and electrical conductivity [57]. Thus, measuring surface roughness is essential for optimizing the performance and quality of manufactured products.

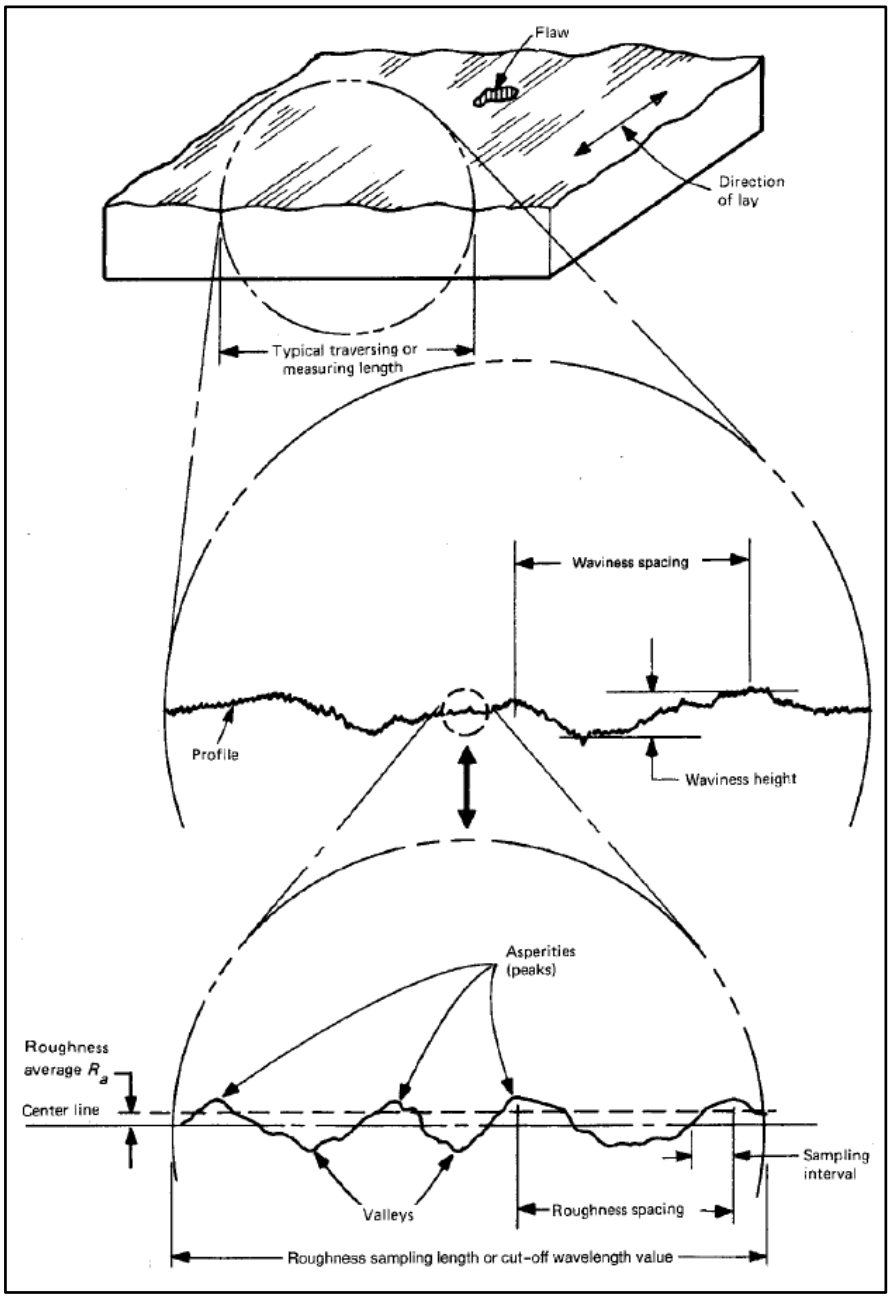

Figure II.1. Schematic of a surface profile. [57]

To fully characterize the quality of machined surfaces, especially in brittle materials, it is essential not only to measure roughness but also to understand the various roughness parameters that describe different aspects of surface quality. Gadelmawla et al. (2002) provided a comprehensive classification of these parameters, grouping them into amplitude, spacing, hybrid, and material ratio families. Their work underscores that relying on a single metric such as Ra (arithmetic average roughness) is often insufficient for assessing surface integrity, especially when subsurface damage, load-bearing capacity, or wear behavior are involved. Table II.1 presents a synthesis of these roughness parameters with their functional definitions, highlighting how each one contributes to a detailed understanding of surface behavior under mechanical and optical loading. [58]

Table II.1. Roughness profile showing key amplitude, spacing, and material ratio parameters.

Category	Parameter (Symbol)	Short Definition
Amplitude	Ra	Arithmetic average of surface deviations.
	Rq	RMS of surface deviations; sensitive to large peaks.
	Rp	Max height above mean line.
	Rv	Max depth below mean line.
	Rz	Mean of 5 highest peaks + 5 deepest valleys.
	Rt	Total peak-to-valley height.
Spacing	Sm	Mean spacing between peaks.
	S	Spacing between similar profile points.
	Pc	Peak count per unit length.
Hybrid	Rsk	Skewness; asymmetry of profile.
	Rku	Kurtosis; sharpness or flatness.
Material Ratio	Rmr	% of profile above a certain level.
	Rk	Core roughness depth (plateau).
	Rpk	Reduced peak height.
	Rvk	Reduced valley depth.

II.2.2. Surface Measurement Techniques

Surface roughness can be evaluated using a range of metrological techniques, which are broadly classified into contact and non-contact methods, each with specific advantages depending on material properties and application requirements [59–61].

Contact Profilometers (Mechanical): Contact profilometers employ a stylus with a sharp diamond or carbide tip that physically traverses the surface under controlled loading. As the stylus moves laterally, vertical displacements corresponding to surface irregularities are recorded, generating a 2D profile of the scanned line. Parameters such as Ra, Rq, and Rz are computed from these profiles.

While highly standardized and widely used, stylus-based methods can introduce surface scratches, especially problematic when measuring soft, brittle, or highly polished materials, and are limited to relatively flat geometries.

Non-Contact Profilometers (Optical): Non-contact systems, such as confocal microscopes, laser triangulation sensors, and white light interferometers, measure surface topography without physical contact. These systems project a light beam, typically a laser or broadband white light, onto the surface and use detectors to analyze the phase shift or intensity variation of the reflected signal. Such methods are advantageous for fragile, compliant, or highly reflective materials where stylus-based contact may distort or damage the surface. They also allow fast scanning over complex or 3D geometries.

Interferometry: Interferometry provides sub-nanometer vertical resolution and is especially suited for assessing flatness and micro-waviness. By analyzing interference fringes formed between a reference wavefront and the wave reflected from the test surface, phase-shifting interferometry or coherence scanning interferometry can reconstruct high-resolution surface maps. These systems are ideal for ultra-flat surfaces, such as optical components or silicon wafers, where form deviation in the nanometric regime is critical.

Atomic force microscopy (AFM): AFM offers ultra-high resolution (down to ~0.1 nm in vertical displacement) and is capable of imaging surface morphology in three dimensions. It operates by raster-scanning a sharp tip mounted on a flexible cantilever across the surface. Interatomic forces between the tip and sample cause cantilever deflection, which is measured by a laser beam reflected into a photodetector. AFM is particularly valuable in nanotechnology, where precise surface features at the atomic or molecular level must be characterized.

II.3. Brittle Material Machining: Removal Mechanisms

Machining brittle materials requires a fundamentally different approach compared to ductile metals, due to their distinct fracture behavior under mechanical loading. Instead of undergoing plastic deformation, these materials tend to fracture when subjected to stress, resulting in specific and often undesirable surface phenomena during machining. [62]

By establishing the underlying behaviors and fracture responses, it becomes possible to understand the mechanisms through which material is removed and the mechanisms that directly influence surface quality and defect formation. and how brittle materials respond to mechanical actions in ultra-precision machining.

II.3.1. Physical Behavior of Brittle Materials

Brittle materials, including ceramics and glass, demonstrate a distinct mechanical behavior characterized by a linear stress–strain response and the absence of plastic deformation; as shown in Figure II.2. When subjected to mechanical loading, these materials exhibit a proportional increase in strain with stress, following Hooke's Law ($\sigma = E \cdot \varepsilon$), where σ is stress, ε is strain, and E is the modulus of elasticity [62]. This linear elastic behavior persists until the material reaches its fracture strength. Unlike ductile materials, brittle materials do not undergo significant yielding or permanent deformation; instead, they fracture abruptly once their elastic limit is exceeded [63]. This failure occurs at relatively low strain levels, indicating their inherently low ductility. Moreover, brittle materials generally exhibit high hardness due to strong interatomic bonding and dense crystal structures [64].

This high hardness enhances their resistance to scratching and wear but also makes them vulnerable to sudden and catastrophic fracture under tensile stress [62]. The combination of high hardness and low plasticity makes brittle materials suitable for applications requiring compressive strength and surface durability but unsuitable for environments involving impact or tensile loading.

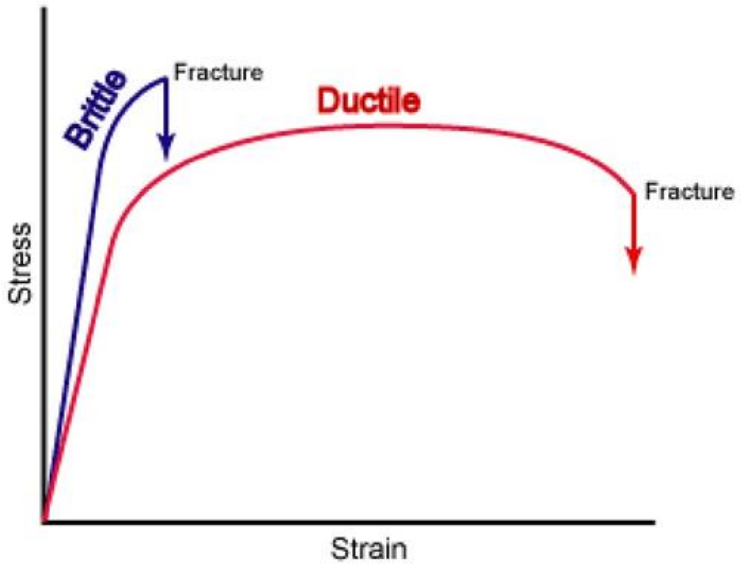

Figure II.2. Stress-strain curves. [65]

II.3.2. Material Removal Modes in UPM

In ultra-precision machining (UPM) of brittle materials, the material removal process largely depends on the material's response to mechanical forces. These materials, characterized by their high hardness and low ductility as previously explained, primarily behave differently from ductile materials during machining. However, understanding and controlling the interaction between the tool and the material is essential to achieve the desired material removal while minimizing defects. There are several modes through which material is removed during UPM, particularly when machining brittle materials, and these can be categorized into ductile and brittle modes, with the critical cutting depth being the defining factor.

The material removal mechanisms are mainly governed by three distinct modes.

a) Brittle Mode

Brittle mode machining removes material through fracture, the dominant mechanism for brittle materials under machining conditions. These materials, which include a wide range of ceramics and other hard substances, lack the ability to undergo significant plastic deformation and, instead, tend to crack or break under stress. Surface and subsurface cracks accompany the removal of material, resulting in a degraded finish and poor surface quality. Such a machining process is undesirable, particularly in high-precision applications, because it not only reduces the quality of the finished surface but also increases tool wear and the need for costly post-processing to address the induced defects. As the cutting depth increases, the likelihood of brittle fracture grows, exacerbating these issues and highlighting the need for careful control of machining parameters to prevent this mode of material removal. [66, 67]

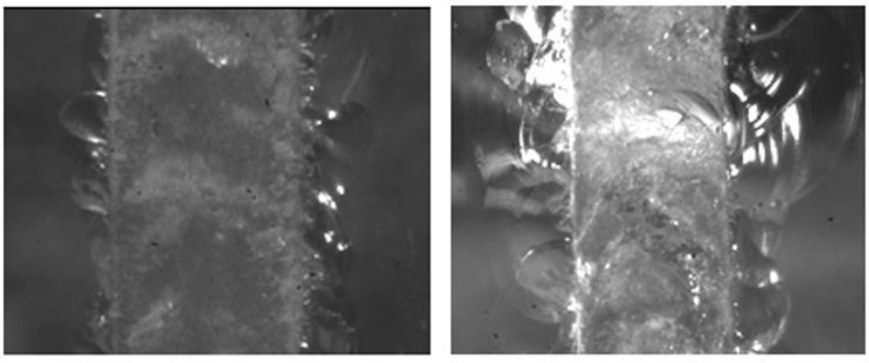

Figure II.3. Surface morphology of glass machined under brittle mode. [68]

As shown in Figure II.3, machining under brittle mode conditions results in extensive surface damage, including visible cracks and edge chipping. This pattern of material removal is governed by fracture propagation, where the cutting forces exceed the material's fracture toughness, leading to unstable crack growth and degraded surface quality. Such morphology confirms the undesirable nature of brittle mode machining for precision applications. [68]

b) Ductile Mode

Ductile mode machining represents an ideal material removal process for brittle materials, as it involves plastic deformation rather than fracture. In this mode, the material flows smoothly during cutting, resulting in a much higher-quality surface with minimal subsurface damage. Achieving ductile behavior in brittle materials requires precise control over machining conditions such as cutting speed, feed rate, and depth of cut as previously explained in chapter I. When properly controlled, these factors allow the material to deform plastically, thereby avoiding the formation of cracks and ensuring a smoother finish. Advanced tools are essential in this process, as they facilitate the achievement of high precision and excellent surface quality. This mode is particularly beneficial for ultra-precision machining, where surface integrity is critical, as it allows for the production of high-quality parts with minimal need for additional finishing. [69,70]

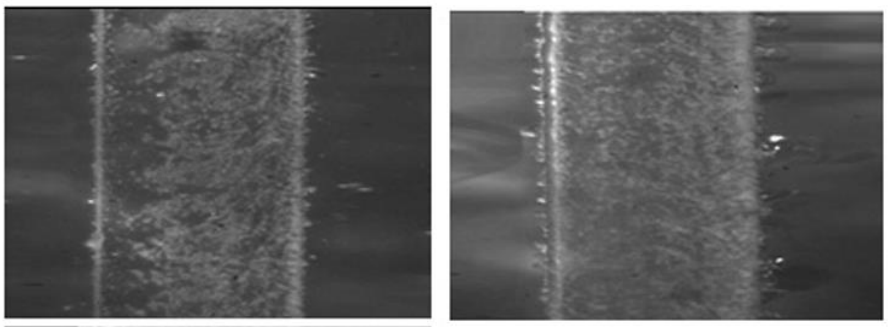

Figure II.4. Surface morphology of glass machined under ductile mode. [68]

In contrast, Figure II.4 demonstrates the smoother surface obtained when machining in ductile mode. The absence of major cracks and the uniform surface texture indicate that the material was removed primarily through plastic deformation rather than fracture. This confirms the advantage of operating below the critical chip thickness to maintain surface integrity and reduce subsurface damage.

c) Transition from Brittle to Ductile Mode

The transition from brittle to ductile mode is a key factor in optimizing the machining of brittle materials. Adjusting machining parameters causes the material to transition from fracture-dominant behavior to plastic deformation. A critical parameter in this process is the critical chip thickness, which dictates whether the material will undergo brittle fracture or ductile flow. When the cutting depth is below this limit, the material typically exhibits ductile characteristics, resulting in a smooth, defect-free surface; see Figure II.5. However, exceeding this critical depth causes the material to fracture, leading to surface damage. In addition to the cutting depth, factors such as cutting speed and feed rate significantly influence this transition. Increased cutting speed and feed rates, when properly managed, encourage plastic deformation by reducing the stress that leads to fractures. Similarly, temperature and strain rate play important roles in promoting ductility. Research has shown that a controlled strain rates can facilitate the transition by reducing crack formation and improving the material's ability to flow plastically. [66,67,70-72]

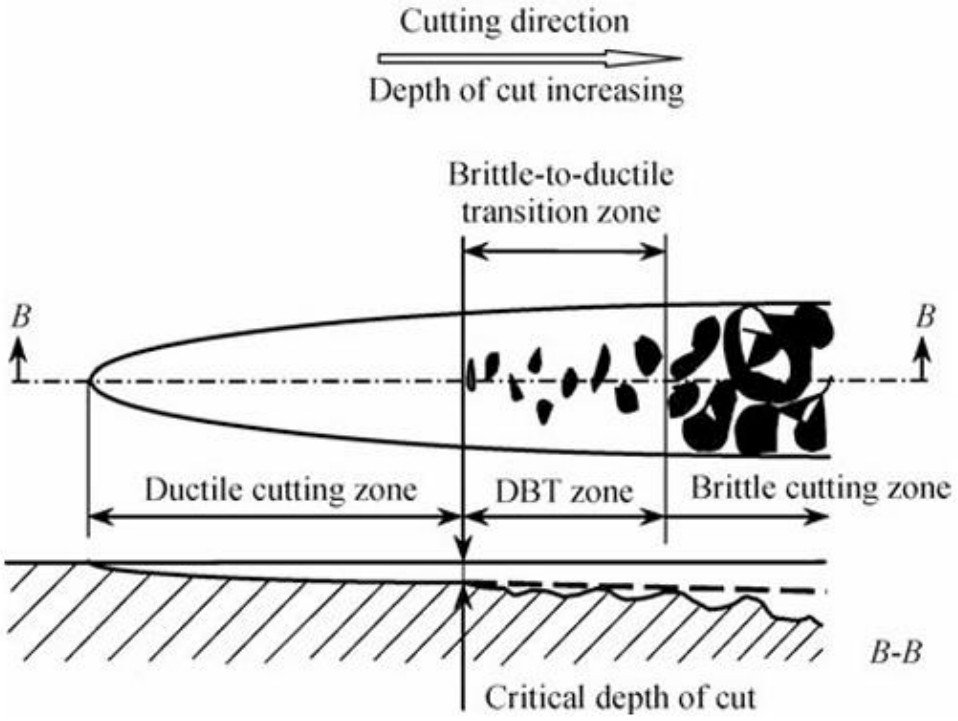

Figure II.5. Brittle to ductile fracture mode. [72]

II.3.3. Surface Damage Formation

The ultra-precision process involves the removal of material and surface irregularities and the production of a smooth surface as explained, which can lead to enhanced functional characteristics. The primary impact of these processes is seen in the improvement of surface finish, which can reduce the incidence of fatigue failures, corrosion, and wear in materials. However, excessive polishing can also lead to surface damage, such as micro-cracks or thermal distortion, which can adversely affect the material's strength and durability.

Microstructural changes in materials due to various manufacturing processes, including machining or finishing, are of significant interest in the field of materials science and engineering. These changes can have profound effects on the physical and mechanical properties of a material. Over-polishing or using inappropriate techniques can introduce microcracks and sub-surface damages (SSD). These defects can act as stress concentrators, adversely affecting the fatigue life and structural integrity of the material [73,74].

$$SSD = \max(c_m) \quad (1)$$

Where c_m is given by the following formula:

$$cm = 0.206 \frac{(E\,Hs)^{\frac{1}{3}}}{(Kc\,\beta)^{\frac{2}{3}}} (\tan\alpha)^{\frac{4}{3}} (cot\,\alpha)^{\frac{4}{9}} (hi)^{\frac{4}{3}} \quad (2)$$

where Hs (GPa) is the scratch hardness, Kc is the fracture toughness, and E is the material young's modulus. The SSD depth can be derived from the geometric relationship between the abrasive and the workpiece.

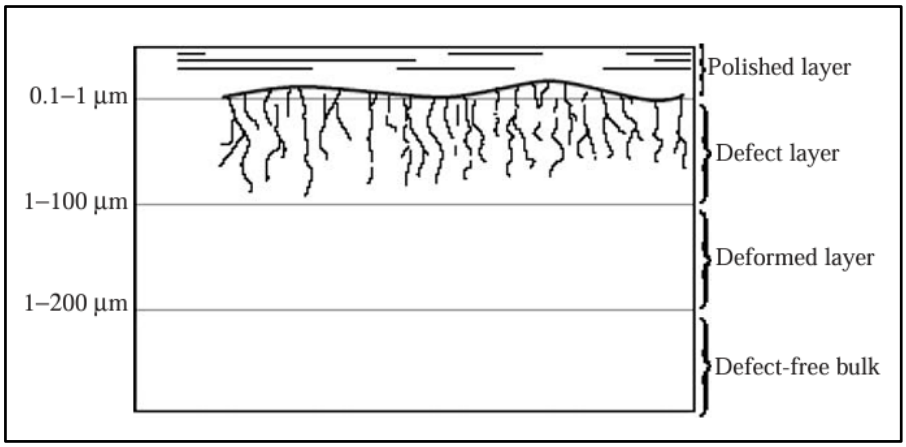

Figure II.6. Schematic of SSD (defect layer) in optical glasses. [73]

The diagram illustrates in Figure II.6, shows the typical subsurface structure of a brittle material following mechanical polishing or abrasive processing. At the very top lies the polished layer, which is usually between 0.1 and 1 μm thick. This superficial region appears smooth under optical inspection but may still contain ultra-fine surface roughness or micro-scratches that contribute to photon scattering in optical applications. Directly beneath the polished surface is the defect layer, which contains microcracks, fissures, and other forms of damage induced by the machining process. These defects can penetrate tens to hundreds of micrometers deep, depending on the material and the processing parameters. Below this is the deformed layer, which consists of plastically or elastically deformed material that may not show visible cracks but has altered mechanical and optical properties due to sub-critical stresses. Finally, the defect-free bulk lies beneath all disturbed layers, representing the original, undamaged material. This stratification is particularly critical in ultra-precision optical components, as both the defect layer and the deformed layer can alter the refractive index, introduce scattering centers, or initiate structural failure under optical or mechanical stress. As such, achieving minimal defect depth through optimized polishing and surface conditioning is essential for ensuring both optical clarity and mechanical stability in brittle materials.

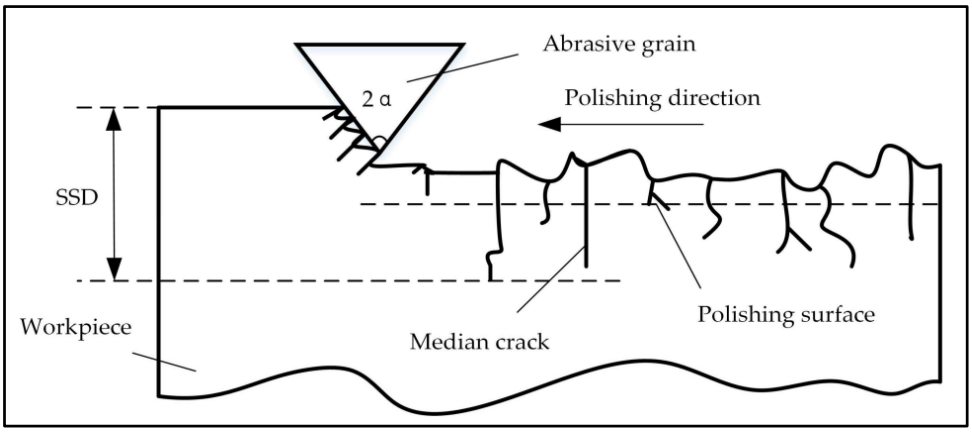

Figure II.7. Scratch process of single abrasive grain. [74]

Figure II.7 illustrates the interaction between an abrasive grain and a brittle workpiece during the polishing process, highlighting the formation of surface and subsurface damage (SSD). As the abrasive grain, typically of angular geometry, moves along the polishing direction, it penetrates the surface of the material at an angle (2α), generating both plastic deformation at the surface and cracks beneath it.

The immediate contact leads to the formation of median cracks, vertical or semi-vertical cracks that extend below the polishing surface into the subsurface region. These cracks are characteristic of brittle fracture and represent the onset of subsurface damage. Repetitive abrasive contact primarily removes the material through a combination of micro-fracture and lateral crack propagation. The figure also indicates that while the polishing surface appears smooth macroscopically, it is accompanied by underlying defects invisible to the naked eye but detrimental to optical and mechanical performance. The total depth affected by this damage is referred to as the SSD layer, which can vary depending on polishing parameters. This damaged zone can alter light transmission in optical components and reduce mechanical reliability, which emphasizes the value of minimizing SSD through optimized finishing techniques and post-polishing treatments.

II.4. Surface Quality and Its Functional Importance

Surface quality is a determining factor in the optical performance of machined components, particularly when working with brittle materials used in high-precision optics, such as glass, ceramics, or single crystals. Any imperfections introduced during cutting, lapping, or polishing, such as microcracks, pits, scratches, or residual surface stresses can significantly impact the way light interacts with the surface. Even nanoscale surface roughness can scatter incident photons, reducing light transmission and overall optical clarity [75].

Figure II.8, adapted from Medel-Ruiz et al. (2024), shows that increasing surface roughness in CdTe crystals leads to stronger Raman scattering signals. This experimental trend confirms that rough surfaces scatter more light, supporting the need to minimize surface roughness in optical components to enhance light transmission and reduce noise in optical systems.

This phenomenon is especially critical in applications such as laser optics, imaging systems, and photonic components, where high transparency and minimal optical loss are essential. When surface irregularities approach or exceed the wavelength of the incident light, they act as scattering centers, diffusing energy away from the intended optical path and thereby degrading resolution and contrast in imaging applications.

In some cases, machining can also induce subsurface damage, which alters the local refractive index and causes beam distortion or phase shifts, particularly in transparent optical components like fused silica.

These subsurface defects are difficult to detect but can have a cumulative effect on system performance, especially in laser applications where high fluence can exacerbate damage propagation. Therefore, achieving superior surface integrity characterized by nanometer-scale smoothness and the absence of both surface and subsurface defects is essential for maintaining high optical transmission, minimizing aberrations, and ensuring long-term stability and reliability of advanced optical systems. [76]

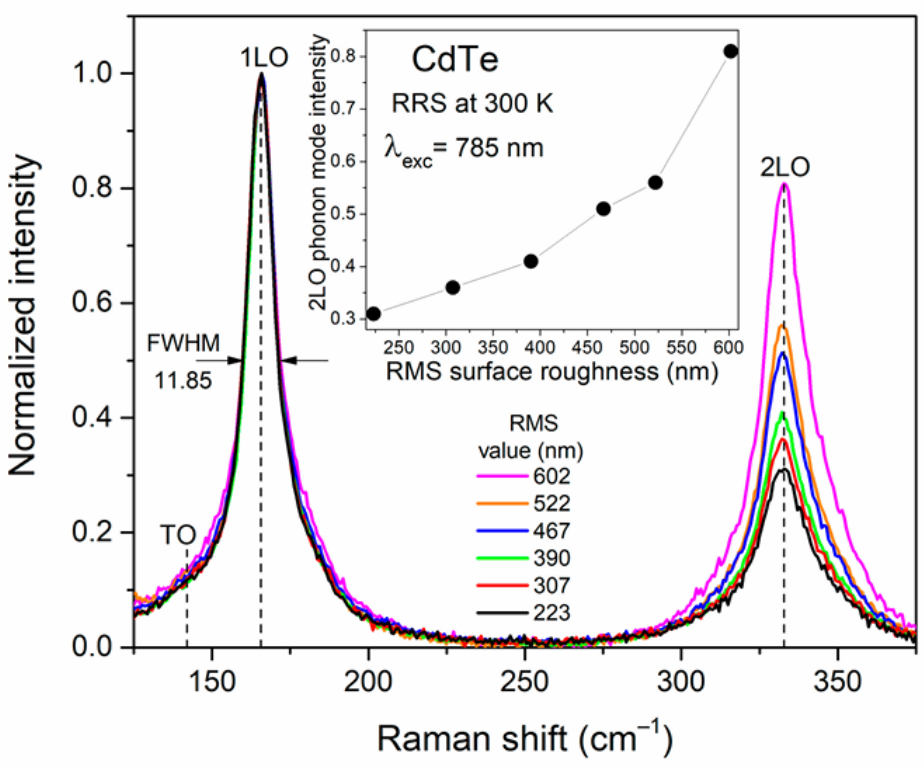

Figure II.8. Effect of surface roughness on Raman scattering intensity in crystal. [75]

II.5. Application Case Study: PET and TOF-PET Imaging Systems

II.5.1. Overview of PET Imaging

PET imaging is an abbreviation for Positron Emission Tomography [77,78], a medical imaging technique used in nuclear medicine, where an amount of radioactive materials called radiotracers are injected into the human body. Various radiotracers are used in PET imaging, and each has a specialized purpose based on its chemical structure and affinity for distinct biological processes [79,80]. This imaging technique aims to provide functional information about the physiological processes occurring within the body at the molecular and cellular levels.

In the natural decay of a radiotracer during positron emission tomography (PET), positrons are emitted and subsequently react with electrons in the body. This interaction produces energy in the form of a pair of photons, specifically gamma rays, a phenomenon known as annihilation, illustrated in Figure II.9. The annihilation process involves the mutual destruction of a positron and an electron, releasing energy that manifests as two gamma rays. Crucially, these gamma rays are emitted in opposite directions, each carrying an energy of 511 keV. This intricate process forms the foundation of PET imaging, where detecting these annihilation events enables the creation of detailed images depicting the spatial distribution of radiotracers within the body [81].

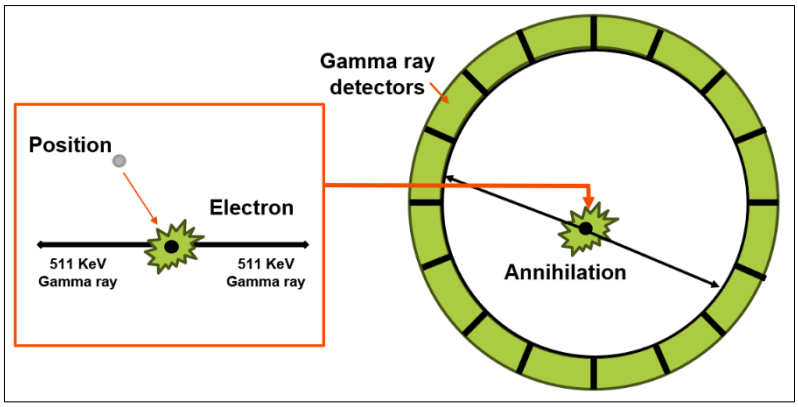

Figure II.9. Principal of the annihilation process in PET scanner.

Recording the concurrent detection of the two gamma photons produced during annihilation generates a response line, linking the detection locations. The response lines, which are aligned in a given direction, aid in creating a projection that shows how radioisotope activity is distributed in a plane perpendicular to this specified direction. By gathering a significant number of these occurrences, it becomes possible to recreate the whole activity distribution within the area captured in the images. The meticulous recording and analysis of coincident gamma photon detections form the basis of PET imaging. This process generates detailed and three-dimensional images, offering valuable insights into the physiological and pathological processes at the molecular level in the examined area. [77,78]

PET offers notable advantages as compared to other imaging techniques. One of its main advantages is its ability to provide functional information, showing metabolic activity inside tissues, which typical anatomical imaging modalities such as Computed Tomography (CT) and Magnetic Resonance Imaging (MRI) cannot be achieved.

The real-time insights provided by PET (Positron Emission Tomography) are precious for identifying illnesses and tracking treatment progress. PET has the notable benefit of enabling comprehensive imaging of the whole body, allowing thorough evaluations of several organ systems in a single scan. In addition, PET's ability to detect and measure biochemical and physiological changes provides a distinct viewpoint, particularly valuable in the field of oncology for the early detection of cancerous growths and the assessment of treatment effectiveness [82].

II.5.2. Time-of-Flight Enhancement in PET

Time-of-flight (TOF) is one crucial achievement that has contributed significantly to the improvement of imaging precision, as we look to the future of scanning technologies, given that PET imaging detects the response line where the destruction occurs, but does not identify which voxel on the response line is the source of two photons.

TOF PET enhances spatial resolution by precisely measuring the time it takes for emitted photons to reach the detectors, as shown in Figure II.10, which will allow the localization of the point of destruction along the line of response compared to PET imaging, which relies on coincident photon detection. Still, inherent timing uncertainties result in a less precise determination of the annihilation point [83-85].

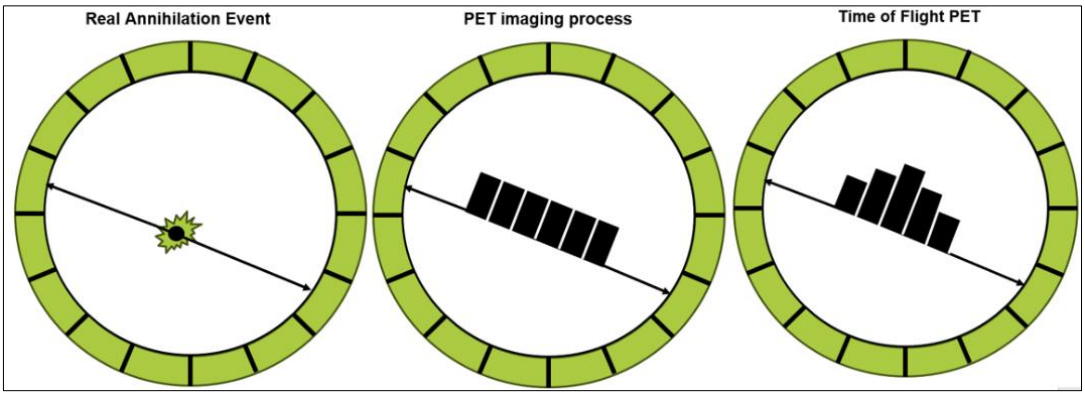

Figure II.10. Comparison between the localization of the point of destruction on the line of response.

One of the crucial parameters in time-of-flight (TOF) imaging is the coincidence timing resolution (CTR), which refers to the precision with which the time difference between the detection of two coincident gamma-ray photons can be measured.

This measurement of the time delay provides essential information for determining the location of the annihilation event along the line of response (LOR). A smaller coincidence timing resolution signifies a more accurate measurement of the time for the emitted photons to reach the detectors. This accuracy directly translates into the improved spatial resolution in TOF-PET, as shown in Figure II.11. The shorter the delay that can be reliably measured, the better the system can pinpoint the exact location of the annihilation event, resulting in higher spatial resolution and enhanced image quality. [83-85]

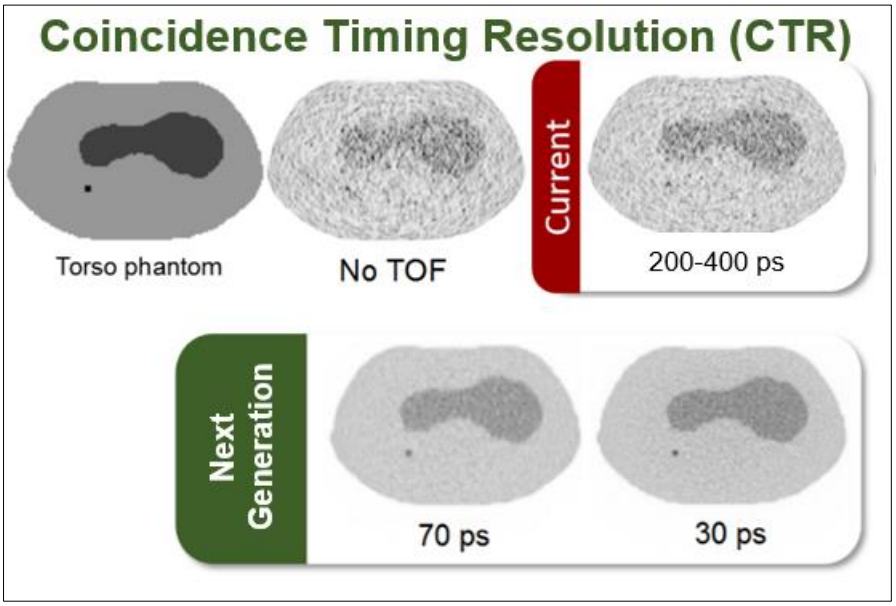

Figure II.11. Effect of CTR on the image quality obtained.

Scintillating crystals are materials with the unique ability to emit light, known as scintillation, upon interaction with ionizing radiation [86]. In the context of Positron Emission Tomography (PET) imaging, the intricate interaction begins when gamma photons intermingle with the scintillation crystal. In this interaction, the gamma photons impart energy to the crystal, inducing a state of excitement among the atoms nestled within the crystal lattice. This temporary but vital excitement stage is akin to the material absorbing the energy delivered by the gamma photons.

The ensuing phenomena unfolds as these excited atoms gracefully return to their original, more stable states, a process that releases photons of visible light as a form of energy dissipation. The wavelength of this emitted light holds a distinctive signature contingent upon the specific scintillation material employed. These emitted visible light photons, each carrying unique energy information, become the indicator signals of the initial gamma photon interactions.

The final act in this interplay involves detecting the emitted light by photodetectors. These detectors capture the nuanced signals, preparing the way for transforming complex scintillation events into data to generate high-quality PET images [87].

II.5.3. From Monolithic to Heterostructure Scintillators

a) Monolithic scintillator

A fundamental part of this technology is using Lanthanide elements in doping scintillator materials. Lanthanides are a class of elements distinguished by their remarkable luminous characteristics. They considerably improve the scintillation process when utilized as dopants in insulating materials. Doping the scintillator with lanthanide elements improves its efficiency in converting gamma rays to visible light, such as those incorporating Ce3+, Tb3+, Pr3+, and Eu2+/3+, are known for their high performance. [88]

A single, uniform crystal structure distinguishes these scintillators. While monolithic scintillators have advantages such as simplicity and ease of manufacture, they also have intrinsic limits. One significant problem is achieving high time resolution and spatial accuracy. Longer decay times can be caused by the regularity of the crystal structure, reducing the precision with which the system can estimate the time difference between the detection of coincident photons. This, in turn, impacts the capacity to precisely pinpoint annihilation events along the Line of Response (LOR).

There are several characteristics which describe the scintillator and which have a direct influence on its scintillation proprieties [87]:

- The stopping power of a scintillator, a crucial characteristic governing its capacity to decelerate charged particles, is intricately linked to the atomic number of the material comprising it. The atomic number, representing the number of protons in an atom's nucleus, significantly influences the scintillator's ability to interact with charged particles. In general, materials characterized by higher atomic numbers exhibit greater stopping power. This attribute is particularly advantageous in the context of positron detection. Positrons, as positively charged particles, undergo deceleration within the scintillator material. The heightened stopping power of scintillators with higher atomic numbers enhances their efficiency in capturing and slowing down positrons, a fundamental process in positron emission tomography imaging. The decay time of a scintillator is related to the transfer speed of free electrons and holes within the material.

Materials with higher atomic numbers may exhibit different decay times, and the presence of a slow component in the decay time can degrade the timing resolution of the scintillator.

- The extended decay times exhibited by monolithic scintillators represent an important aspect that have implications for the timing resolution of the imaging system. Timing resolution is a critical parameter in scintillation detectors, where the precise measurement of the time difference between coincident photons is essential as previously explained. The longer decay times inherent to monolithic scintillators introduces challenges in achieving the rapid response necessary for accurate temporal discrimination. This compromise in timing resolution impacts the system's ability to precisely timestamp events, potentially leading to reduced accuracy in reconstructing coincident events. Additionally, achieving optimal spatial resolution and uniform light output across the entire scintillator material presents further complexities. Spatial resolution is vital in imaging as it directly influences the system's ability to localize the origin of gamma photons. Challenges in maintaining uniform light output may result in variations in signal intensity, impacting the accuracy and precision of the localization process along the Line of Response.

b) Limitations of Lanthanide-Doped Insulators

The challenges in attaining ideal parameters for insulators doped with lanthanide elements in coincidence timing resolution are complex and varied.

The Figure II.12 illustrates the correlation between two essential variables: light output (measured in photons per megaelectron Volt) and decay time (measured in nanoseconds). To achieve optimal coincidence timing resolution, it is desirable for materials to possess both a high-light output and a short decay time. This combination enables accurate time-stamping of scintillation events. Which is limited in the case of Lanthanide-Doped Insulators.

To attain the "very demanding parameter space" means that achieving an optimal combination of high-light output, short decay time, and good energy resolution (as represented by the color gradient indicating the energy resolution) is arduous due to the physical qualities of the materials involved.

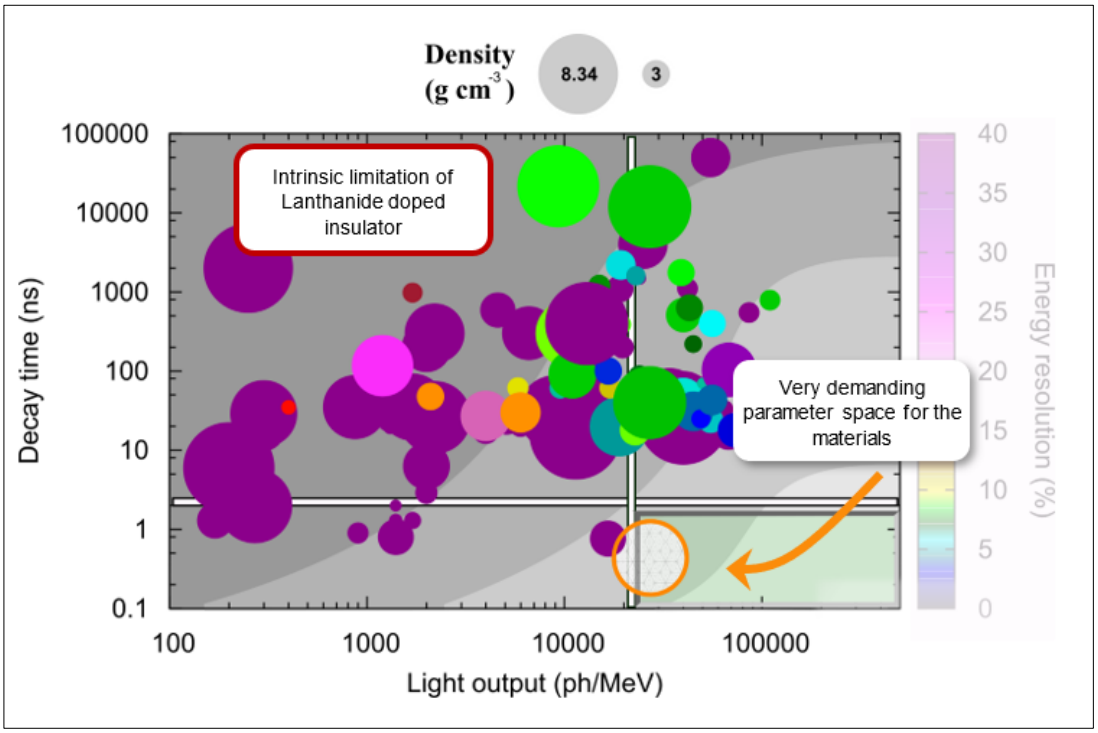

Figure II.12. Limitations in Achieving Optimal Parameters for Lanthanide-Doped Insulators in Coincidence Timing Resolution.

c) Heterostructure scintillator

Scientists have developed new designs focusing on heterostructures as a strategic solution to the difficulties of using Lanthanide-Doped Insulators (LDIs) [89-91]. The main goal of these designs is to address the inherent constraints of LDIs by utilizing the advantages of heterostructures.

The suggested technique needs incorporating the scintillation properties of two distinct materials into a heterostructure framework, which signifies a fundamental change in scintillation detector technology. Using the unique properties of various materials in the heterostructure design makes it easier and more accurate to time coincidence events in scintillation detectors. Therefore, incorporating heterostructures represents a promising breakthrough in scintillation detector technology.

The expected mechanism of a heterostructure scintillator, particularly in comparison to the favourable photoelectric effect, involves the synergistic interaction between its two components: the first component, the matrix, characterized by a short attenuation length, and the second component, the filler, known for its ultra-fast photon emission.

In the context of the photoelectric effect, where incident photons are absorbed, and electrons are ejected, the heterostructure scintillator aims to optimize this process for efficient photon detection and subsequent electron excitation. The short attenuation length of the matrix component is strategically designed to facilitate the prompt absorption of incident photons, minimizing the distance travelled before interaction. This characteristic is important for enhancing the probability of the photoelectric effect within the matrix. Once an incident photon is absorbed within the matrix, the liberated electrons are directed toward the second component, the filler. The rapid emission of photons by the filler upon interaction with the excited electrons ensures minimal delay in the scintillation process. Combining the short attenuation length of the matrix for efficient photon absorption and the ultra-fast photon emission of the filler for prompt scintillation, the heterostructure scintillator aims to optimize the photoelectric effect.

Figure II.13 outlines a visual representation detailing the anticipated scintillation process within a heterostructured scintillator. Scenario (a) The envisions gamma-ray conversion exclusively occurring in the matrix, emphasizing its efficiency in interacting with incident gamma photons. Conversely, scenario (b) illustrates a situation where gamma conversion is confined to the filler, highlighting its specialized role in converting gamma photons into scintillation events. Scenario (c) introduces a dual conversion process involving matrix and filler simultaneously. The subsequent elements, (i) "Gamma Conversion in Both Matrix and Filler," (ii) "Prompt Photon Emission," and (iii) "Electron Excitation for Enhanced Imaging Capabilities," collectively suggest a dynamic mechanism. This involves concurrent gamma conversion, immediate photon emission, and electron excitation, collectively contributing to the proposed enhanced imaging capabilities of the heterostructured.

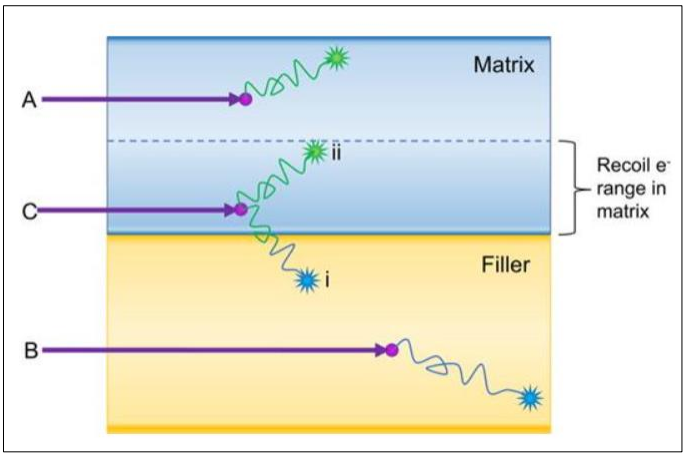

Figure II.13. Schematic Illustration of the Proposed Scintillation Mechanism in a Heterostructured Scintillator. [89]

II.5.4. Performance Analysis and Simulations

Some research proved improvements TOF PET imaging performance using Monte Carlo simulation software for heterostructures, it was found a coincidence time resolution (CTR) distribution of 204 ± 49 for layers of BGO and plastic (EJ232), compared to 276 ps that we considered for bulk BGO. [91]

Other researchers have extended the application of the Monte Carlo simulation, where the performance impacts were assessed by 1) altering the geometry and design of a BGO matrix and plastic scintillator structure. 2) Varying filler materials and design geometry in a BGO-based, long-axis fiber design. 3) Comparing BGO and LSO matrices using different fillers and geometries in a consistent design type. [92]

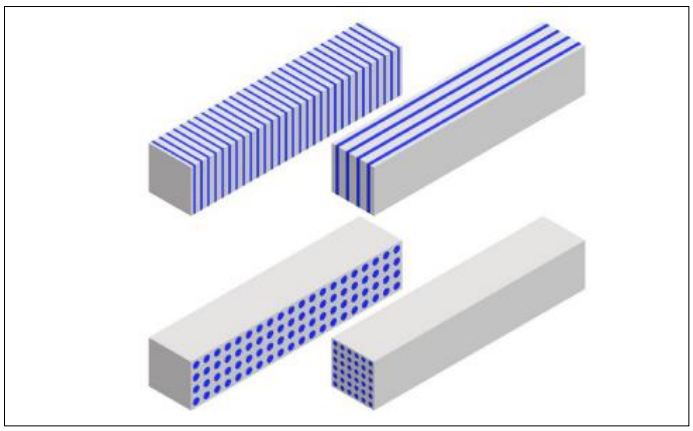

Figure II.14. Heterostructure designs: Plate stacking (upper) and fiber (lower) based structures. [92]

In a practical comparison between three different designs [93], a standard bulk BGO crystal, a layered BGO structure, and a heterostructure combining BGO with the EJ232 plastic scintillator. The heterostructure, which integrated BGO with EJ232 plastic scintillator, showed superior performance. the CTR was 239±12 ps. These finding underscore that the BGO and EJ232 plastic scintillator heterostructure, resulted in the most efficient CTR.

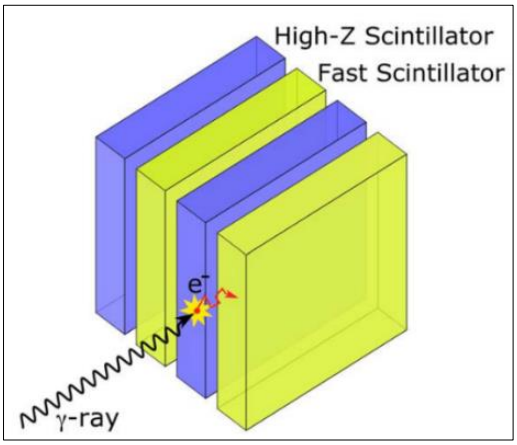

Figure II.15. Concept of layered heterostructure scintillators (plastic + single crystal). [93]

Other researchers have developed an innovative layered heterostructure, which is ingeniously combines a nanocomposite consists of a polystyrene matrix imbued with scintillating conjugated dyes and high-density nanoparticles with single crystal Bismuth Germanate (BGO), achieving a final CTR of 180 picoseconds (ps). [94]

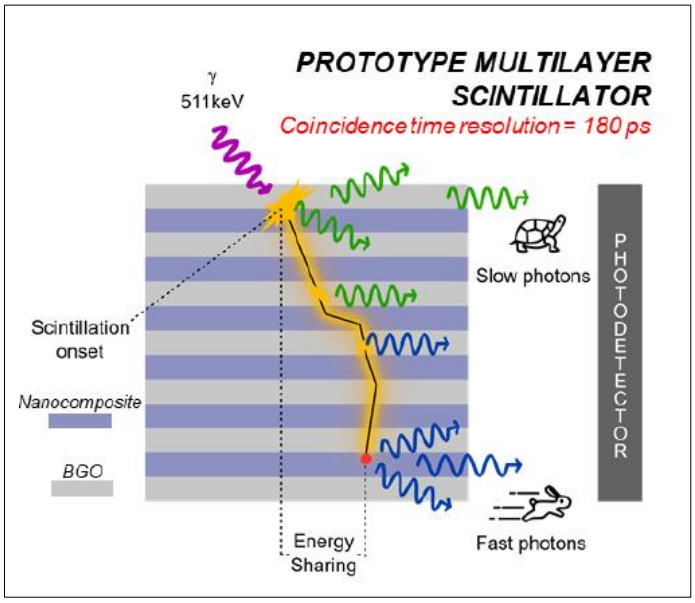

Figure II.16 Concept of layered heterostructure scintillators (nanocomposite films+ single crystal). [94]

a) Limitation of the Heterostructure Design

Implementing heterostructured scintillators poses significant challenges despite its promised advantages. It demands high precision at a micrometric scale poses intricate challenges in fabricating heterostructured scintillators.

The inherent hardness of such materials exacerbates issues of material cracking, leading to potential inaccuracies and reduced tool life during machining processes as previously discussed. Achieving a superior surface finish becomes a complex process, as the material's brittleness may induce microcracks and chips, compromising the quality of the scintillator's surface and, consequently, its performance. Addressing these challenges necessitates a deep approach, integrating a profound understanding of material properties with optimized machining parameters and advanced machining techniques, all crucial for ultra-precision machining of heterostructured scintillators.

b) Challenges of the Heterostructure Design

The challenge associated with the compatibility of two different materials to form a unique system in heterostructured scintillators is a multifaceted concern. Integrating distinct materials, such as a matrix and a filler, necessitates attention to their chemical, physical, and structural compatibility. Misalignment in these properties may lead to delamination, reduced adhesion, or even chemical reactions that could compromise the overall integrity of the heterostructure. Balancing the unique characteristics of each material while ensuring their harmonious coexistence presents a significant challenge in designing heterostructured scintillators.

II.6. Conclusion

This chapter has explored the essential role of high-quality surfaces in the performance and reliability of advanced technological systems. Moving beyond the generation of surface parameters discussed in Chapter I, the focus here has been on how surface quality directly influences functionality in precision applications, particularly in medical imaging and radiation detection.

Through the examination of Time-of-Flight Positron Emission Tomography (TOF-PET) and the evolution of scintillation materials, we have demonstrated that surface quality is not simply a manufacturing detail but a performance-determining factor. The transition from monolithic to heterostructured scintillators underscores the increasing demand for precise machining, surface control, and material compatibility in next-generation detector technologies.

Furthermore, the technical challenges associated with machining brittle, high-density single crystals and integrating heterogeneous materials call for continued research in ultra-precision finishing processes. These challenges directly relate to the accuracy, timing resolution, and overall efficiency of complex imaging systems.

In summary, this chapter highlights how surface quality is important in technological innovation. As imaging systems and detection technologies evolve, the demand for finely controlled, defect-free surfaces will continue to grow, reinforcing the central role of precision surface engineering in future scientific and industrial developments.

CHAPTER III

EXPERIMENT INSIGHTS FOR ULTRA-PRECISION PROCESSES

III.1. Introduction

This chapter provides a comprehensive and methodologically description of the experimental framework established to explore ultra-precision processes strategies for bismuth germanate (BGO) single crystals, which are essential for high-resolution radiation detection, especially in time-of-flight positron emission tomography (TOF-PET). This Chapter will demonstrate that BGO possesses exceptional scintillation properties, high density and optical clarity, rendering it essential for photon detection.

Nonetheless, its elevated hardness and reduced fracture toughness present significant challenges in precision machining, requiring specialized methods to maintain surface quality and optical performance. This chapter revisits the intrinsic properties of BGO that significantly influence its machinability, building upon the theoretical foundations of ultra-precision processes and brittle fracture behavior discussed earlier.

The experimental workflow is systematically outlined, including initial sample preparation steps such as wire saw cutting, precision lapping, and mechanical polishing. These steps aim to minimize surface defects. The polishing stage utilizes a statistically guided experimental design, allowing for controlled variation of parameters to enhance surface finish. Surface and optical characterization protocols are utilized to evaluate the impact of machining conditions on the physical quality and functional performance of the processed crystals. These evaluations are crucial for determining the relationships between surface quality and important application metrics in detector systems.

The present chapter establishes the essential connection among process parameters, material behavior, and performance metrics in ultra-precision machining (Milling and Drilling) of brittle BGO scintillator, acting as a crucial link between theoretical modeling and application-focused results discussed in the next chapters.

III.2. Material Properties of BGO and Its Implications for Ultra-Precision Machining

Bismuth Germanate (BGO) is a high-density scintillating crystal composed of bismuth oxide (Bi_2O_3) and germanium dioxide (GeO_2). As detailed in Chapters I and II, its unique combination of high atomic number constituents, high gamma-ray absorption, and favorable optical properties makes it particularly well-suited for use in Time-of-Flight Positron Emission Tomography (TOF-PET).

However, from a manufacturing perspective, BGO presents considerable challenges due to its mechanical characteristics, which directly influence its machinability and the required precision processing strategy.

The material exhibits a relatively high hardness (~500 kgf/mm² on the Vickers scale), combined with low fracture toughness (~0.67 MPa·m^½) and minimal ductility. These characteristics render BGO highly susceptible to brittle fracture, chipping, and subsurface crack propagation during mechanical machining. In addition, its moderate thermal conductivity (~3.5 W/m·K) limits the material's ability to dissipate heat generated during high-speed cutting or polishing, which can lead to localized thermal stresses and further exacerbate surface damage. These machining-induced defects are especially critical in TOF-PET applications, where surface quality directly influences optical coupling efficiency, light transmission, and ultimately, the detector's timing resolution.

Given these constraints, the selection of machining conditions, tool materials, and finishing protocols was carefully adapted to accommodate BGO's brittleness. Table III.1 summarizes the material parameters that were considered when defining the experimental protocol.

Table III.1. BGO Mechanical characteristics. [95,96]

DENSITY [G/CM3]	7.13
THERMAL EXPANSION COEFFICIENT [C-1]	7 x 10-6
HARDNESS (MOHS)	5
MODULUS OF ELASTICITY (E) [GPA]	105.4
POISSON MODULE	0.175
FRACTURE TOUGHNESS (KC) [MPA.M1/2]	0.67

To mitigate machining-induced damage, ultra-precision processing was conducted in multiple controlled stages. Initial sample preparation employed wire saw cutting with minimal mechanical loading, followed by fine lapping and low-pressure mechanical polishing. These steps were used to maintain machining forces below the critical stress intensity factor, thus preventing crack initiation. The brittle-to-ductile transition concept, as discussed in Chapter II, was a key consideration in determining the allowable depth of cut and abrasive grain size during polishing. By operating below the critical chip thickness, the material removal process remained within the ductile regime, reducing the formation of microcracks and subsurface defects.

In addition, the relatively low thermal conductivity of BGO necessitated the use of efficient cooling and lubrication strategies to prevent thermal damage. A suitable coolant was selected based on its ability to reduce friction, dissipate heat, and protect the crystal surface to prevent any chemical reactions. Tool materials were also chosen to match the hardness of BGO; to ensure high wear resistance, consistent cutting geometry, and minimal tool-workpiece interaction degradation over time.

These choices shaped the entire experimental methodology described in the subsequent sections of this chapter, including the polishing parameter matrix (Section III.3), tool selection and parameters for micromachining (Section III.4).

III.3. Preliminary Machining Processes for BGO

The initial preparation of Bismuth Germanate (BGO) samples involves a sequence of precision machining steps aimed at minimizing surface and subsurface damage before the final ultra-precision polishing stage. Given BGO's brittle nature and high hardness, each operation, cutting, lapping, and polishing, was carefully controlled to preserve surface quality and dimensional accuracy. This section outlines the experimental protocol for preparing all BGO samples used in subsequent surface and optical characterization experiments.

III.3.1. Wire Saw Cutting

Initial sample segmentation was carried out using a high-precision wire saw system (Princeton Scientific Corp., USA) equipped with a 0.05 mm diameter tungsten wire. Raw BGO blocks (see Figure III.1), were cut into cuboidal samples with nominal dimensions of 5 mm × 4 mm × 3 mm and an average mass of 0.4724 ± 0.0001 g. The surface roughness after cutting was approximately Ra ≈ 0.49 μm, as measured by contact profilometry.

To enhance the material removal rate and reduce tool-sample interaction forces, a slurry composed of silicon carbide (SiC) abrasive grains suspended in oil was used during cutting. The abrasive slurry increased cutting efficiency and minimized thermal and mechanical loading. Following sectioning, the samples were cleaned in an ultrasonic bath to remove residual abrasive particles and surface contamination.

Twenty-seven samples of identical dimensions were prepared to ensure experimental repeatability across all machining and characterization tests.

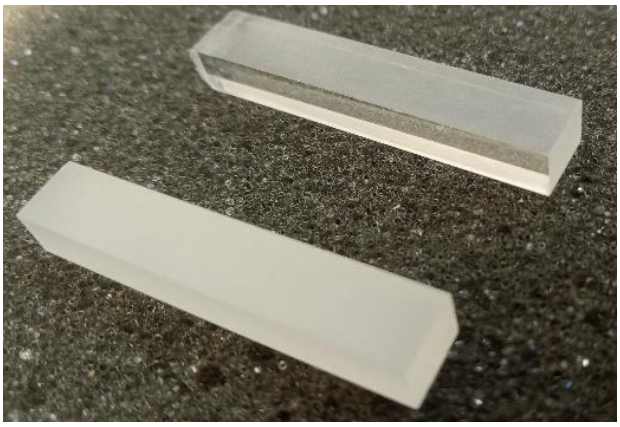

Figure III.1. BGO samples sourced from Hilger Crystals Ltd. (UK).

III.3.2. Lapping of BGO

After cutting, lapping process for the samples was done to eliminate saw induced scratches and reduce micrometric surface irregularities. Lapping was performed automatically using a progressively finer grit sequence of silicon carbide (SiC) abrasive papers: P800, P1200, and P2500. Each step was carried out under consistent process conditions, previously established through experimental laboratory work (as shown in Table III.2), to ensure uniform material removal and controlled surface refinement.

Table III.2. Lapping Parameters.

Lapping parameters	
Workpiece	
Type	BGO
Samples Number	9 * 3
Lapping Wheel	
Diameter	200 mm
Grains type	SiC (Silicon carbide): P800, P1200, P2500
Process Parameters	
Rotation speed	80 RPM
Applied Load	100 N
Time	5 min for each paper

III.3.3. Mechanical Polishing (Final Surface Preparation)

The concluding phase of sample preparation included mechanical polishing to attain the nanometric surface finish necessary for optical applications, especially in TOF-PET systems. A series of polishing experiments was carried out to evaluate the influence of three independent variables on key process outcomes, based on conditions previously established through experimental laboratory work.

- Grain type and size: 1 µm alumina, 0.3 µm alumina, 0.25 µm diamond.

- Applied pressures: 10 N, 15 N, 20 N.

- Rotational speeds include 50 RPM, 80 RPM, and 120 RPM.

Polishing was conducted utilizing a ChemiCloth M polishing pad, a porous synthetic cloth chosen for its consistent compliance and suitability with fine abrasives. To control for time as a confounding variable, all polishing runs were conducted for a standardized duration of 20 minutes. For polishing protocol, the Taguchi L9 orthogonal array design was used, facilitating an efficient investigation of the parameter space with a reduced number of experimental runs. Chapter IV provides a deeper look at the statistical and data analysis.

III.4. Ultra-Precision Machining Techniques and measurements Equipment

III.4.1. Micromachining of BGO

Ultra-precision machining of BGO samples was carried out using a Kern Evo Ultra Precision CNC Machining Centre, equipped with a 3-axis stage and designed to meet the sub-micron accuracy requirements essential for brittle material processing. This machine enabled precise tool control and high stability during both micro-milling and micro-drilling operations, making it particularly suitable for fabricating complex channel patterns in single-crystal scintillator slices. Two distinct machining approaches were implemented: Micro-drilling, for generating cylindrical holes, and Micro-milling, for machining semi-cylindrical channels across the surface.

The BGO samples used for the micromachining study, as described in Section 2-1, consisted of rectangular slices with dimensions of 20 mm × 3 mm × 0.3 mm, see Figure III.2.

Figure III.2. BGO slices used for micromachining tests.

Table III.3. Micro-Machining Parameters for Drilling and Milling of BGO.

PROCESS	TOOL TYPE	TOOL DIAMETER	SPINDLE SPEED (RPM)	FEED RATE (MM/MIN)	COOLANT
MICRO-DRILLING	Spotting Drill (Kyocera 130°)	0.2 mm	25,000	0.1 – 0.3	Mineral Oil
	Micro Drill (Union C-UMD)	0.15 – 0.4 mm	25,000	0.1 – 0.3	Mineral Oil
MICRO-MILLING	Diamond-Coated Ball Endmill (UDCBF)	0.2 – 0.4 mm	30,000	10 – 100	Deionized Water

For micro-drilling, a two-step approach was used: initial spotting with Kyocera 81 Series 130° carbide micro-spotting drills, followed by drilling with Union Tools C-UMD two-flute micro drills (Figure III.3.a), available in diameters of 0.15 mm, 0.25 mm, and 0.4 mm. Spindle speeds were maintained at 25,000 RPM, with feed rates ranging from 0.1 to 0.3 mm/min. A mineral oil coolant was applied to minimize thermal stresses and reduce tool wear.

For micro-milling, Union Tools UDCBF diamond-coated ball-nosed endmills were used with diameters of 0.2 mm, 0.3 mm, and 0.4 mm (Figure III.3.b). These tools were operated at spindle speeds of 30,000 RPM and feed rates varying from 10 to 100 mm/min. During milling, deionized water was employed as the coolant to aid in heat dissipation and to ensure clean cutting conditions.

Figure III.3. Union Tools a) drill bit b) Ball nosed end mill.

III.4.2. Surface Characterization

To evaluate the impact of UPM on the surface quality of BGO, a comprehensive surface characterization steps were applied.

High-resolution 3D microscopy was performed using a Keyence VHX-6000 digital 3D microscope at 20× magnification. This system enabled rapid visualization of machined features such as channel shape, edge sharpness, and surface chipping. It also provided precise measurements of channel dimensions and depth, supporting the evaluation of dimensional fidelity across machining conditions.

SEM imaging was conducted using a TESCAN Vega 3 electron microscope, operated at field-of-view scales of 50 µm and 500 µm. Prior to SEM analysis, all BGO samples were gold-coated to enhance surface conductivity and contrast. SEM provided detailed views of crack propagation, brittle fracture patterns, and tool-induced microfeatures on both the top surface and sidewalls of the machined channels. These images were further processed using ImageJ (FIJI distribution) for quantitative assessment where needed.

Surface roughness was measured using a Taylor Hobson Talysurf CCI white-light interferometer, with a 20× objective lens. Measurements focused on the root-mean-square roughness (Rq) and average roughness (Ra), which are critical indicators of optical quality. The roughness values were analyzed for both the unmachined top surfaces (between channels) and the internal surfaces of the channels themselves (sidewalls or bottoms), depending on the machining method. These metrics were essential for assessing the potential impact of surface defects on optical scattering and scintillation light transport.

Bruker Dektak XT stylus profilometer was used to measure the surface roughness, a high-resolution contact-based metrology instrument capable of nanometer-scale vertical resolution. This system operates by dragging a precision diamond-tipped stylus across the surface of the sample under a controlled force, typically in the millinewton range. As the stylus traverses the surface, it detects vertical displacements caused by surface irregularities, which are recorded and digitized to generate a detailed surface profile. The profilometer measures key surface texture parameters such as average roughness (Ra), root mean square roughness (Rq), peak height (Rp) and valley depth (Rv) over a defined scan length. In this study, the Dektak XT was configured with a scan length of 2 mm, a stylus force of 20 mg, and a resolution suitable for capturing surface features in the nanometric range.

The system's ability to accurately quantify surface topography made it ideal for evaluating the effectiveness of polishing protocols and comparing surface finishes across various machining conditions.

III.4.3. Optical Characterization

Transmittance measurements were performed using a UV1900i UV-VIS spectrophotometer (Shimadzu), which allows for high-precision optical analysis across a broad spectral range. To ensure repeatability and minimize alignment errors, each sample was carefully centered in the sample holder mounted on the instrument's optical bench. Measurements were conducted three times for each sample under identical conditions, and the average transmittance values were calculated and used to generate the final spectral curve.

Radioluminescence spectra were recorded using an X-ray generator (Inel XRG3000) that produces Bremsstrahlung X-rays by accelerating electrons at 35 kV onto a tungsten anode. The resulting scintillation light was transmitted through an optical fiber connected to a monochromator (SR500i-D2, Andor; 149 lines/mm grating blazed at 300 nm), and then detected using an Andor Newton EM-CCD camera (DU970P-UVB). Spectral measurements were corrected for system sensitivity using a calibrated tungsten lamp spectrum.

Pulse height spectra and coincidence timing resolution (CTR) measurements were performed using a custom test bench. Scintillator samples were optically coupled to either a 3×3 mm^2 Hamamatsu SiPM (S13360-3050CS) or a Broadcom SiPM. These were placed in coincidence with a 2×2×3 mm^3 LSO: Ce:0.4%Ca crystal, which was coupled to a 4×4 mm^2 SiPM from Fondazione Bruno Kessler (FBK). The CTR between the two detectors was measured at 61 ± 3 picoseconds, using a 3 MBq ^22Na radioactive source. The output signal from the SiPM was split to optimize both energy resolution and timing measurements.

III.4.4. Determination of BGO material properties

The BGO specimens used for the quasi-static test are 10 mm diameter and 10 mm height cylinders sourced from Hilger Crystals Ltd. (UK), see Figure III.4. (left). Quasi-static uniaxial compression tests were performed using an INSTRON 68FM-100 testing machine, operating at a crosshead speed of 0.12 mm/min, resulting in a strain rate of 2×10-4 s^{-1}. The top and bottom surfaces of the specimens were lubricated with silicone grease (RS Pro) to reduce the friction effect. The specimens were compressed until failure.

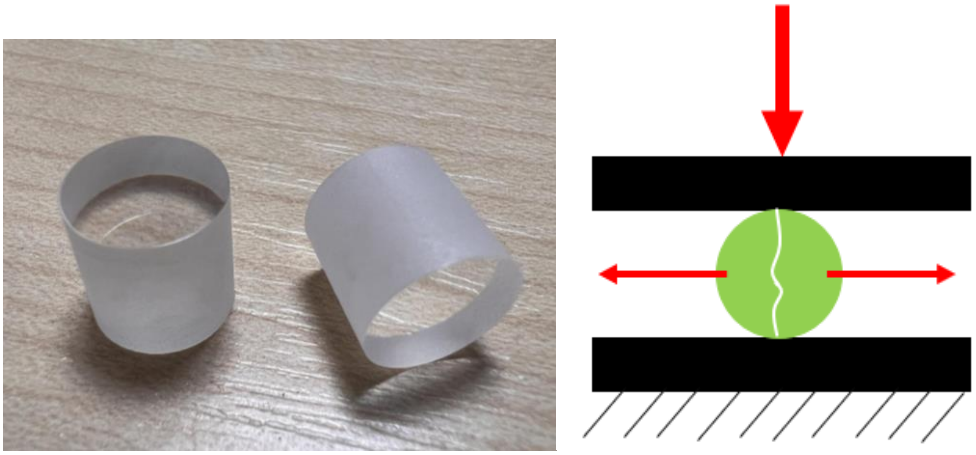

Figure III.4. (left). BGO specimens used for compression tests, **(right).** Diagram of the split test method.

To determine the ultimate tensile strength of BGO, a split test was conducted using the same machine. The loading rate during the test was maintained at 0.12 mm/min, and the peak pressure corresponding to failure was recorded. The splitting method is illustrated in Figure III.4. (right).

III.5. Conclusion

This chapter offered an in-depth review of the material selection, machining techniques, and equipment used for the ultra-precision machining and finishing of bismuth germanate (BGO) single crystals. The material properties of BGO, including its high hardness, brittleness, and low fracture toughness, were discussed, highlighting the challenges faced during its machining. These properties necessitate careful consideration in the selection of both the machining processes and the tools employed.

The chapter also explored the preliminary machining methods, such as wire saw cutting, lapping, and mechanical polishing, all of which were studied to minimize surface defects and damages. These techniques are crucial for preparing BGO for the more advanced, high-precision machining operations required for applications in fields like time-of-flight positron emission tomography (TOF-PET).

Furthermore, the advanced equipment used in these processes, including precision CNC machines and machining tools, was outlined, emphasizing the value of employing cutting-edge technology to achieve the sub-micron accuracy required in ultra-precision machining.

By understanding the material properties, techniques, and machinery detailed in this chapter, we can appreciate the complexities involved in ultra-precision machining and the importance of carefully chosen methods and tools to maintain the quality of BGO. The foundations laid here will be instrumental in the experimental results and simulations discussed in the next chapters.

CHAPTER IV

EXPEXPERIMENTAL PREPARATION AND PRELIMINARY MACHINING OF BGO SINGLE CRYSTAL

IV.1. Introduction

After establishing the theoretical principles of ultra-precision processes and the specific challenges encountered when machining brittle materials, this chapter initiates the experimental part of the study. It focuses on the results of the preliminary processes discussed in Chapter III necessary to ensure the success of high-precision operations.

Bismuth Germanate (BGO) single crystal was chosen for its unique combination of mechanical hardness and scintillation efficiency, which are critical for advanced applications such as Time-of-Flight Positron Emission Tomography (TOF-PET).

To prepare BGO for advanced machining, a sequence of preliminary operations was conducted, including wire sawing, lapping, and mechanical polishing. These processes were carefully selected based on the characteristics of BGO, such as its high hardness, brittleness, and ability to fracture, and were adapted to minimize the risk of surface and subsurface damage.

This chapter provides a detailed results analysis of the material surface quality that guided the process selection, explains the experimental strategies adopted to preserve surface quality, and lays the groundwork for the subsequent high-precision micromachining and modeling presented in the chapter V.

IV.2. Preliminary Machining of BGO Samples

IV.2.1. Wire Saw Cutting

The initial condition of the BGO crystal surface following wire sawing exhibited significant topographical irregularities, as illustrated in Figure IV.1. The microstructure is characterized by a high density of sharp micro-asperities, interspersed with fractured zones and micro-pits, indicative of a surface formed under brittle material removal.

Surface profilometry (Figure IV.2) quantitatively confirms this observation, revealing an average roughness Ra of 1.002 μm, with maximum peak height Rp = 2.68 μm, maximum valley depth Rv = 3.233 μm. These elevated values reflect a broad amplitude distribution, suggesting an unstable and uncontrolled surface state with high potential for subsurface damage.

The measured roughness parameters are well above the limit required for optical surfaces or sub-micron machining, confirming that the surface must undergo further refinement.

These initial measurements establish a critical baseline for evaluating the effectiveness of subsequent finishing stages in reducing surface roughness and improving optical readiness.

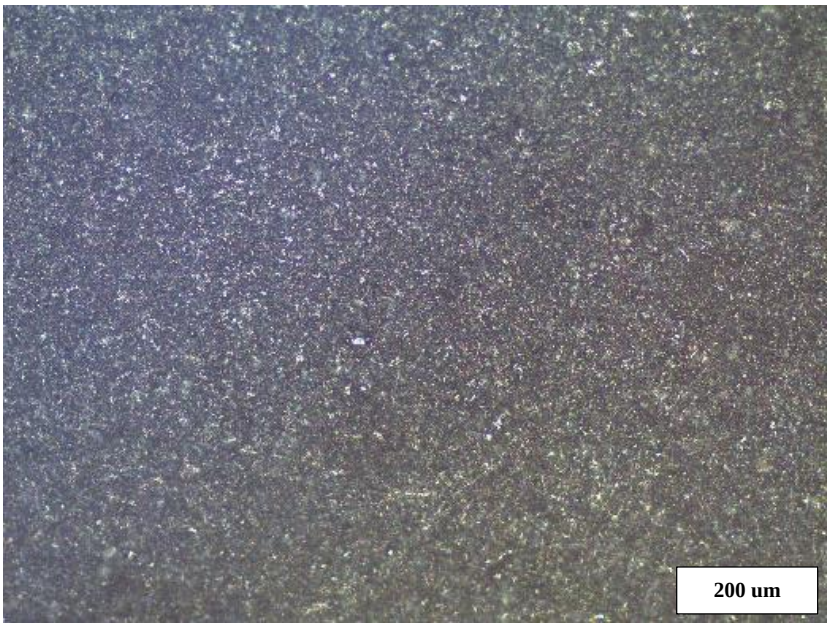

Figure IV.1. Microscopic view of the Rough BGO surface.

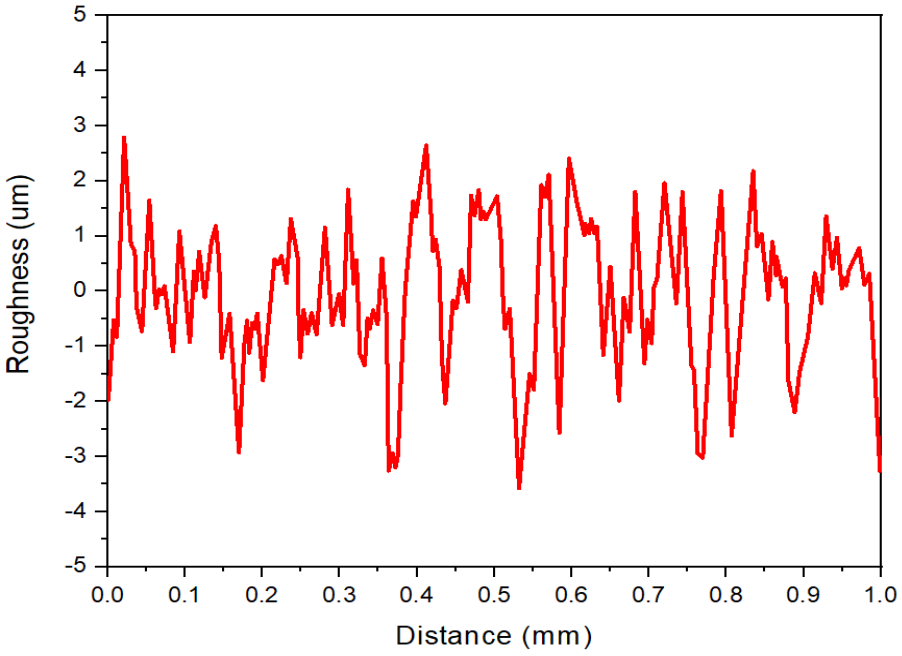

Figure IV.2. Surface roughness measurements for rough BGO surface.

IV.2.2. Lapping of BGO

Following wire saw cutting, the BGO crystal surfaces were subjected to a precision lapping process to reduce the surface roughness and mitigate the extent of subsurface damage induced by the initial cutting stage. The microscopic examination of the surface, as shown in Figure IV.3, reveals a dense scratch, predominantly aligned with the kinematics of the lapping path. These scratches have different depths and angles, suggesting that the material was removed unevenly due to the way the tool interacted with the workpiece, differences in the grain structure, and the natural brittleness of BGO.

The optical micrograph illustrates a surface that, while more uniform compared to the as-cut condition, still exhibits characteristic features of ductile-regime material removal transitioning to brittle fracture at isolated locations. The presence of intersecting grooves and micro-defects suggests that although lapping substantially reduces surface asperities, it does not entirely eliminate micro-cracks or chipping, which are particularly prevalent in hard and brittle single crystals such as BGO.

Quantitative surface profilometry results (Figure IV.4) confirm the improved but still moderately rough surface state. The average surface roughness Ra was measured at 70.264 nm, marking a significant improvement from the wire-sawn state (Ra = 1.002 μm). This reduction by approximately an order of magnitude indicates the efficacy of lapping in leveling the surface and removing large-scale topographical features.

However, the remaining roughness is still above the limit required for high-precision optical or photonic applications. Furthermore, the presence of sharp peaks and valleys in the profile trace points to residual brittle fracture events or embedded debris from the lapping process. These features may act as stress concentrators or optical scatterers if not subsequently addressed.

The current surface state therefore represents an intermediate stage in the overall machining chain. It highlights the transition from a fractured, irregular morphology toward a more planar and uniform structure. These findings underline the necessity of a subsequent polishing phase to achieve nanometric surface quality and to minimize sub-surface damage, which is critical for the intended use of BGO in high-performance scintillation and TOF-PET applications.

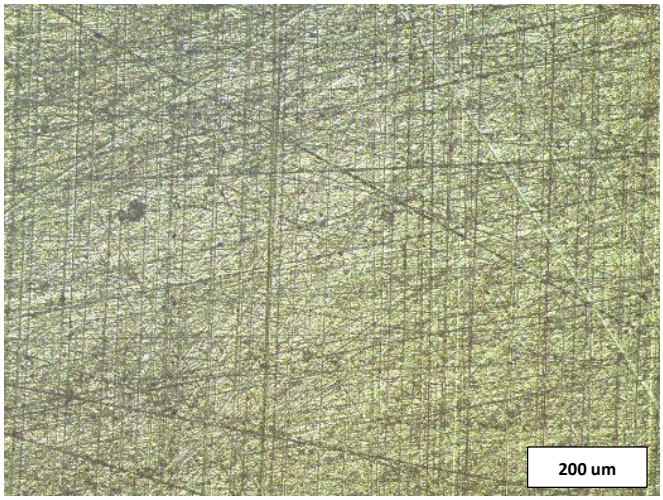

Figure IV.3. Microscopic view of the lapped BGO surface.

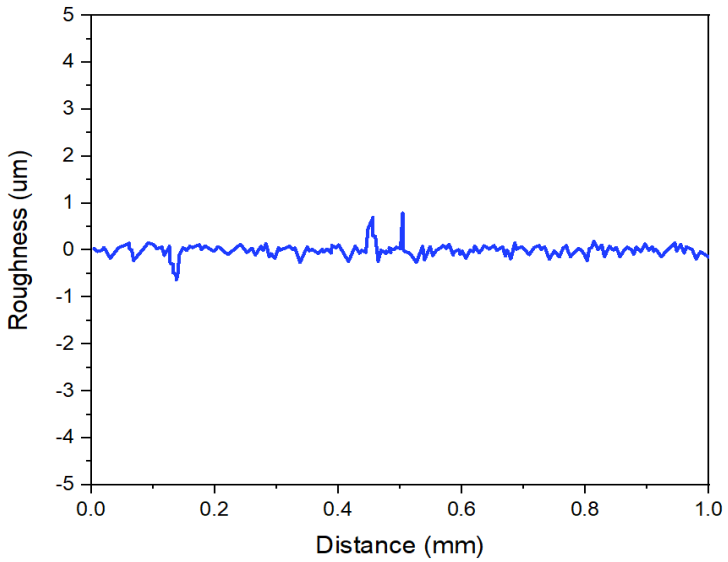

Figure IV.4. Surface roughness measurement after lapping.

IV.2.3. Mechanical Polishing (Final Surface Preparation)

Following wire sawing and lapping, the BGO samples retained a surface roughness of approximately Ra = 70.264 nm, with visible directional grooves and micro-fractures from the previous steps. To achieve optical-grade surface quality suitable for micromachining and subsequent characterization, a mechanical polishing process was implemented as the final stage of surface preparation. The objective was to reduce the surface roughness to the sub-10 nm range without inducing additional defects, particularly subsurface damage which could compromise both optical performance and material integrity.

To systematically optimize the polishing parameters, a Taguchi L9(3^3) orthogonal array design was selected. This statistical approach enables efficient screening of key variables, abrasive grain type, applied pressure, and rotation speed at three discrete levels each, across nine experimental runs. This method allowed the identification of optimal polishing conditions while minimizing experimental cost and time.

All surface roughness values were obtained using a Bruker Dektak XT stylus profilometer, with an instrument resolution of ±0.5 nm. Each average Ra value in the Taguchi matrix corresponds to the mean of three independent measurements performed after a fixed 20-minute polishing cycle per condition. To capture the temporal evolution of surface quality during polishing, time-resolved roughness measurements were also conducted at 5, 10, 15 and 20-minute intervals, offering insight into the dynamic material removal behavior.

Table IV.1. Taguchi L9 array with average Ra, standard deviation (σ), and S/N.

Nº	Grain Type	Pressure	Speed	Ra_1 (nm)	Ra_2 (nm)	Ra_3 (nm)	Ra Avg (nm)	σ (SD)	S/N Ratio (dB)
1	1 µm Alumina	10 N	50 RPM	11.13	11.00	11.16	11.03	0.07	-20.85
2	1 µm Alumina	15 N	80 RPM	7.31	6.96	6.96	7.01	0.20	-16.91
3	1 µm Alumina	20 N	120 RPM	4.80	4.63	4.39	4.48	0.21	-13.02
4	0.3 µm Alumina	15 N	120 RPM	3.41	3.21	3.21	3.30	0.11	-10.37
5	0.3 µm Alumina	20 N	50 RPM	5.63	5.20	5.24	5.58	0.24	-14.93
6	0.3 µm Alumina	10 N	80 RPM	4.54	4.62	4.94	4.70	0.17	-13.44
7	0.25 µm Diamond	20 N	80 RPM	5.58	5.84	5.79	5.74	0.13	-15.18
8	0.25 µm Diamond	10 N	120 RPM	5.04	4.84	5.22	5.03	0.19	-13.99
9	0.25 µm Diamond	15 N	50 RPM	4.05	4.09	4.25	4.13	0.11	-12.32

The S/N ratio for each trial was calculated using the "smaller-the-better" formula:

$$S/N = -10 \times \log_{10}((1/n) \times \Sigma(y_i^2)) \qquad (3)$$

Each polishing condition was visually and quantitatively analyzed using Ra vs. time curves and post-polishing microscopic imaging. Each sample's performance was assessed with time-resolved Ra values and microscopic observations.

Sample 01 (1 µm Alumina, 10 N, 50 RPM):

Over the 20-minute polishing cycle, Sample 01 shows a clear and continuous improvement in surface smoothness, reflected across multiple roughness parameters (Ra, Rq, Rp, Rv) measured in nanometers (nm).

Initial Phase (0–5 minutes):

The arithmetic average roughness (Ra) rapidly declines from approximately 72 nm to 27.4 nm, signifying effective elimination of prominent surface asperities. This is supported by decreases in peak height (Rp) from 171 nm to 30.4 nm and valley depth (Rv) from 70 nm to 24 nm, indicating a substantial smoothing of both peaks and valleys.

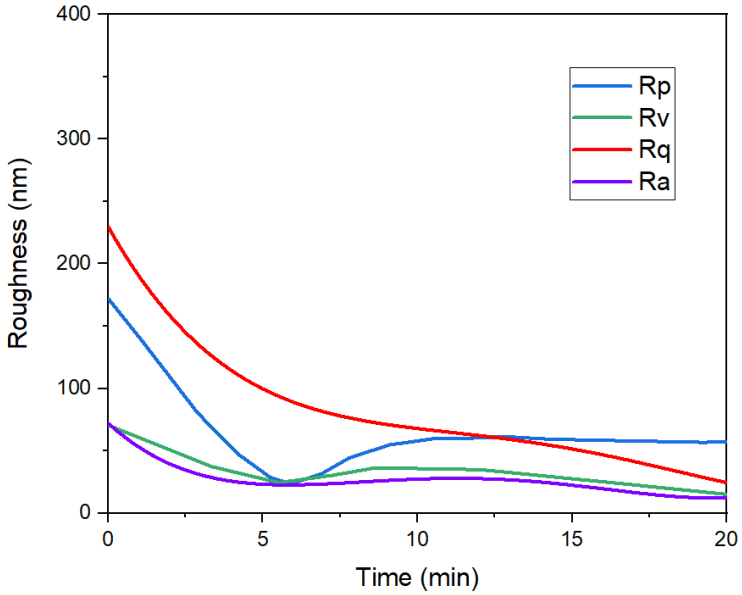

Figure IV.5. Surface roughness evolution curve of Sample 01 showing Ra, Rq, Rp, Rv values over 20 minutes of polishing.

Intermediate Phase (5–10 minutes):

Surface refinement continues as Ra falls to around 20–25 nm and the root mean square roughness (Rq) drops below 75 nm. The valley depth (Rv) follow similar downward trends, demonstrating homogenization of the surface profile and more uniform material removal.

The Rp parameter displays a notable increase between 9 and 15 minutes, peaking near 60 nm. This non-monotonic behavior suggests transient surface phenomena such as localized peak regeneration, microstructural changes, or variations in pad-abrasive interactions.

Such fluctuations may result from polishing pad deformation, abrasive particle embedment, or uneven pressure distribution.

Final Phase (15–20 minutes):

The parameters stabilize and show slight further reductions, with Ra reaching approximately 11 nm at 20 minutes. This parameter indicates a steady-state polishing regime with balanced material removal and surface finish improvement, free from re-roughening or defect formation.

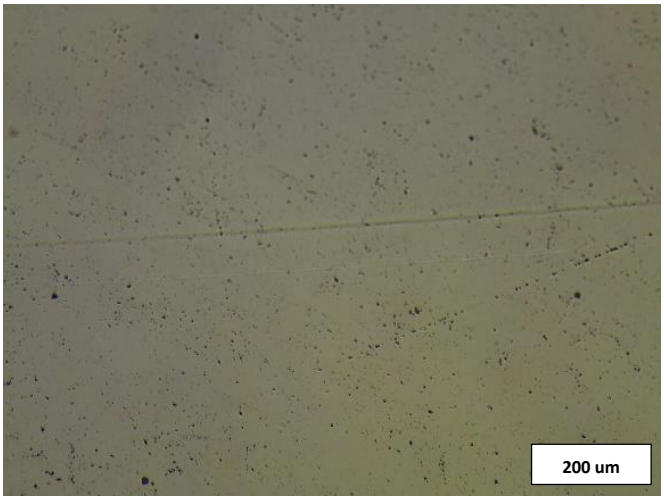

Figure IV.6. Optical micrograph of Sample 01 after polishing.

Microscopy (Figure IV.6) confirms a less uniform surface, not entirely free of deep scratches or pits. The scattered polishing debris do not compromise the overall surface quality, and the absence of subsurface damage underlines the effectiveness of the chosen polishing conditions.

This polishing strategy achieves a medium finish, reducing the Ra from approximately 72 nm to approximately 11 nm under the applied conditions. However, the value is slightly higher than the strict value of <10 nm, which is not ideal for ultra-precision application.

Sample 02 (1 µm Alumina, 15 N, 80 RPM):

The surface roughness evolution of Sample 02 during the 20-minute polishing cycle reveals a highly stable and monotonic improvement in surface quality, as evidenced by multiple profilometric parameters (Ra, Rq, Rp, Rv), all measured in nanometers (nm).

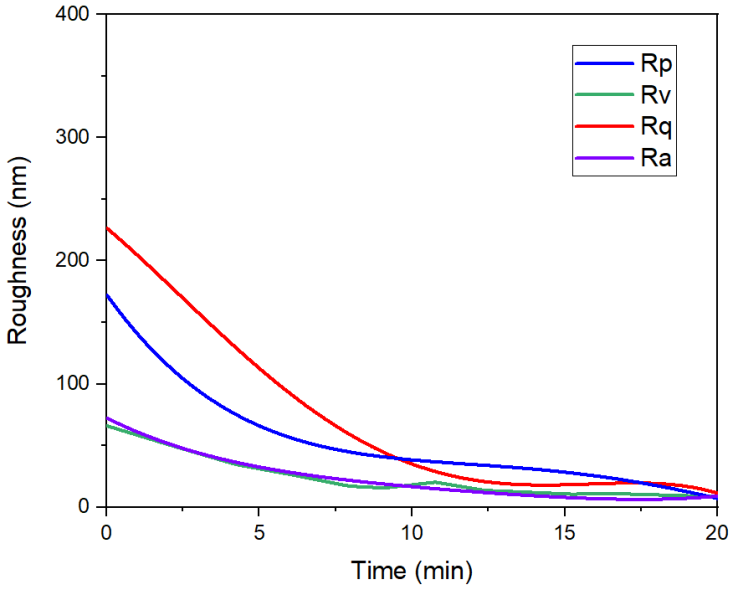

Figure IV.7. Surface roughness evolution curve of Sample 02 showing Ra, Rq, Rp, Rv values over 20 minutes of polishing.

Initial Phase (0–5 minutes):

The arithmetic average roughness (Ra) begins at approximately 75 nm but decreases rapidly to about 30 nm by 5 minutes, indicating a good removal of initial surface asperities and irregularities. The peak height (Rp) and valley depth (Rv) parameters also decrease markedly from approximately 167 nm and 66 nm, to 68 nm and 26 nm respectively, reflecting substantial smoothing of surface peaks and valleys.

Intermediate Phase (5–15 minutes):

Surface refinement continues to decrease as Ra reaches to around 17 nm. The peak height (Rp) and valley depth (Rv) also decrease consistently, with Rv reaching approximately 20 nm and Rp dropping to about 37 nm. This trend reflects uniform material removal and homogenization of the surface profile.

Final Phase (15–20 minutes):

Polishing culminates with Ra values stabilizing near 7.7 nm at 20 minutes. Rv and Rp reach approximately 8.6 nm and 8.2 nm, respectively, reflecting a smooth and leveled surface, confirming the effective reduction of both peaks and valleys. This stable plateau in roughness parameters indicates the establishment of a steady-state polishing regime characterized by balanced material removal and surface finish improvement.

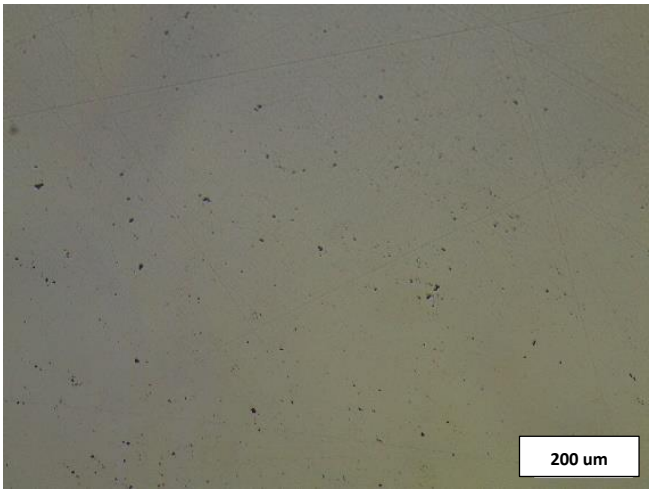

Figure IV.8. Optical micrograph of Sample 02 after polishing.

Microscopy (Figure IV.8) confirms the profilometric trends by displaying a homogeneous and defect-free surface with near-complete elimination of initial lapping lines. The surface appears smooth and uniform, with no evidence of new defects or damage induced during polishing.

This polishing protocol, using a higher load and speed compared to Sample 01, achieves a consistent and monotonic reduction in surface roughness, resulting in a near ultra-precision finish. The final surface quality, with Ra close to 7.7 nm, demonstrates the efficacy of the applied polishing parameters for producing high-quality finishes.

Sample 03: (1 µm Alumina, 20 N, 120 RPM):

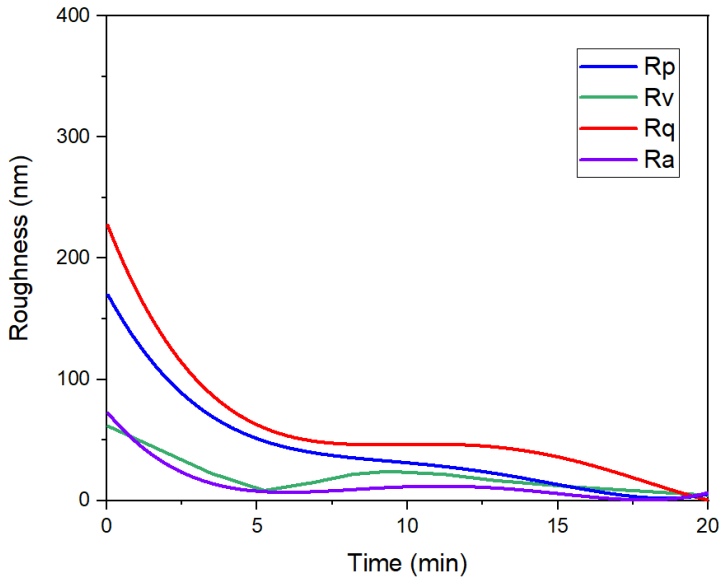

Figure IV.9. Surface roughness evolution curve of Sample 03 showing Ra, Rq, Rp, Rv values over 20 minutes of polishing.

Initial Phase (0–5 minutes):

The arithmetic average roughness (Ra) rapidly decreases from approximately 74 nm to about 25 nm, indicating efficient removal of initial surface asperities. This is accompanied by reductions in peak height (Rp) from roughly 160 nm to 100 nm and valley depth (Rv) from about 61 nm to 20 nm, reflecting significant smoothing of both surface peaks and valleys.

Intermediate Phase (5–10 minutes):

Surface roughness parameters continue to decrease steadily, with Ra approaching approximately 7 nm by 10 minutes. Rv and Rp reduce consistently to near 14 nm and 35 nm respectively. The root mean square roughness (Rq) also follows this downward trend. These decreases illustrate ongoing surface homogenization and controlled material removal, characteristic of an effective polishing regime.

Final Phase (15–20 minutes):

By the end of the polishing cycle, Ra reaches values close to 4 nm (within measurement resolution), while Rp approach minimal values near 7 nm. The valley depth (Rv) decreases to near 4 nm as well, confirming a near-ideal surface finish with virtually no deep valleys or peaks remaining.

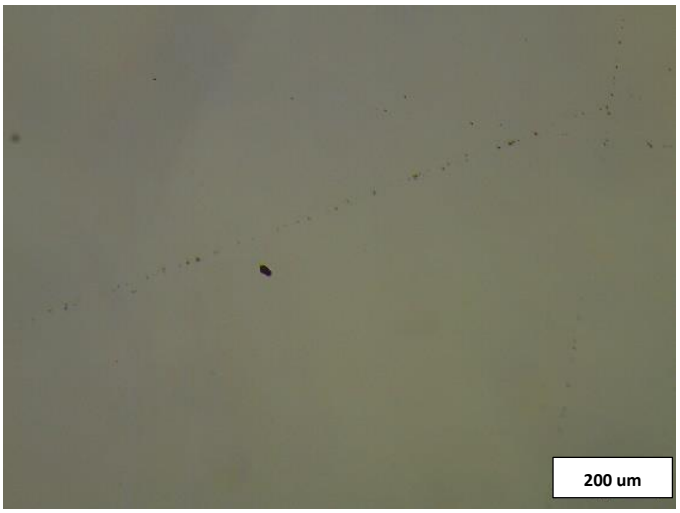

Figure IV.10. Optical micrograph of Sample 03 after polishing.

Microscopy (Figure IV.10) corroborates the profilometric data, revealing a smooth and uniform surface with minor residual polishing debris but no significant defects or scratches. The polishing process effectively removes previous machining marks, confirming the high-quality surface finish.

This polishing strategy, employing the highest speed among the samples, achieves rapid and uniform surface smoothness improvement, producing an ultra-precision finish well below 10 nm Ra.

Sample 04 (0.3 µm Alumina, 15 N, 120 RPM):

Initial Phase (0–5 minutes):

The arithmetic average roughness (Ra) decreases from approximately 47 nm to about 24 nm, reflecting rapid smoothing of prominent surface asperities. This is accompanied by decreases in peak height (Rp) from around 168 nm to 58 nm and valley depth (Rv) from about 64 nm to 40 nm, indicating effective smoothing of both peaks and valleys.

Intermediate Phase (5–10 minutes):

Surface roughness parameters continue to decline, with Ra falling to approximately 3 nm by 10 minutes. Rv and Rp follow a decreasing trend, reaching about 11 nm and 23 nm respectively.

Final Phase (15–20 minutes):

By 20 minutes, Ra approaches about 3 nm. The valley depth (Rv) and peak height (Rp) similarly decrease, confirming a smooth, homogenized surface profile. The polishing process reaches a regime with an ultra-precision finish facilitated by the finer abrasive size (0.3 µm alumina).

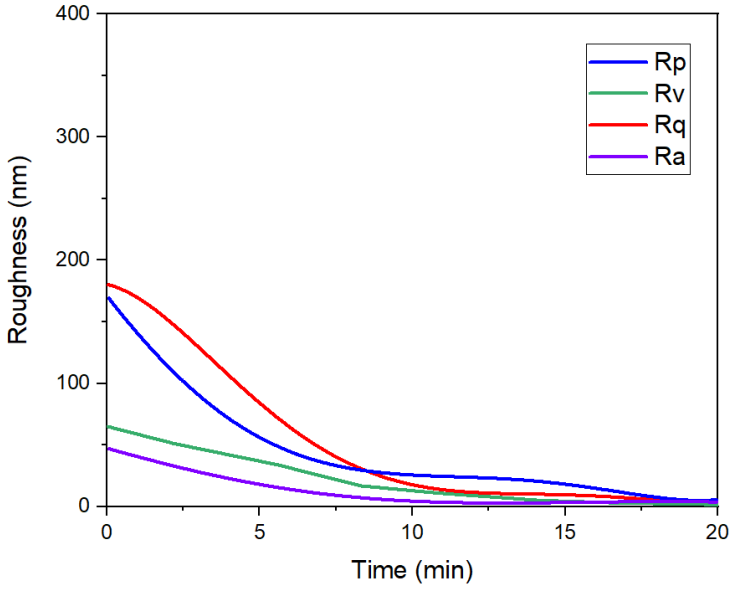

Figure IV.11. Surface roughness evolution curve of Sample 04 showing Ra, Rq, Rp, Rv values over 20 minutes of polishing.

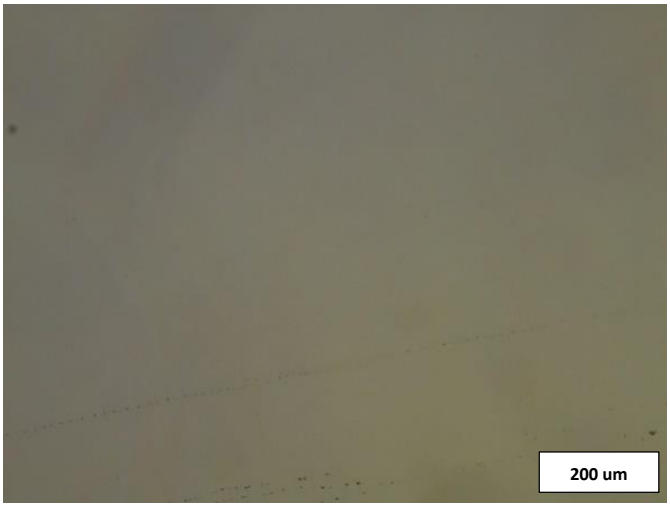

Figure IV.12. Optical micrograph of Sample 04 after polishing.

Microscopy (Figure IV.12) reveals a smooth, nearly defect-free surface with minimal polishing debris and almost complete removal of prior machining marks. This confirms the efficacy of the polishing parameters used.

The finer abrasive size combined with moderate load and high speed achieves a faster and finer surface finish compared to previous samples, making this approach ideal for ultra-precision applications.

Sample 05 (0.3 µm Alumina, 20 N, 50 RPM):

Initial Phase (0–5 minutes):

The arithmetic average roughness (Ra) decreases significantly from approximately 73.5 nm to about 23.55 nm within the first 5 minutes, indicating effective removal of coarse surface asperities. Concurrently, the peak height (Rp) drops from roughly 171 nm to 25 nm, and the valley depth (Rv) decreases from about 69 nm to 20 nm, reflecting substantial smoothing of surface peaks and valleys.

Intermediate Phase (5–10 minutes):

Surface roughness parameters continue their downward trend, with Ra approaching approximately 6.6 nm by 9 minutes. Rv and Rp decrease consistently to about 6 nm and 9 nm respectively. The root mean square roughness (Rq) follows a similar trend, declining from around 39 nm to 8.8 nm, indicating progressive surface leveling and homogenization.

Final Phase (15–20 minutes):

By the conclusion of polishing, Ra values stabilize around 5.2 nm, while Rv and Rp maintain low values near 3.55 nm and 8.6 nm respectively. Overall, the surface exhibits a high-quality finish with minimal roughness.

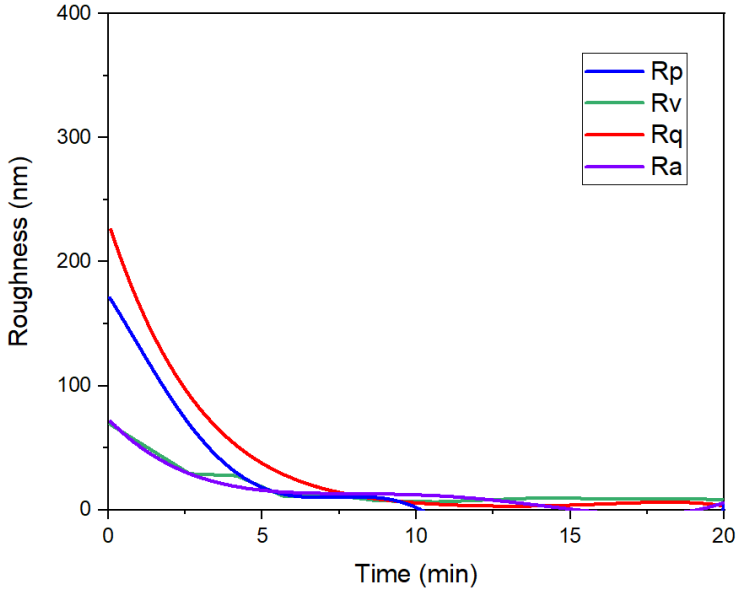

Figure IV.13. Surface roughness evolution curve of Sample 05 showing Ra, Rq, Rp, Rv values over 20 minutes of polishing.

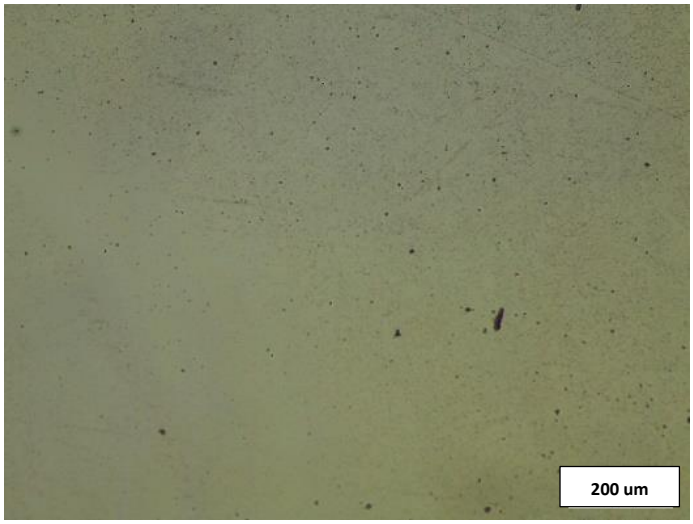

Figure IV.14. Optical micrograph of Sample 05 after polishing.

Microscopy (Figure IV.14) confirms a smooth, homogeneous surface with minimal polishing debris and the near-complete elimination of machining marks, indicating excellent surface quality.

This polishing regime, using a fine 0.3 µm alumina abrasive at a high load but moderate speed, effectively produces an ultra-precision surface finish suitable for demanding applications.

Sample 06 (0.3 µm Alumina, 10 N, 80 RPM):

Initial Phase (0–5 minutes):

The arithmetic average roughness (Ra) decreases notably from approximately 70 nm to about 19 nm within the first 5 minutes, indicating rapid smoothing of initial surface asperities. Peak height (Rp) reduces from around 171 nm to 47 nm, while valley depth (Rp) drops significantly from about 171 nm to 50 nm, showing effective removal of both peaks and valleys.

Intermediate Phase (5–10 minutes):

Surface roughness parameters continue to decline with Ra approaching 20 nm by 10 minutes. Rv and Rp show a gradual decrease, with both Rv and Rp near 40 nm. The root mean square roughness (Rq) follows a similar decreasing trend, confirming progressive surface leveling.

Final Phase (15–20 minutes):

By the end of polishing, Ra stabilizes around 4.8 nm, and Rv and Rp decreases substantially to approximately 5 nm. Other roughness parameters also reach low values, confirming a smooth and uniform surface finish.

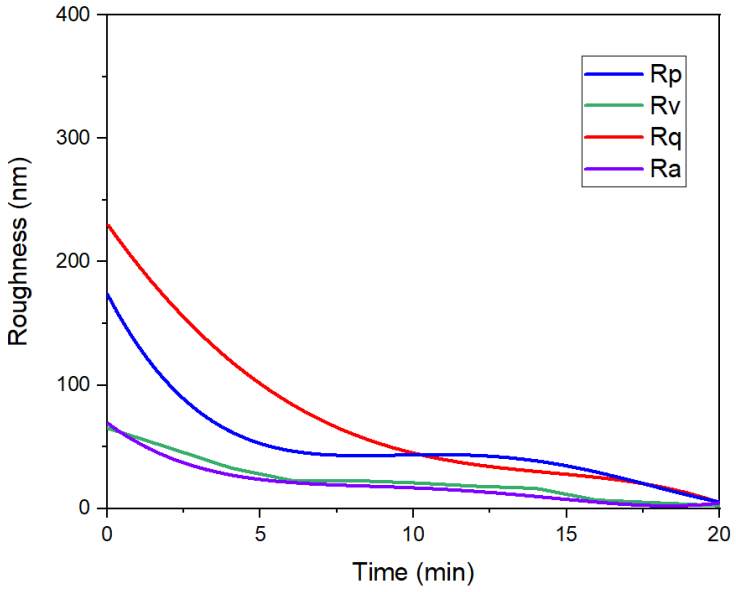

Figure IV.15. Surface roughness evolution curve of Sample 06 showing Ra, Rq, Rp, Rv values over 20 minutes of polishing.

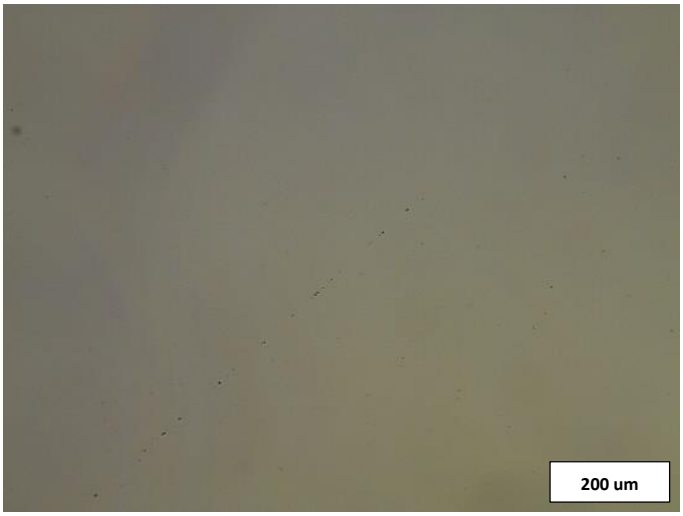

Figure IV.16. Optical micrograph of Sample 06 after polishing.

Microscopy (Figure IV.16) corroborates with the findings, displaying a smooth surface with minimal defects and polishing debris, and effective removal of initial machining marks.

This polishing regime, employing a fine 0.3 µm alumina abrasive with moderate load and speed, produces an effective surface finish.

Sample 07 (0.25 µm Diamond, 20 N, 80 RPM):

Initial Phase (0–5 minutes):

The arithmetic average roughness (Ra) decreases from approximately 79 nm to about 15 nm within the first 5 minutes, indicating effective removal of prominent surface asperities. Peak height (Rp) decreases from about 169 nm to approximately 25 nm, while valley depth (Rv) declines markedly from around 66 nm to 27 nm, reflecting substantial smoothing of peaks and valleys.

Intermediate Phase (5–10 minutes):

Surface roughness continues to decline but with minor fluctuations. Ra stabilizes near 14 nm, while Rp, and Rq show slight variations but trend downward overall. This behavior indicates ongoing surface refinement but suggests some transient variations potentially due to polishing dynamics or measurement sensitivity. The valley depth (Rv) decreases steadily, indicating continued smoothing of surface valleys.

Final Phase (15–20 minutes):

By the end of polishing, Ra reaches approximately 5.5 nm, and Rp decreases further to about 10 nm. Other parameters similarly decline, confirming a smooth, near defect-free surface.

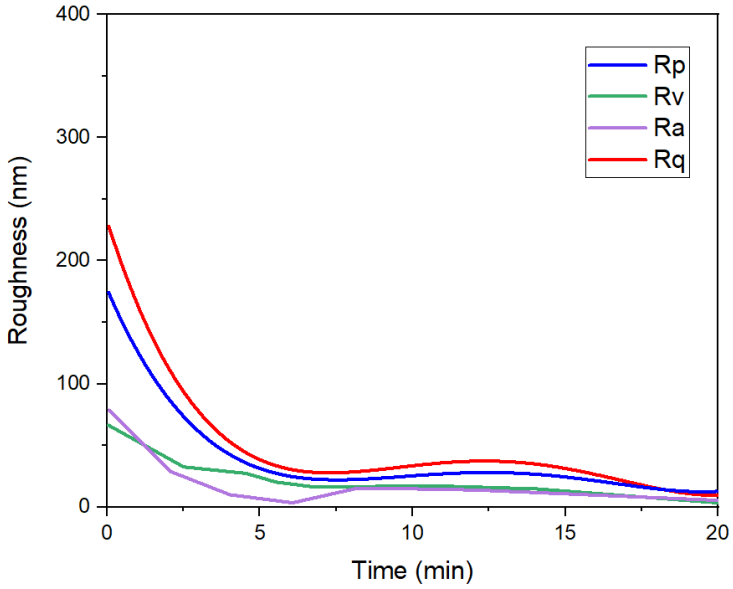

Figure IV.17. Surface roughness evolution curve of Sample 07 showing Ra, Rq, Rp, Rv values over 20 minutes of polishing.

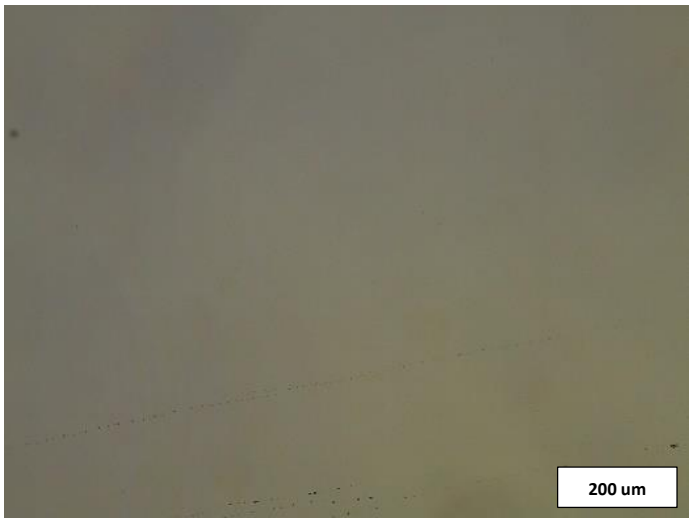

Figure IV.18. Optical micrograph of Sample 07 after polishing.

Microscopy (Figure IV.18) confirms the profilometric trends, showing a smooth, homogeneous surface with minor polishing debris and effective removal of prior machining marks.

The polishing protocol, using a fine 0.25 µm diamond abrasive combined with high load and moderate speed, achieves effective and rapid surface smoothing.

Sample 08 (0.25 µm Diamond, 10 N, 120 RPM):

Initial Phase (0–5 minutes):

The arithmetic average roughness (Ra) decreases from approximately 70 nm to about 18 nm, demonstrating effective removal of initial surface asperities. Peak height (Rp) declines from about 174 nm to 23 nm, while valley depth (Rv) drops from around 69 nm to 20 nm, reflecting significant smoothing of surface peaks and valleys.

Intermediate Phase (5–10 minutes):

Surface roughness parameters show a complex trend. While Ra continues to decrease, Rv and Rp values show slight decrease around 7–9 minutes, going to approximately 13 nm and 20 nm respectively. This indicates some transient surface irregularities, possibly due to polishing pad condition or abrasive behavior.

Final Phase (15–20 minutes):

By the end of polishing, Ra reduces further to approximately 5 nm, and Rv drops to about 5 nm also. The polishing process reaches a steady state, yielding a smooth surface.

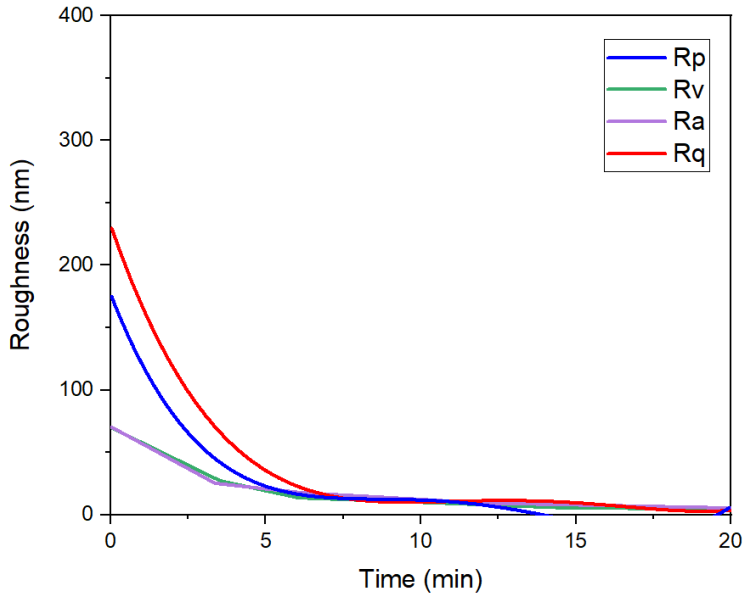

Figure IV.19. Surface roughness evolution curve of Sample 08 showing Ra, Rq, Rp, Rv values over 20 minutes of polishing.

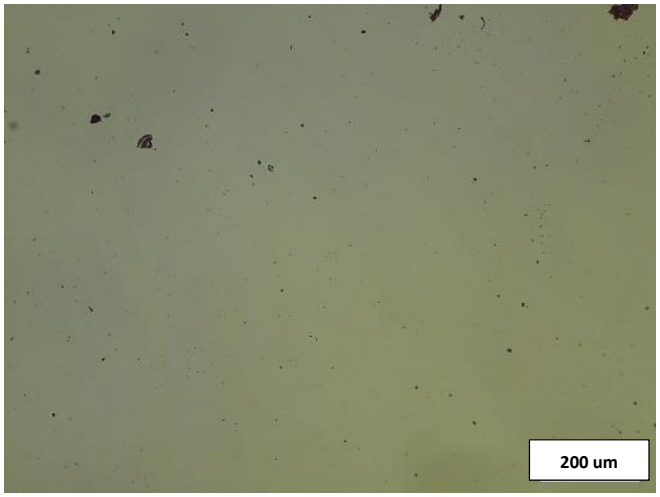

Figure IV.20. Optical micrograph of Sample 08 after polishing.

Microscopy (Figure IV.20) supports the profilometric data, showing a uniform and polished surface with minimal residual defects or debris.

This polishing regime, combining fine diamond abrasive with moderate load and high speed, demonstrates efficient surface smoothing with minor transient roughness variations, achieving an ultra-precision finish appropriate for demanding applications.

Sample 09 (0.25 µm Diamond, 15 N, 50 RPM):

Initial Phase (0–5 minutes):

The arithmetic average roughness (Ra) decreases from approximately 54 nm to about 27 nm in the first 5 minutes, indicating significant smoothing of coarse surface features. Peak height (Rp) drops from roughly 175 nm to 28 nm, and valley depth (Rv) decreases from about 69 nm to 25 nm, reflecting substantial reduction in surface peaks and valleys.

Intermediate Phase (5–10 minutes):

Surface roughness parameters continue to decline steadily, with Ra reaching approximately 16 nm by 10 minutes. Rv and Rp also decrease further to about 14 nm and 18 nm respectively, while Rq follows similar decreasing trend. This phase illustrates ongoing surface leveling and homogenization.

Final Phase (15–20 minutes):

By the end of the polishing cycle, Ra approaches approximately 5 nm, Rv drops to around 8 nm, and Rp decreases to about 7 nm.

Valley depth (Rq) similarly decreases, confirming a smooth, nearly defect-free surface finish.

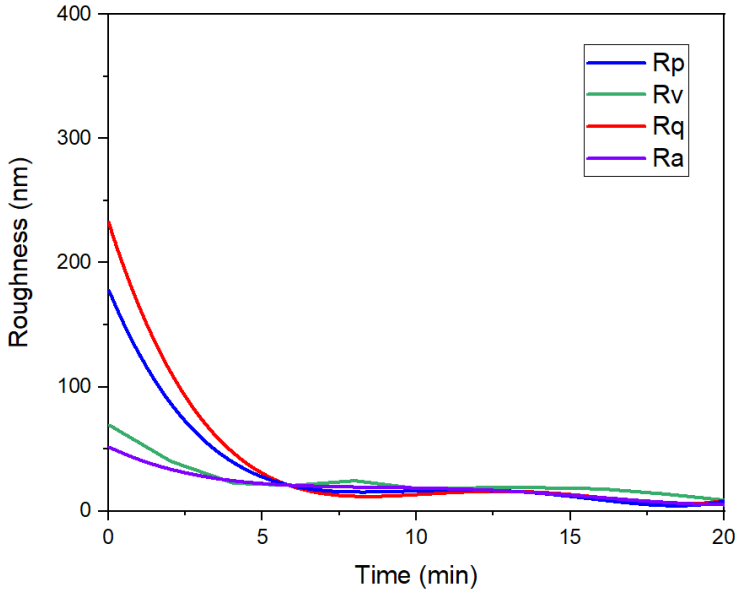

Figure IV.21. Surface roughness evolution curve of Sample 09 showing Ra, Rq, Rp, Rv values over 20 minutes of polishing.

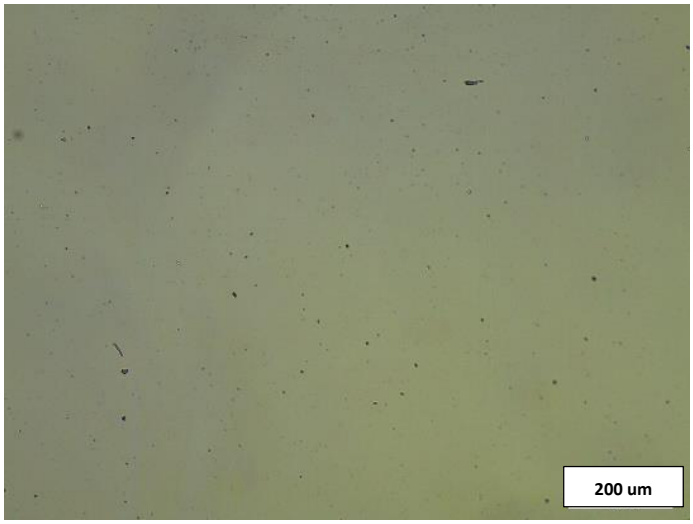

Figure IV.22. Optical micrograph of Sample 09 after polishing.

Microscopy (Figure IV.22) supports these profilometric results, displaying a uniform, smooth surface with minimal residual polishing debris and the effective removal of initial machining marks.

This polishing protocol, using fine 0.25 µm diamond abrasive with moderate load and speed, effectively produces an ultra-precision surface finish suitable for advanced precision applications.

IV.2.4. Main Effects Analysis

To assess the individual influence of polishing parameters on the final surface quality of BGO crystals, a main effects analysis was performed using Taguchi's orthogonal array approach. The average roughness (Ra) values were calculated for each level of grain type, pressure, and rotational speed, revealing the following trends.

Table IV.2. Mean Surface Roughness (Ra) by Polishing Parameter Level.

Factor	Level 1	Level 2	Level 3	Trend
Grain Type	1 μm Alumina (7.51 nm)	0.25 μm Diamond (4.97 nm)	0.3 μm Alumina **(4.53 nm)**	Ra with smaller grain size
Pressure	10 N (6.92 nm)	20 N (5.27 nm)	15 N **(4.81 nm)**	Minimum at moderate pressure
Speed	50 RPM (6.91 nm)	80 RPM (5.81 nm)	120 RPM **(4.27 nm)**	Ra with increasing speed

The average surface roughness values (Ra) were analyzed across all levels of the three investigated polishing parameters. As summarized in Table IV.2, the smallest grain size (0.3 μm Alumina) produced the lowest mean roughness (Ra = 4.53 nm), followed by 0.25 μm Diamond (Ra = 4.97 nm), while 1 μm Alumina resulted in the poorest surface quality (Ra = 7.51 nm).

For applied pressure, the best performance was observed at 15 N (Ra = 4.81 nm), indicating that moderate pressure enables effective material removal without inducing surface damage. At the extremes (10 N or 20 N), the process either lacked mechanical activation or became overly aggressive, leading to rougher results.

Rotational speed was also critical: increasing speed from 50 to 120 RPM consistently reduced Ra, with 120 RPM producing the smoothest surfaces (Ra = 4.27 nm). These findings underscore the synergistic effect of fine abrasives and dynamic mechanical energy input, both of which enhance the ductile-mode removal and suppress mid-frequency surface defects.

A quantitative sensitivity analysis showed that grain size exhibited the largest influence, with a range of 2.98 nm between the 1 μm and 0.3 μm abrasive types. Rotational speed followed closely, with a 2.64 nm effect between 50 and 120 RPM.

Pressure had the least effect, varying Ra by 2.11 nm between 10 N and 15 N. When normalized, the relative sensitivities were 38.5% for grain size, 27.3% for speed, and 34.2% for pressure.

These results confirm that abrasive particle size and mechanical energy input (via speed) play dominant roles in surface quality, while pressure acts as a secondary contributor. Consequently, optimizing grain size and rotational speed should be prioritized when targeting sub-10 nm finishes in BGO polishing.

ΔGrain = Max - Min = 7.51 − 4.53 = 2.98 nm.

ΔPressure = Max - Min = 6.92 − 4.81 = 2.11 nm.

ΔSpeed = Max - Min = 6.91 − 4.27 = 2.64 nm.

Total Variation=ΔGrain +ΔPressure +ΔSpeed =2.98+2.11+2.64= 7.73 nm.

Table IV.3. Main Effects and Sensitivity Contribution of Polishing Parameters on Surface Roughness (Ra).

Parameter	***ΔRa (nm)***	***Sensitivity (%)***
Grain size	2.98	**38.5%** (Most sensitive)
Rotational speed	2.64	**34.2%**
Pressure	2.11	**27.3%** (Least sensitive)

Several samples showed non-monotonic behavior in surface quality, particularly those with high pressure or large grain size. This is likely due to:

Over-polishing: leading to surface damage after initial improvement

Embedded debris or pad wear: reducing consistency over time

These observations emphasize the importance of both parameter selection and process monitoring.

IV.3. Optical Transmittance and Surface Readiness

Following the preliminary surface preparation stages, the optical performance of BGO samples was evaluated to determine their readiness for ultra-precision applications such as TOF-PET imaging. This assessment focused on two key parameters: visible light transmittance and optical absorbance, which directly correlate with surface quality and microstructural integrity. The goal was to quantify how improvements in surface roughness influence the optical efficiency of the scintillating crystal, especially in the wavelength range critical to photodetector sensitivity.

BGO crystals function as scintillators by emitting visible light in response to ionizing radiation, particularly 511 keV gamma photons. The intensity of this emitted light, commonly referred to as light output is crucial, as it determines the number of photons available for detection and thus directly affects the system's timing resolution and sensitivity in TOF-PET imaging. Maximizing transmittance in the blue region (400–500 nm), where BGO's emission spectrum is most active, is essential for efficient photon collection.

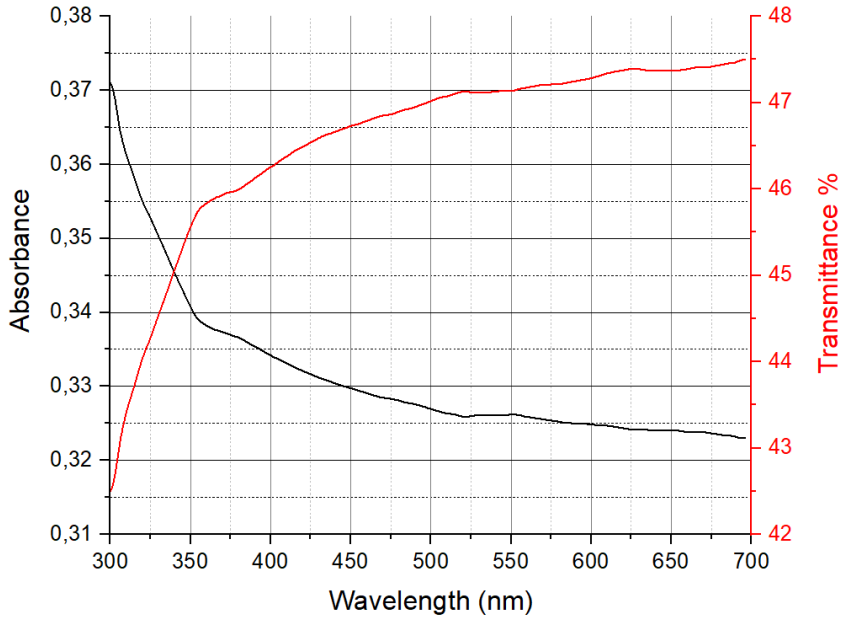

Figure IV.23. Transmittance and absorbance of the rough BGO (Ra ≈ 70 nm).

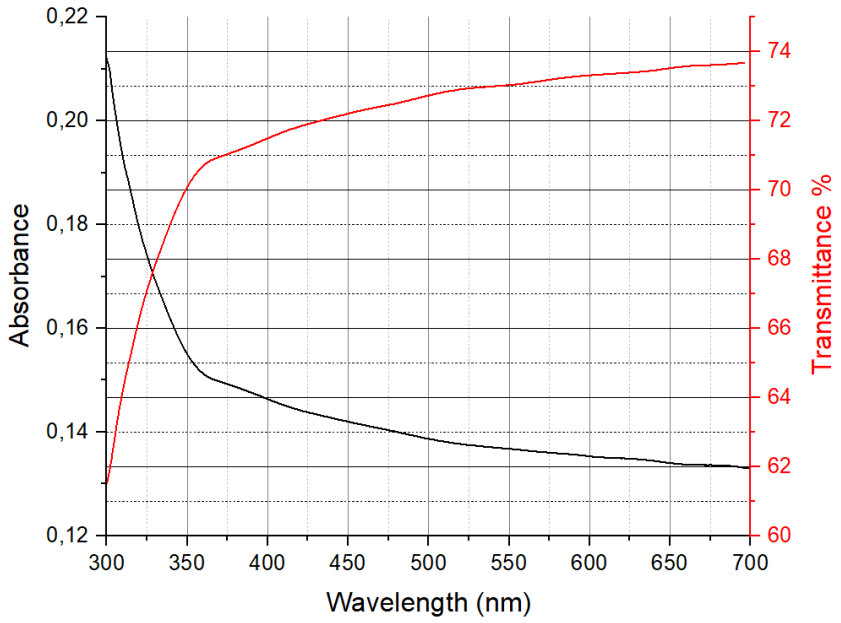

Figure IV.24. Transmittance and absorbance of the polished BGO (Ra ≈ 3.3 nm).

At the reference wavelength of 420 nm that is corresponding to the peak sensitivity of standard photomultiplier tubes (PMTs) used in TOF-PET, the polished sample exhibited a transmittance of 72%, compared to only 46.5% for the rough sample. This 25.5% improvement in transmittance is directly attributed to the reduction in surface roughness, which minimizes photon scattering and enhances optical clarity.

Additionally, absorbance values in the ultraviolet–visible spectrum (300–700 nm) confirm a slight decrease for the polished sample, indicating reduced internal losses. While the difference in absorbance is relatively small (~1% at 420 nm), it further supports the notion that smoother surfaces not only allow greater light transmission but also reduce reflection and scattering losses within the bulk material.

The observed improvement in Ra from ~70 nm (cutting) to 3.3 nm (after optimized polishing) resulted in a marked enhancement in transmittance. This relationship highlights the critical role of surface quality in optimizing light output for scintillating applications. In high-performance optical detection systems such as TOF-PET, where even minor light losses can degrade timing resolution and photon detection efficiency, ensuring sub-10 nm roughness becomes a functional requirement. It is also noteworthy that both transmittance and absorbance curves exhibit consistent behavior beyond the 500 nm wavelength range.

Specifically, the transmittance continues to increase gradually, while absorbance steadily decreases as the wavelength approaches 700 nm. This trend is expected and can be attributed to the intrinsic optical properties of BGO crystals. At longer wavelengths, the photon energy is lower, reducing the likelihood of electronic transitions and light absorption within the crystal structure. As a result, even rough surfaces exhibit improved transmittance in the red and near-infrared regions. Although this spectral range lies outside the primary emission peak of BGO scintillators (typically 400–500 nm), the observation reinforces the conclusion that surface quality has its greatest influence on optical performance in the blue region especially around 420 nm, which is most relevant for TOF-PET detection systems.

IV.4. Conclusion

The experimental results presented in this chapter demonstrate that surface roughness and optical transmittance of BGO crystals can be significantly influenced by fine-tuning the parameters of ultra-precision finishing.

Through systematic variation of abrasive size, cloth material, applied pressure, and rotational speed, we identified critical thresholds beyond which surface quality deteriorates, either through microcrack formation or excessive roughness. The findings also confirmed that smaller grain sizes and moderate polishing speeds yield the most favorable outcomes, while excessive loads degrade surface quality.

Optical transmittance measurements at 420 nm further validated that improvements in surface finish translate directly to enhanced photon collection, crucial for TOF-PET efficiency. These results validate the necessity of parameter optimization in machining brittle crystals and lay the groundwork for advanced simulation and real-time machining strategies, which are explored in the subsequent chapters.

CHAPTER V

ULTRA PRECISION MACHINING OF BGO: EXPERIMENTAL RESULTS AND FINITE ELEMENT SIMULATION

V.1. Introduction

After the initial surface preparation of BGO samples, this chapter focuses on the behavior of this material during ultra-precision machining operations. Following the surface conditioning procedures outlined in the preceding chapter, micro-drilling and micro-milling were conducted to assess the machinability of BGO under controlled conditions utilizing high-precision CNC machinery. The operations signify an important phase in the production of functional scintillator detectors, necessitating a correct choice of tool geometry, feed rate, and cutting depth to prevent surface defects, subsurface damage, and total fracture.

This chapter's initial section outlines the experimental procedures utilized in the ultra-precision machining of the heterostructure. Both proposed designs and results of the effect of parameters, including tool diameter, spindle speed, and feed rate, are examined through SEM and 3D optical microscopy. Observations concentrate on variations in surface roughness across various cutting conditions.

A numerical modeling approach is presented in the second part to augment the experimental findings. Finite element simulations were conducted to replicate static loading and dynamic micromachining scenarios, utilizing the Johnson-Holmquist II (JH-2) model, which had been calibrated through mechanical testing and BGO characterization. This modeling framework facilitates a comprehensive analysis of stress distribution and crack initiation zones.

This chapter presents a combined experimental and numerical analysis that contributes to the formulation of optimized machining parameters for BGO, with the objective of studying its structural integrity and surface quality for optical and scintillator applications.

V.2. Experimental Setup for Ultra Precision Machining of BGO

V.2.1. Heterostrcture Design Configurations

Figure V.1 represents the comprehensive fabrication process of fiber-type heterostructured scintillator pixels through two methodologies: milling (top row) and drilling (bottom row). Using a ball-nosed endmill, the milled approach initially machines semi-cylindrical channels onto flat BGO slices. The milled slices are subsequently arranged in precise alignment to create a three-dimensional structure featuring continuous parallel channels.

The stacked layers are bonded with optical adhesive cured by UV light, and the assembled pixel is subsequently wrapped in PTFE tape to improve reflectivity and mechanical stability. The drilled approach involves the direct drilling of cylindrical holes into a single monolithic BGO block. Machining, the pixel undergoes polishing and is subsequently wrapped in a similar manner.

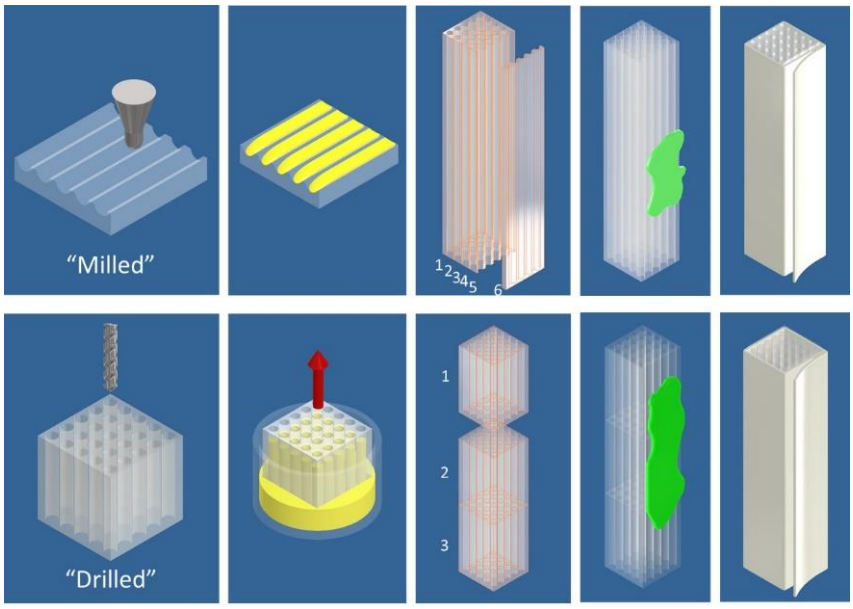

Figure V.1. Illustration of the four stages in assembling a pixel from milled or drilled BGO slices: 1. Functionalization of the machined BGO,2. Stacking of slices ,3. Application and UV curing of adhesive, 4. Wrapping with PTFE tape.

V.2.2. Experimental Results: Micro-Drilling and Micro-Milling of BGO

The influence of feed rate on surface quality was evaluated through a series of micromachining tests on BGO plates using tools of varying diameters. For both micro-drilling and micro-milling as previously represented in Chapter III.

Figure V.2 represents scanning electron microscopy (SEM) micrographs of micro-drilled channels produced using drill diameters of 0.4 mm, 0.25 mm, and 0.15 mm at feed rates of 0.1, 0.2, and 0.3 mm/min. The morphological evaluation focuses on both the lateral (sidewall) integrity and the bottom surface topology of the drilling parameters. The observations reveal the complex interplay between feed rate and tool diameter, influencing the severity and mechanisms of material removal, ranging from ductile mode to brittle fracture.

For the 0.4 mm diameter drill, the channel machined at 0.1 mm/min demonstrates a geometrically regular profile, with continuous sidewalls and minimal edge chipping. The contour remains symmetrical, and the surface finish appears relatively uniform along the vertical section. However, despite this apparent external integrity, the bottom surface exhibits micro fractures and cracks characteristic of brittle failure. At 0.2 mm/min, the degradation becomes more pronounced, as the sidewalls exhibit localized patches and increased surface roughness. Simultaneously, the bottom surface deteriorates significantly, with extensive intergranular cracking and unstable chip detachment zones indicative of a transition toward unstable fracture mechanics. At 0.3 mm/min, the degradation effects still manifested, the hole geometry is irregular as for the previous feed rates, with pronounced edge fragmentation, while the bottom surface is dominated by fracture features, large-scale delamination, and catastrophic subsurface cracking.

In contrast, the 0.25 mm diameter drill at 0.1 mm/min yields moderate-quality sidewalls with mild evidence of ploughing and superficial grain pull-out. The bottom surface, while roughened, does not exhibit severe fracture lines or delamination, remaining within acceptable limits for mechanical integrity. At a feed rate of 0.2 mm/min, however, both lateral and basal regions display significant degradation. The sidewalls become irregular with the emergence of intergranular microcracks, while the bottom surface develops textured zones interspersed with microvoids and debris agglomerates. When the feed rate reaches 0.3 mm/min, the channel geometry becomes highly asymmetric, with severe edge chipping and wall fragmentation. Although the bottom surface shows tearing and loss of coherence, the damage remains comparatively less severe than the brittle cracking observed in the 0.4 mm case. The dominant failure mode here appears more ductile, characterized by material displacement and localized detachment rather than catastrophic damage.

The 0.15 mm diameter drill exhibits a distinct trend, with performance highly sensitive to feed rate variations. At 0.1 mm/min, the SEM images show relatively continuous but slightly rounded sidewalls. The bottom surface, however, reveals significant lamellar delamination and interfacial micro-tearing, consistent with subsurface energy accumulation and premature crack initiation. Interestingly, at 0.2 mm/min, the optimal machining condition for this diameter is achieved. Both the channel walls and the bottom exhibit markedly improved morphological features: sidewall roughness is minimized, edge regularity is preserved, and the bottom surface appears smooth and homogenous, devoid of fracture patterns or chipping.

This condition suggests a balanced energy input sufficient for controlled material removal without inducing fractures. At 0.3 mm/min, the morphological integrity declines, with irregular wall geometry and visible breakout at the hole entrance and exit. Nevertheless, the bottom surface remains less deteriorated than that of the 0.4 mm drill, with damage localized to microcracking rather than complete fracture propagation.

In summary, the SEM analysis confirms that both feed rate and drill diameter critically influence the micro-drilling response of the material, particularly in terms of fracture mechanics and chip formation behavior. While the 0.4 mm drill achieves the best sidewall finish at low feed, it consistently produces the most compromised bottom surfaces due to brittle failure mechanisms, especially at higher feed rates. The 0.15 mm drill, though more susceptible to edge deterioration at extreme conditions, exhibits optimal bottom surface morphology at 0.2 mm/min, reflecting a more favorable energy distribution for ductile-mode machining. The 0.25 mm drill yields intermediate performance but shows progressive degradation in both edge and bottom quality with increasing feed. These results highlight the necessity of optimizing process parameters not only for surface finish but also to mitigate subsurface damage, particularly in brittle substrates where crack propagation can severely compromise component performance.

Figure V.3 presents SEM micrographs of micro-milled channels produced using ball endmills of 0.2 mm, 0.3 mm, and 0.4 mm diameter at feed rates of 10, 25, and 100 mm/min. The images reveal the influence of both tool diameter and feed rate on the surface morphology and structural definition of the machined heterostrcture.

For 0.2 mm diameter endmill at a feed rate of 10 mm/min, the SEM micrographs show relatively better quality channels with continuous edges and clear tool marks along the channel floor. The surface appears uniform, and no major chipping or cracks are observed. However, slight surface variations and minimal waviness suggest localized tool–material interaction instabilities. At 25 mm/min, the surface begins to show signs of degradation. The tool marks become less uniform, and scattered debris appears along the sidewalls. The edges of the channel are less sharp, and the surface quality becomes rougher. At 100 mm/min, significant structural damage is evident. The machined surface exhibits irregular patterns, with pronounced microcracks and surface discontinuities along the tool path. The edges are disrupted, and partial fracture of the edges indicates a transition to a brittle milling regime; cutting action loses stability under increased feed rate.

The 0.3 mm tool, when used at a feed rate of 10 mm/min, produces milled channels that appear well-defined, with fine and continuous tool marks and minimal damage. The SEM images show smooth and parallel striations, and the edges are intact with no breakout or surface tearing. At 25 mm/min, the surface begins to exhibit more pronounced scratches and irregularities. The central area of the milled channel shows chip accumulation and loss of pattern uniformity; though major cracking is still absent. At 100 mm/min, the tool marks become highly inconsistent, and surface defects such as microcracks and localized fragmentation are visible. The channel walls appear eroded, and the floor is marred by disrupted grooves and non-uniform tool engagement, which is indicative of unstable, brittle cutting behavior in this condition.

The SEM images reveal highly regular and smooth surfaces when using a 0.4 mm diameter endmill at a feed rate of 10 mm/min. The tool marks are uniform, tightly spaced, and extend consistently along the channel, with no sign of chipping, debris, or edge wear. The overall geometry is symmetrical and morphologically intact. At 25 mm/min, the channel remains well-formed, although slight tool marks are visible. The edge contours show a subtle loss of sharpness, and the surface texture becomes slightly less refined, although it remains consistent. At 100 mm/min, the machined surface exhibits increased waviness and minor irregularities. The edges show fine micro-tearing, and the tool path uniformity starts to deteriorate. However, compared to smaller tools, the 0.4 mm endmill maintains a relatively stable profile even at higher feed rates, suggesting better resistance to fracture and improved cutting stability under dynamic loading.

The SEM analysis reveals that increasing the feed rate in micro-milling induces a gradual deterioration in both surface integrity and dimensional consistency across all tool diameters. This effect is modulated by tool size, with smaller endmills exhibiting high sensitivity to feed variation. The 0.4 mm tool, when operated at 10 mm/min, yields superior morphological outcomes, characterized by uniform tool trajectories, minimal surface disruption, and sharply defined edges. In contrast, the 0.2 mm endmill demonstrates optimal performance only at low feed rates; beyond this range, particularly at 100 mm/min, the milled grooves show morphological degradation, including irregular surfaces and microcrack propagation. These findings suggest that micro-milling brittle material becomes unstable as mechanical loading increases. Consequently, precise control of feed parameters in conjunction with tool selection is essential to preserving surface quality and ensuring process reliability at the microscale.

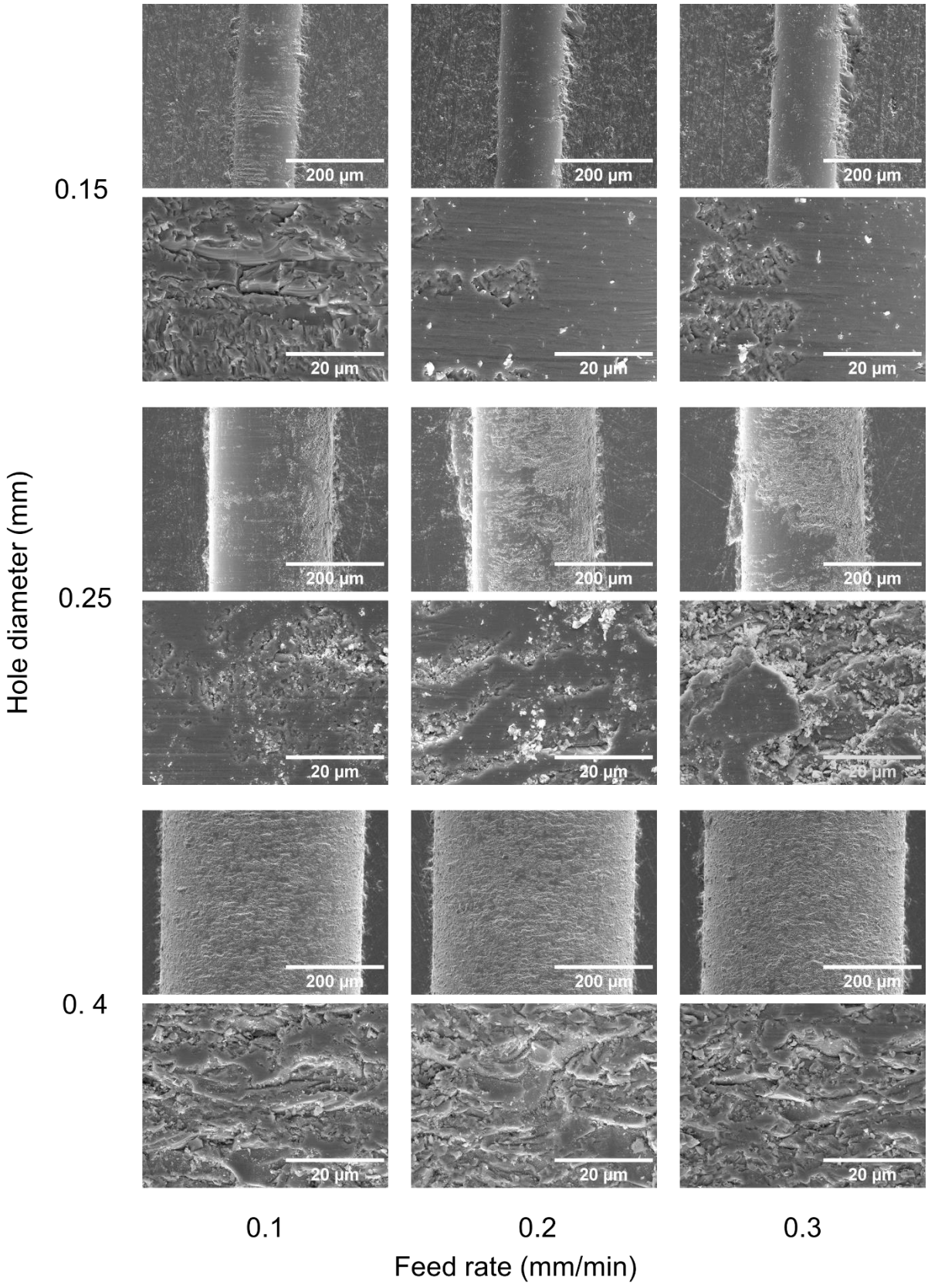

Figure V.2. SEM of the Impact of feed rate on the channel walls of holes drilled into BGO with 0.15, 0.25 and 0.4 mm diameter.

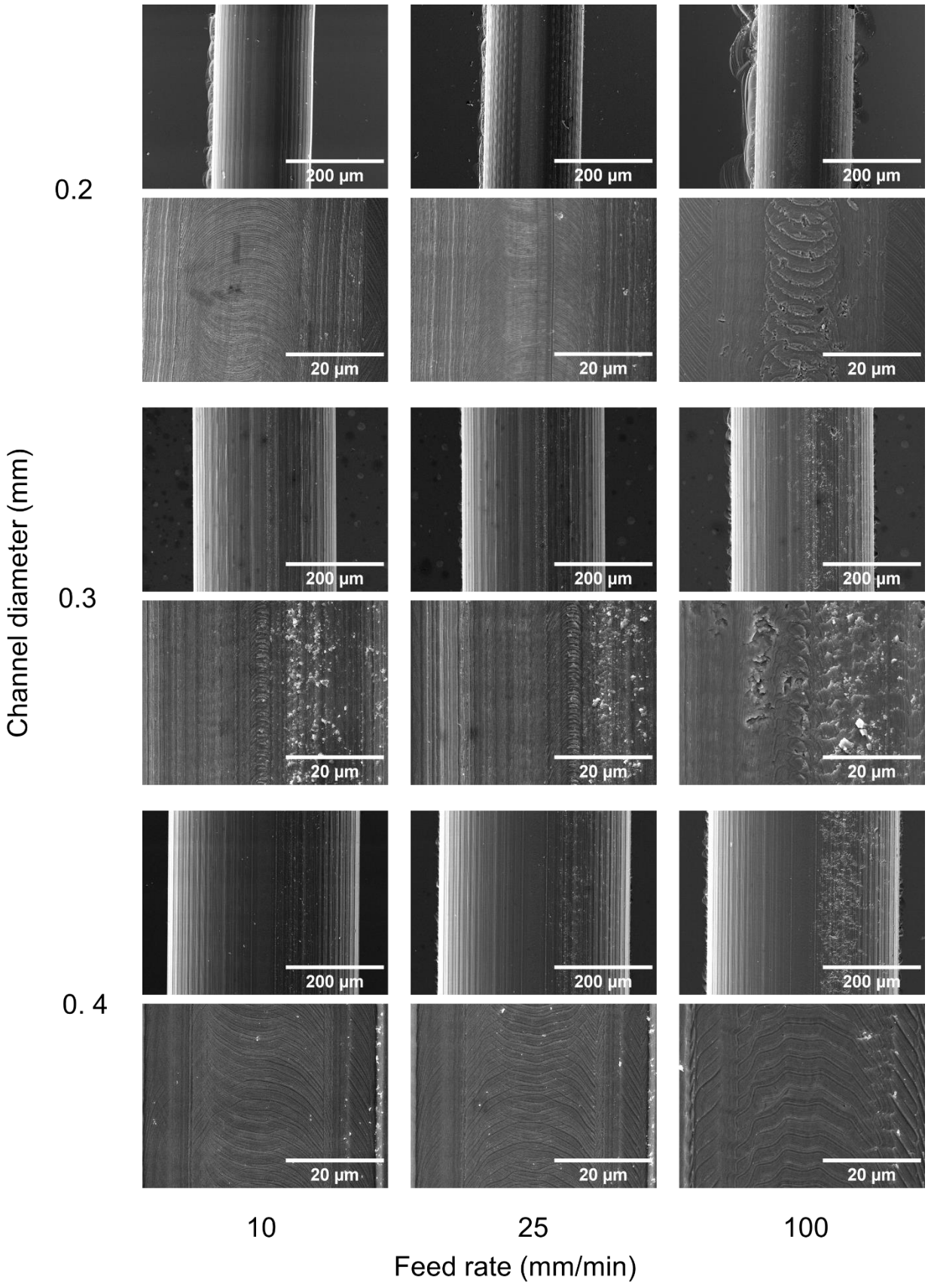

Figure V.3. SEM of the Impact of feed rate on channels milled into BGO with 0.2, 0.3 and 0.4 mm diameter.

Optical 3D microscopy revealed a direct correlation between feed rate and surface integrity as shown in Figure V.4. and Figure V.5.

Figure V.4 presents optical micrographs of micro-drilled hole entries as a function of tool diameter and feed rate. At 0.1 mm/min, all hole geometries exhibit circular contours with minimal peripheral disruption, reflecting stable penetration and controlled chip evacuation. With an increase to 0.2 mm/min, localized damage becomes apparent, particularly in the 0.4 mm and 0.25 mm holes, where irregular edge morphology and onset of radial cracking are observed. At the highest feed rate (0.3 mm/min), entry integrity degrades significantly across all diameters. Notable features include delamination halos, fragmented peripheries, and asymmetric deformation, especially for the 0.25 mm tool, indicating a brittle failure mode and elevated stress concentration during tool engagement. The progressive morphological deterioration confirms a strong correlation between feed rate and the onset of surface damage in brittle substrates during micro-drilling.

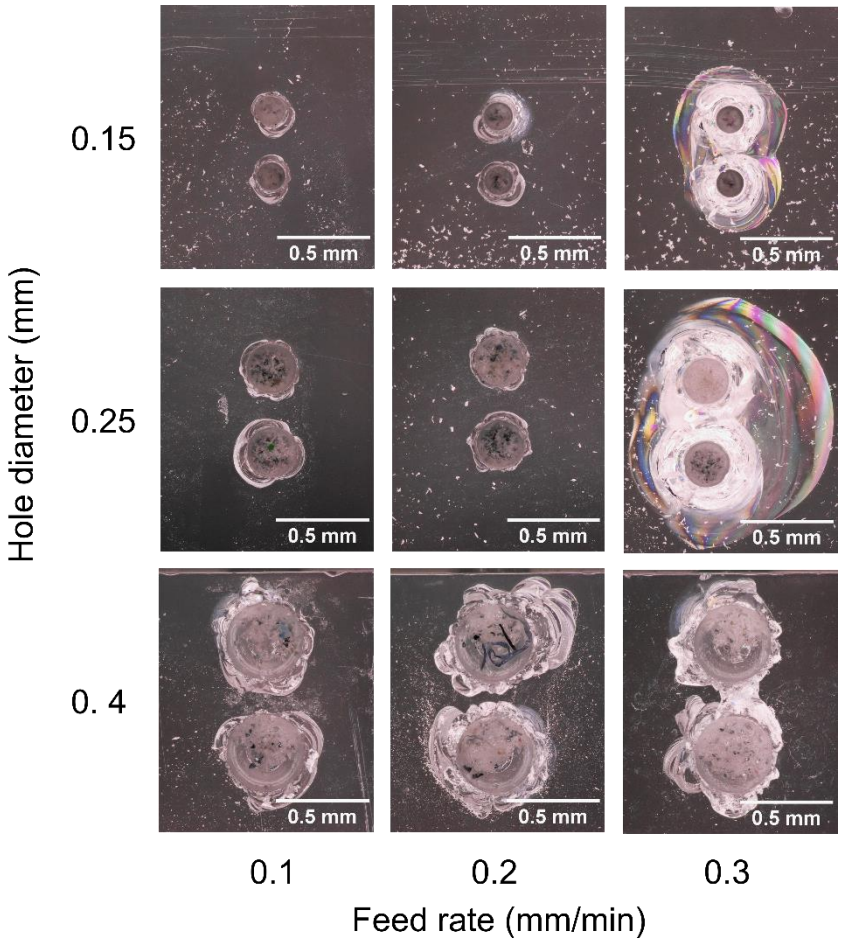

Figure V.4. 3D Microscopic view of the Impact of feed rate on holes drilled into BGO with 0.15, 0.25 and 0.4 mm diameter.

Figure V.5 displays top-view optical images of micro-milled channels. At a feed rate of 10 mm/min, channels exhibit high dimensional fidelity across all tool sizes, with continuous sidewalls, uniform widths, and smooth terminations. This is particularly evident for the 0.4 mm endmill, where edge sharpness and surface coherence are well preserved. At 25 mm/min, minor surface irregularities begin to appear, especially with the 0.2 mm tool, where slight edge waviness and local inconsistencies emerge along the channel length. At the highest feed rate of 100 mm/min, the deterioration becomes more pronounced. Channels milled with the 0.2 mm and 0.3 mm tools display wall discontinuities, edge fragmentation, and path deviation, suggesting unstable tool–material interaction and brittle chip formation. In contrast, the 0.4 mm tool retains acceptable geometric regularity even at this elevated rate, though minor edge roughness is evident. These observations confirm the strong dependence of channel quality on both feed rate and tool rigidity, with smaller diameters exhibiting higher susceptibility to dynamic instability during high-speed micro-milling of brittle substrates.

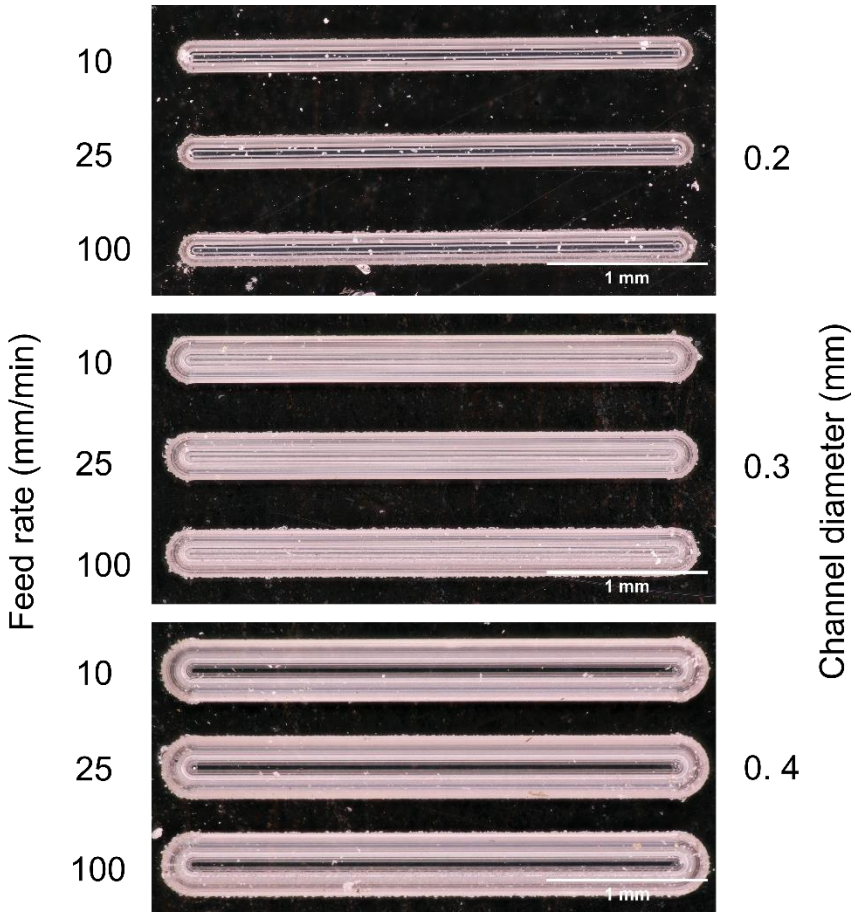

Figure V.5. 3D Microscopic view of the Impact of feed rate on channels milled into BGO with 0.2, 0.3 and 0.4 mm diameter.

Table V.1. Overview of the roughness of channels machined by drilling.

Diameter (µm)	Feed rate (mm/min)	Ra (nm)
0.15	0.1	317
	0.2	109
	0.3	399
0.25	0.1	419
	0.2	359
	0.3	950
0.4	0.1	1010
	0.2	1050
	0.3	508

Table V.2. Overview of the roughness of channels machined by milling.

Diameter (µm)	Feed rate (mm/min)	Ra (nm)
0.2	10	17.0
	25	27.3
	100	60.6
0.3	10	22.4
	25	29.8
	100	107.0
0.4	10	10.7
	25	17.7
	100	41.0

Surface roughness was quantitatively assessed using white-light interferometry, and the results are summarized in Tables V.1 and V.2 for drilled and milled channels, respectively. In micro-drilling, the measured roughness (Ra) ranged from 317 nm to over 1000 nm, with values increasing significantly as a function of both feed rate and tool diameter. Notably, the 0.4 mm drill at 0.2 mm/min produced the highest roughness (1050 nm), indicative of severe subsurface damage and brittle fracture propagation.

In contrast, micro-milled channels exhibited markedly lower roughness values, ranging from 10.7 nm to 60.6 nm, depending on the cutting parameters. The smoothest surfaces were obtained with the 0.4 mm tool at 10 mm/min, whereas the highest roughness occurred with the 0.2 mm tool at 100 mm/min.

These results underscore the superior surface finish achievable through milling, attributable to more stable cutting kinematics and reduced crack formation at the tool–workpiece interface. Overall, the data confirm that micro-milling is significantly more effective than drilling in producing optically smooth surfaces in brittle substrates such as BGO.

V.2.3. Optical Evaluation of Machined BGO

Normalized emission spectra shown in Figure V.6 revealed that milled samples closely matched the reference spectrum of unmachined BGO, with peaks centered near 480–490 nm. No significant wavelength shifts or peaks broadening are seen for either of the machined samples suggesting that the machining techniques do not induce new colour centres in the material.

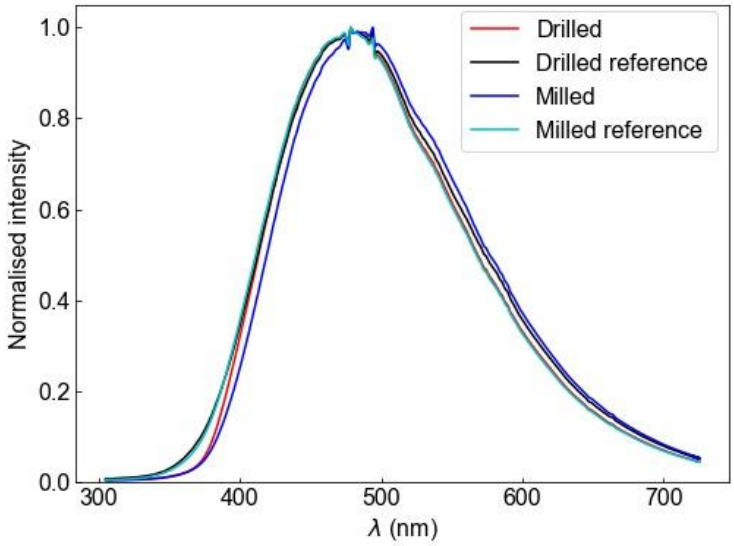

Figure V.6. X-ray excited radioluminescence spectra of drilled and milled pixel.

Timing measurements in Figure V.7 showed that milled BGO retained a CTR profile nearly identical to the reference. In contrast, drilled samples exhibited broader, asymmetric timing distributions, confirming that surface damage and roughness degrade temporal resolution. The broader CTR in drilled samples suggests that optical inhomogeneity causes variations in photon path length, increasing timing jitter.

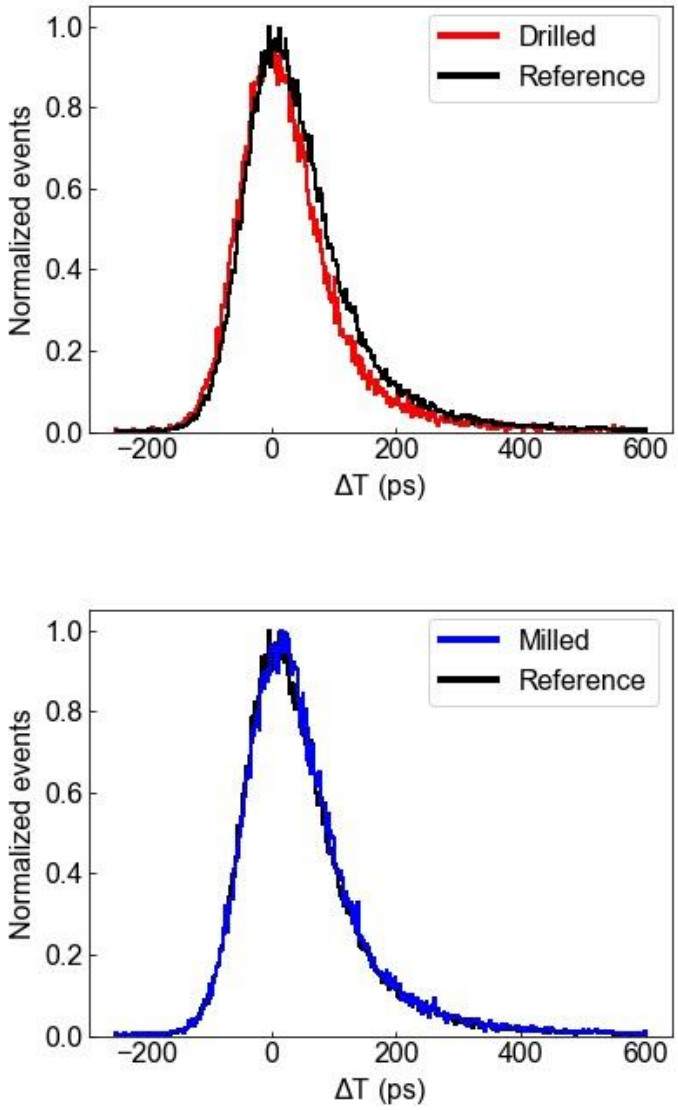

Figure V.7. Coincidence timing resolution measurements of samples prepared by drilling and assembled milled.

Figure V.8 presents the pulse height spectra of BGO pixels fabricated using two different machining methods, drilling (red line) and milling with assembly (blue line) compared to their respective unmachined reference sample. The reference samples exhibit the highest photopeak intensities, indicating optimal light output. The drilled pixel shows a slight reduction in photopeak amplitude and broadening, likely due to surface damage and increased light scattering from brittle fractures introduced during drilling. In contrast, the milled and assembled pixel displays a more pronounced shift toward lower charge values and reduced peak intensity, suggesting greater light loss.

This is attributed not to the milling process itself, but rather to the absence of a scintillating filler and potential light losses at the interfaces between assembled slices. Thus, while Figure V.8. shows lower light output for the milled pixel, it does not imply inferior machining quality; instead, it reflects the incomplete optical structure of the milled sample during testing.

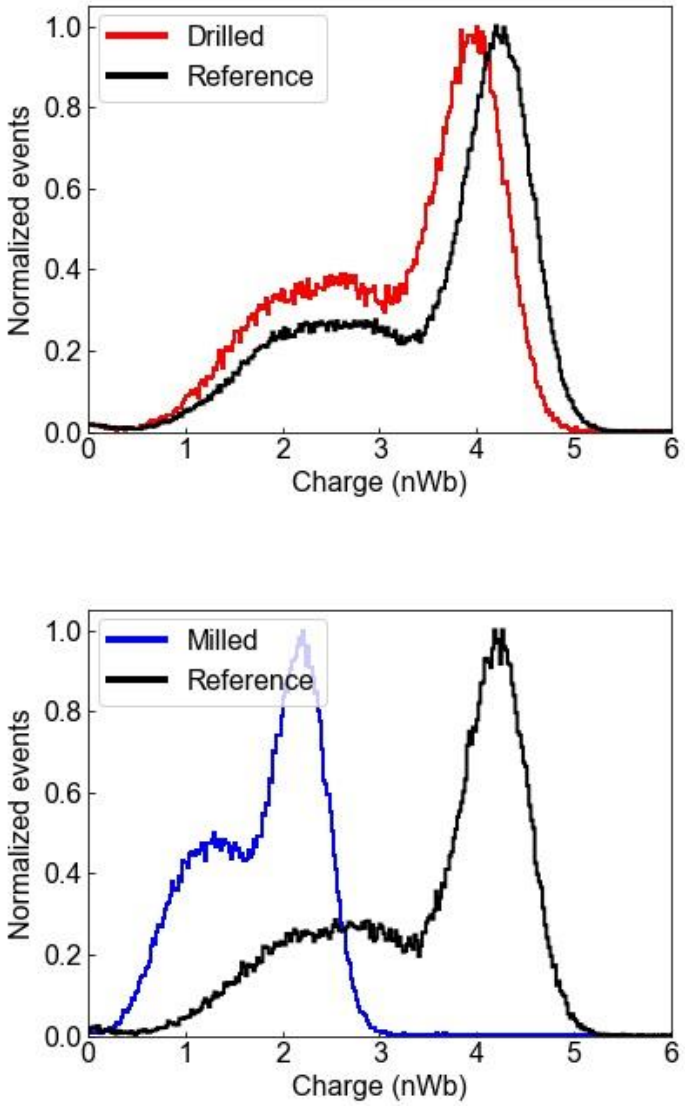

Figure V.8. Pulse height spectra of samples prepared by drilling and assembled milled.

V.3. Numerical Simulation of Micromachining Behavior Using the JH-2 Model

To complement the experimental study and deepen the understanding of material behavior during ultra-precision machining, a numerical simulation approach was employed using the Johnson-Holmquist II (JH-2) constitutive model [97]. This model is specifically designed to describe the behavior of brittle materials such as Bismuth Germanate (BGO) under varying strain rates and stress conditions.

The aim of the simulation was to predict stress distribution, damage growth, and fracture behavior under conditions for both quasi-static mechanical testing and dynamic micromachining processes. The simulation was executed in Abaqus/Explicit, utilizing material characteristics obtained from experimental mechanical characterization and literature-derived estimations. This dual methodology enabled precise reproduction of fracture initiation, propagation, and the brittle-to-ductile transition during material removal. This section explains how to evaluate material properties, adjust the JH-2 model, and test it with quasi-static compression and split tensile tests and the application of the model to simulate micro-milling, comparing force production, stress localization, and machining induced damage.

V.3.1. Quasi-static Compression

Figure V.9 illustrates the average stress–strain curve derived from the five experiments labeled C1–C5. The graph indicates that during quasi-static uniaxial compression loading, BGO has a nearly linear stress-strain relationship until it attains its maximal compressive strength, highlighting its pronounced brittleness. Table V.3 presents the outcomes of the compressive strength tests.

Table V.3. Quasi-static uniaxial compression testing results.

No.	Compressive strength (MPa)	Young's Module (GPa)	Average (GPa)	Standard Deviation (GPa)
C1	612.71	104.59	102.60	1.6349
C2	605.63	101.18		
C3	630.53	104.18		
C4	578.95	102.69		
C5	668.23	100.39		

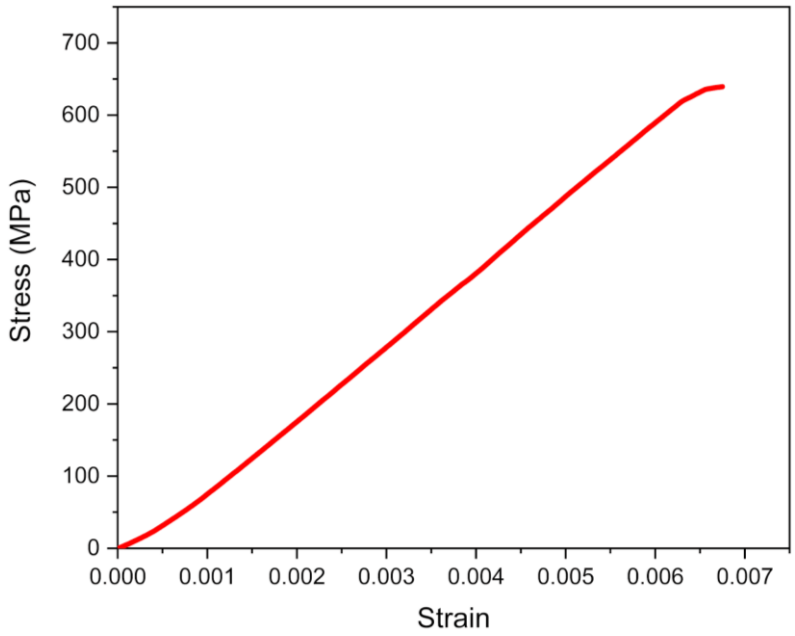

Figure V.9. Mean quasi static uniaxial compression testing stress–strain curve.

The average Young's modulus is 102.6 Gpa, with a standard deviation of 1.6349 GPa. This is comparable to the 105.4 GPa reported by Majorana et al. [95]. C1 and C3 fluctuate within one Young's modulus value (104 GPa). These are normal fluctuations. The mean compressive strength of BGO is 619.2 MPa, with a standard deviation of 21.3672 MPa. The higher fluctuation among these five sets may be due to internal defects, microcracks, and localized porosity, which can lead to variations in compressive strength. Additionally, the distribution and severity of inherent defects within each sample can cause significant deviations in the measured failure forces. Samples that fail around 650 MPa likely represent those with minimal defects and optimal microstructural integrity. In contrast, those failing around 590 MPa may contain significant stress concentrators, which drastically reduce their load-bearing capacity. These results underscore the importance of considering microstructural and defect analysis when interpreting the compressive strength of brittle materials. If a specimen already contains many defects, its strength decreases rapidly, leading to material failure.

Split test

The ultimate tensile strength of the BGO was indirectly estimated by determining the peak pressure at which the material failed. The tensile stress can be calculated as follows:

$\sigma_t = 2p/\pi dl$ (4)

In the given formula, σ_t represents the maximum tensile stress in the specimen's center, in MPa; p signifies the load at failure, in N; d and l are the specimen's diameter and length, respectively, in mm. The tensile strength results, shown in Table Table V.4, indicate that BGO had an average ultimate tensile strength of 20.82 MPa, with a standard deviation of 1.35 MPa. The mean split testing force displacement curve is presented in Figure V.10.

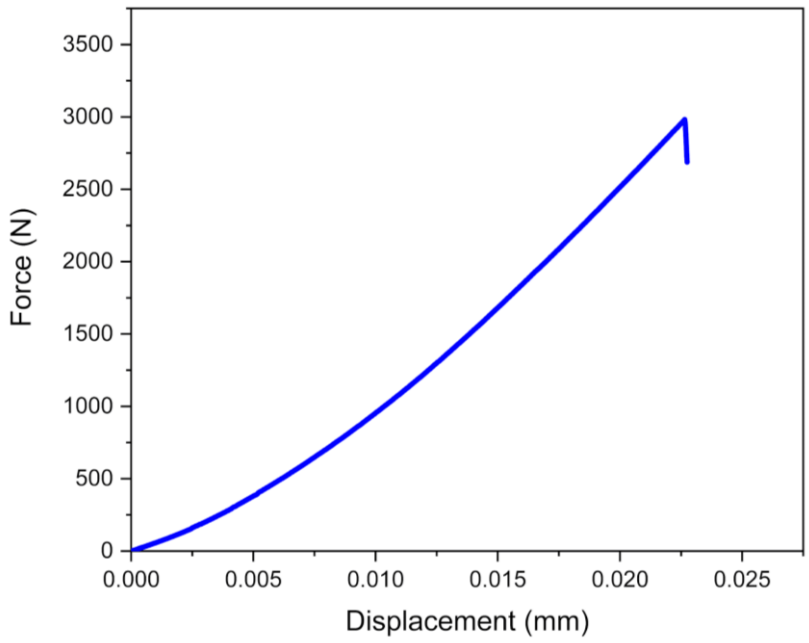

Figure V.10. Mean split testing force-displacement curve.

Table V.4. Split test tensile strength results.

No.	Failure Force (N)	Specimen Diameter (mm)	Specimen Length (mm)	Tensile Strength (MPa)	Average (MPa)	Standard Deviation (MPa)
S1	3450.7	10	10	21.97	20.82	1.35
S2	2970.8	10	10	18.92		
S3	3388.8	10	10	21.58		

V.3.2. JH2 model parameters determination

The JH-2 model is employed in this study to characterize the mechanical response of BGO. It accounts for both intact and fractured material states, incorporating strain rate dependency, damage evolution, and pressure-dependent strength. This section details the specific methodology used to determine the parameters governing the model, which are derived from experimental quasi-static uniaxial compression and split tests. The proposed model is divided into three groups of parameters describing the behavior of the brittle material.

From the results of the experiments above, the average Young's modulus of the material was E= 102.60 GPa. The Poisson ratio was taken from literature to be $\nu = 0.175$ [95].

The bulk modulus was $K_1 = E/(3(1-2\nu)) = 52.61$ GPa. (5)

and the shear modulus was $G = E/(2(1+\nu)) = 43.65$ GPa. (6)

Parameters of the equation of state

The equation of state characterizes the relationship between hydrostatic pressure and volumetric strain in a material. At low pressures, the hydrostatic pressure tensor is relatively minor, allowing for a straightforward linear expression of the equation of state. In the JH-2 model, the equation of state of the material can be expressed by the following equation:

$$P=K_1 \mu + K_2 \mu^2 + K_3 \mu^3 \quad (7)$$

Where: K_1 is the bulk modulus of the material previously calculated. K_2, K_3 are material constants, P is the hydrostatic pressure, μ is the volumetric strain, ($\mu = \rho/\rho_0 - 1$), $\rho 0$ is the material's initial density and ρ is the current density.

A plate impact test is used to obtain the P-μ curve of the brittle material under high pressure. As no plate impact test was found in the literature for BGO, based on other similar material properties [98,99], in this case it was taken that $K_2 = K_3 = 0$ GPa.

Parameters of the strength model

The JH2 strength model accounts for both the intact strength and the material strength at fracture. To represent the transition from the intact state to the fractured state, a damage scalar is introduced. The normalized equivalent stress σ^* is given as:

$$\sigma^* = \sigma^*_i - D(\sigma^*_i - \sigma^*_f) \quad (8)$$

The behavior of the material is modeled based on its damage state. When no damage is present, the scale damage parameter D is (D =0), the equivalent dimensionless stress is given by the following equation:

$$\sigma^*_i = A(P^* + T^*)^N [1 + C \ln(\dot{\varepsilon} + \dot{\varepsilon}_0)] \quad (9)$$

For a complete material failure, the scale damage parameter is (D =1), the dimensionless equivalent stress can be represented by:

$$\sigma^*_f = B(P^*)^M [1 + C \ln(\dot{\varepsilon} + \dot{\varepsilon}^0)] \quad (10)$$

In these equations, the material dimensionless constants are A, B, C, M and N. The dimensionless hydrostatic pressure is represented by P^*, where: $P^* = P/P_{HEL}$, while the maximum hydrostatic tensile stress and the equivalent stress are normalized by the general form: $T^* = T/P_{HEL}$, $\sigma^* = \sigma/\sigma_{HEL}$, respectively. The parameter P_{HEL} refers to the pressure of the brittle material at the equivalent stress (σ_{HEL}) at Hugoniot elastic limit (HEL). T refers to the maximum tensile pressure of the brittle material before failure. The dimensionless strain rate is the real strain rate $\dot{\varepsilon}$ and $\dot{\varepsilon}_0$ is the reference strain rate.

The Hugoniot elastic limit, HEL in the JH-2 model, is calculated using the plate impact test. In this paper, we will take as a reference two single crystal hard brittle materials, single-crystal quartz and sapphire, which are similar to BGO [100].

For safety when machining bismuth germanate (BGO), it is better to take the HEL value of quartz rather than sapphire. Specifically, using the lower HEL range of quartz (5.5-8.5 GPa) would be the most conservative and safest approach, given BGO's material properties and the need to prevent failure during machining. Through a sensitivity analysis compared to different single crystal materials as shown in Table V.5 and Table V.6, the chosen Hugoniot elastic limit will therefore be HEL = 5.8 GPa in this paper. The HEL value can be described by the following formula:

$$HEL = K_1 \mu_{HEL} + K_2 \mu_{HEL} + K_3 \mu_{HEL} + 4/3\ G\ \mu_{HEL} / (1 + \mu_{HEL}) \qquad (11)$$

Where μ_{HEL} is the volumetric strain at Hugoniot Limit.

Table V.5. HEL values for different single crystal materials.

Material	**HEL (GPa)**
Quartz	5.5 - 8.5
Sapphire	5.5 - 11
Almandine Garnet	8.1 ± 1.7
Alumina	7.5 - 9
Silicate Glass	4 - 10
Crown Glass (K9)	~6.8

Through a sensitivity analysis (see Table below), we found that the best HEL range for BGO is 5.5–6 GPa, with 5.8 GPa chosen as the reference because it provided the most stable compressive strength (657 MPa).

Furthermore, experimental split tests validated this estimation, as the measured failure stress closely aligned with predictions based on a 5.8 GPa HEL. This agreement confirms that our chosen HEL value effectively captures BGO's brittle fracture behavior.

Table V.6. Sensitivity analysis of the compressive strength value for different HEL values.

Tested HEL (GPa)	Compressive Strength (MPa)
4	506
5.5	632
6	659
6.5	778
8.5	810
11	860
15	1012

By replacing the estimated HEL value, and the values obtained from equations (5) and (6) in (11): μ_{HEL}= 0.054, then we can obtain the value of P_{HEL} from equation (7): P_{HEL}= 2.84 GPa.

The tensile strength is derived from the ultimate tensile strength obtained from split from equation (4) by the formula:

$$T= \sigma_t/3 \ ((1+\nu)/(1-\nu)) = 9.88 \text{ MPa.} \quad (12)$$

Finally, the value of σ HEL is given by the following equation:

$$\sigma_{HEL} = 3/2 \ (HEL - P_{HEL}) = 4.44 \text{ GPa.} \quad (13)$$

For the remaining parameters A, B, M, N and C, the values were determined based on the range typically observed for brittle materials and further refined through simulations. [98,99]

Parameters for the damage model

The JH-2 model employs a damage formulation similar to the Johnson-Cook model [101]. The damage parameter, D, is defined using the following equation.

$$D= \sum (\Delta\varepsilon_p/\varepsilon_p^f) \quad (14)$$

$\Delta\varepsilon_p$ refers to the integral of the effective plastic strain, ε_p^f represents the equivalent plastic strain of the material at fracture under a given pressure.

$$\varepsilon_p^f = D_1 (P^*+T^*)/D_2 \quad (15)$$

In the JH-2 damage model, the parameters D_1 and D_2 are two dimensionless damage parameters used to describe material damage.

Since BGO fractures under very small strains, it is challenging to determine D_1 and D_2 experimentally. These parameters can be estimated through numerical simulations to achieve realistic damage predictions. Based on experimental data comparative view of the failure mechanisms [102], numerical simulations from prior studies [98,99], and iterative comparisons with our real compression test results, the values of $D_1 = 0.045$ and $D_2 = 0.85$ were selected as the initial damage parameters in this paper.

V.3.3. Application of the model

In our study, we implemented the Johnson-Holmquist 2 (JH-2) model in Abaqus by using the User-defined mechanical material behavior feature, which allowed us to incorporate the JH-2 constitutive model into the Abaqus library. The model includes 32 mechanical constants and 8 solution-dependent state variables such as equivalent plastic strain (PEEQ), ductile damage initiation criterion (DUCTCRT), pressure increment due to bulking (DELTAP), and damage (D). We used the VUMAT subroutine in Abaqus/Explicit, which requires a constitutive model to be defined within the user's subroutine.

Quasi Static uniaxial compression test simulation

The dimensions of the specimen in the simulation are the same as that used in the Quasi-static uniaxial compression test and split experiments (10 mm × 10 mm) as shown in Figure V.11. The material was considered homogeneous. Due to the larger cross-sectional area of the plates in the tests compared to the specimen, a uniform compressive load was assumed to act on the BGO surface in JH2 modeling. During the compressive test, a constant velocity was applied to the top face along the Y compression direction, allowing it to compress while deforming freely. The boundary conditions were adjusted so that the bottom face remained fixed. General contact with a defined coefficient of friction ($\mu = 0.3$) was applied based on iterative testing for specimen stability. The mesh type size was chosen to be C3D8R with a size of 0.2 mm in this study based on a mesh convergence as shown in Figure V.12. The plates were set as rigid, and the constitutive material model for the BGO specimen was defined based on the JH-2 damage model with the parameters listed in Table V.7.

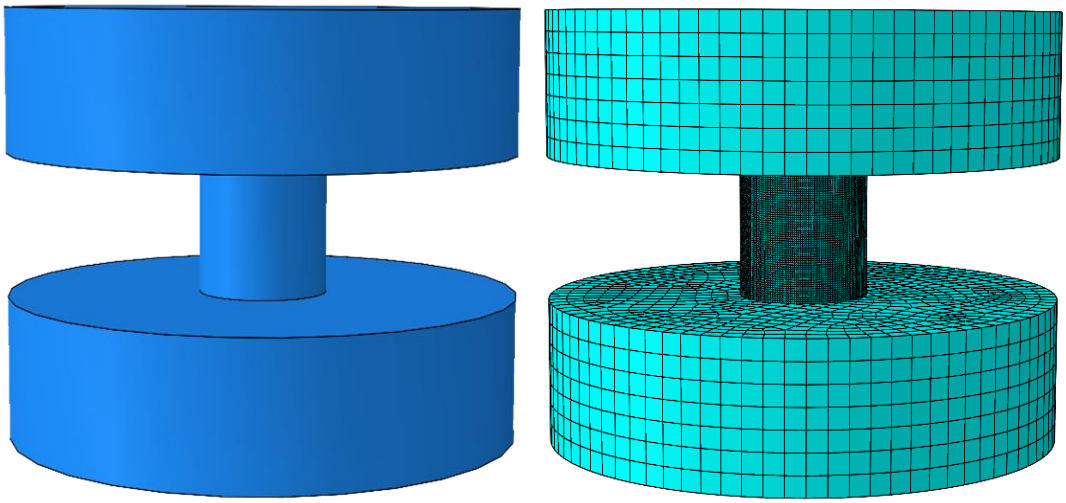

Figure V.11. The geometric structure and boundary condition of the three-dimensional (3D) finite element model (FEM) of quasi static compression test.

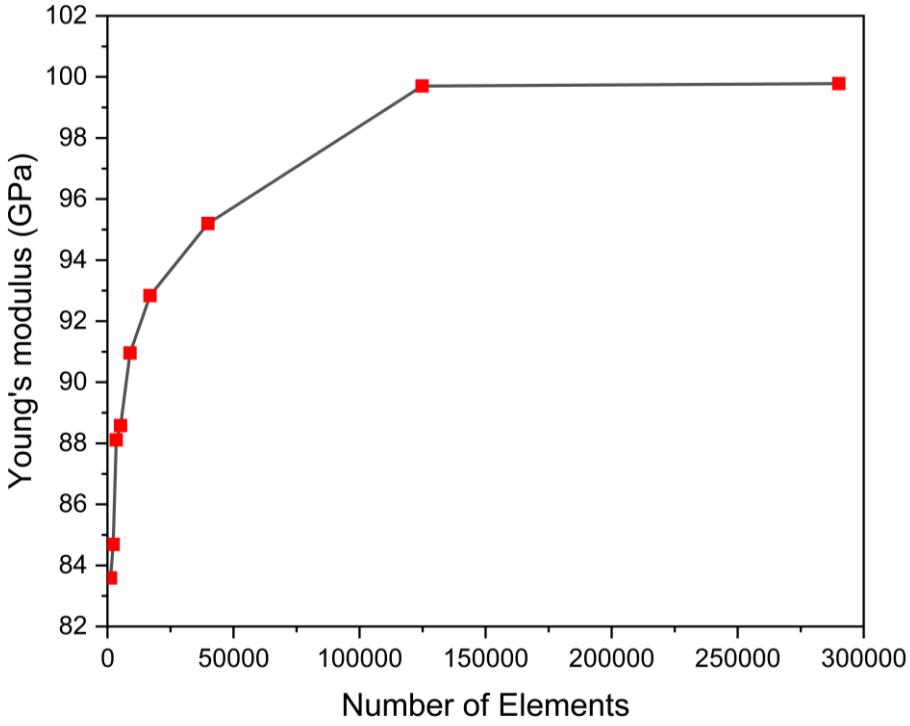

Figure V.12. Mesh convergence.

Table V.7. Abaqus JH-II model material parameters of the BGO.

Density (g cm-3)	7.13 [95]
Strength Constants	
A	0.97
B	0.31
C	0
M	0.6
N	0.52
Tensile strength (MPa)	9.88
Pressure at HEL (GPa)	2.84
HEL strength (GPa)	4.44
Shear modulus (GPa)	43.65
Damage constants	
D_1	0.045
D_2	0.85
Equation Of State	
K_1 *(GPa)*	52.61
K_2	0
K_3	0
Bulk	1
FS	0.2

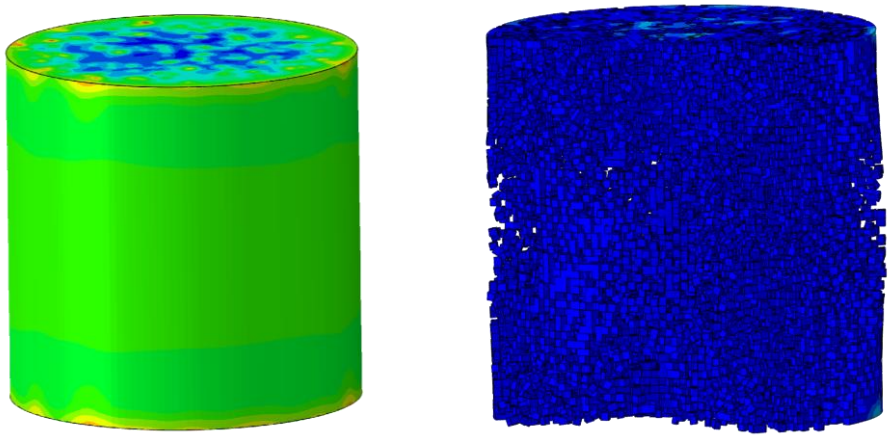

(a) Deformation mode before failure. (b) Crack propagation and failure of material.

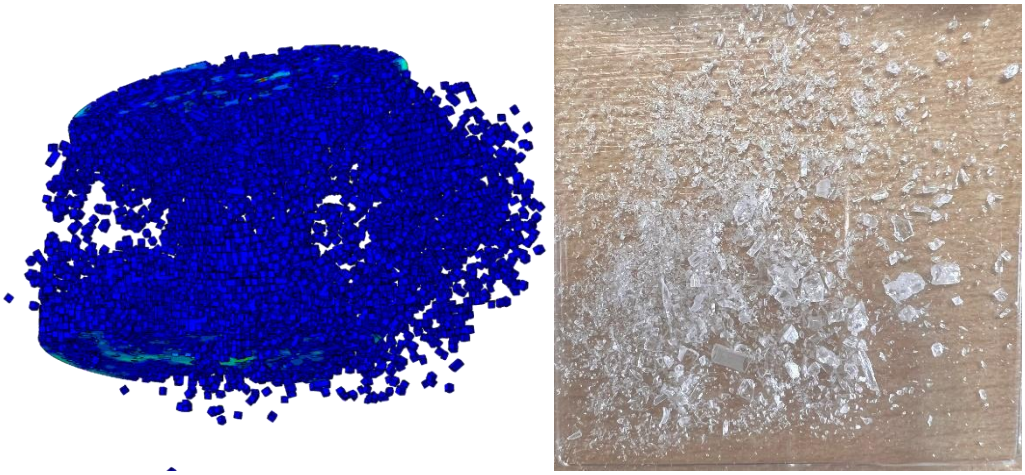

(c) Final damaged specimen. (d) Real final damaged specimen.

Figure V.13. Damage propagation until failure in simulation and experimental for uniaxial quasi-static compression test.

In the presented quasi-static compression test, the simulation results from Abaqus, shown in Figures V.13 (a to c), demonstrate a close correlation with the experimental results of the real damaged specimen (Figure V.13.d). The simulation initially captures the deformation mode before failure (Figure V.13.a), where the material exhibits a gradual build-up of internal stresses. As loading progresses, the material undergoes crack initiation and propagation (Figure V.13.b), leading to its eventual failure, depicted in Figure V.13.c.

The final state of the simulated specimen (Figure V.13.c) reveals a disintegration pattern characterized by dispersed material fragments, which closely mimics the observed behavior in the real damaged specimen (Figure V.13.d). Both the simulation and the experimental results show a similar fragmentation pattern, indicating that the implemented material model in Abaqus provides an accurate representation of the physical behavior of the material under uniaxial quasi-static compression.

The stress-strain curves presented in Figure V.14 illustrate a comparative analysis between the experimental results from five different samples (C1, C2, C3, C4, and C5) and the simulation data. The graph reveals a remarkable consistency between the experimental data points and the numerical simulation. Each experimental curve demonstrates a similar trend of linear elastic behavior, followed by a slight nonlinearity as the strain increases. This behavior aligns closely with the simulated curve, which follows the same trajectory as the experimental data, particularly in the elastic regime up to strains of approximately 0.0067.

Notably, the dispersion observed between the experimental curves is minimal, with all curves clustering closely around the simulation curve. This suggests a high degree of repeatability and reliability in both the experimental procedure and the simulation model. The simulation slightly underestimates the stress values in the lower strain regions that can be attributed to inherent imperfections, such as microstructural defects (porosity and microcracks), but captures the overall stiffness and the material's response to increased loading with high precision.

The correlation between the experimental and simulated results provides strong evidence that the simulation model is valid for predicting material behavior under similar quasi-static conditions. This accurate alignment between experimental and simulated stress-strain curves is critical for validating the mechanical model used in the finite element analysis.

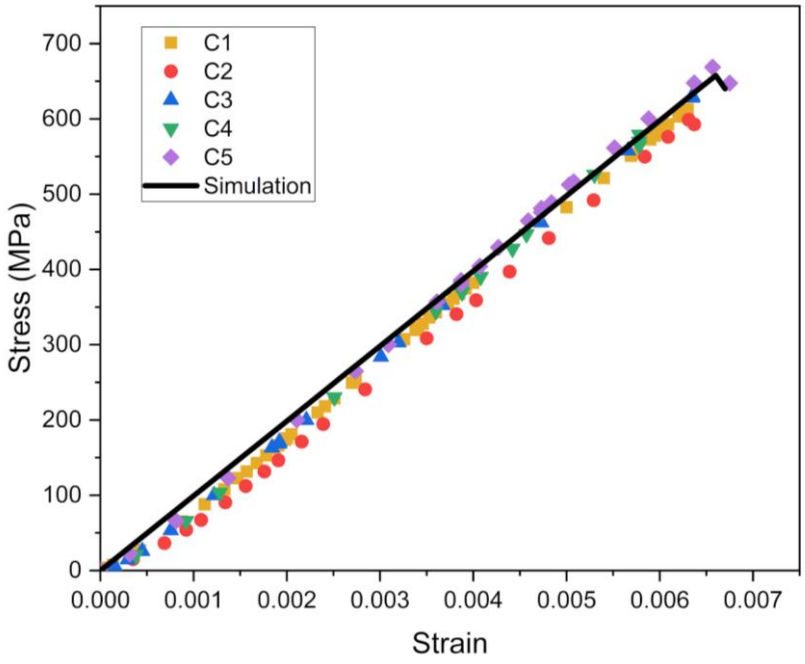

Figure V.14. Simulation and experimental stress-strain curve of quasi static compression tests.

Split test Simulation

To accurately model the fracture behavior of BGO, a finite element simulation of the split test was also conducted in Abaqus. The boundary conditions and loading conditions were replicated from the experimental setup to ensure consistency in stress distribution and failure prediction.

Figure V.15 illustrates the 3D finite element model (FEM) used for the split test simulation, where the lower plate was constrained while a compressive force was applied at the top plate to induce tensile stresses.

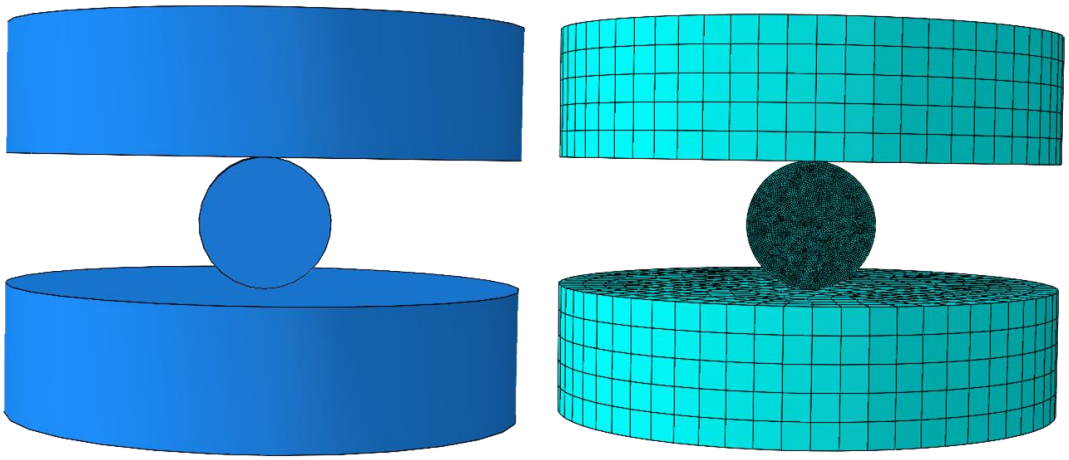

Figure V.15. The geometric structure and boundary condition of the three-dimensional (3D) finite element model (FEM) of split test.

In the simulation results depicted in Figure V.16.a, the material undergoes a deformation before failure. The stress distribution is concentrated along the axis of loading, with stress propagating symmetrically. This behavior is consistent with brittle materials, which tend to accumulate stress at localized points before sudden failure. The large stress concentration at the loading point indicates that the material experiences tensile stresses, leading to eventual failure. The symmetric stress propagation suggests that the loading conditions are uniform, confirming the accuracy of the simulation setup. The first visible crack in Figure 10.b appears at the point of highest stress concentration. The model accurately predicts the onset of failure, capturing the initial fracture at the location where the material's strength is exceeded. This early-stage crack generation is critical in brittle materials, where cracks form and propagate rapidly once the material's tensile strength is reached. The initiation of this crack aligns with the experimental results in Figure V.16.e, where the crack begins at the same location, further validating the simulation model. As shown in Figure V.16.c, the simulation successfully captures the propagation of the crack throughout the material. The crack follows a predictable path, growing along the plane of maximum stress. This behavior is typical in brittle materials where failure occurs through crack extension rather than plastic deformation. The accurate depiction of crack propagation highlights the model's ability to simulate brittle fracture mechanics.

In comparison to Figure V.16.e, the real-world material exhibits a similar crack path, confirming that the model closely mirrors the physical behavior of the material under load. The final damaged specimen in the simulation, shown in Figure V.16.d, demonstrates the complete fracture of the material. The material splits into two distinct sections, with visible fragmentation occurring along the crack path. This fragmentation pattern is consistent with the brittle failure mode, where the material does not undergo a big plastic deformation but instead fractures immediately. In the experimental results (Figure V.16.f), the material also fractures into similar fragments, further validating the accuracy of the Abaqus model.

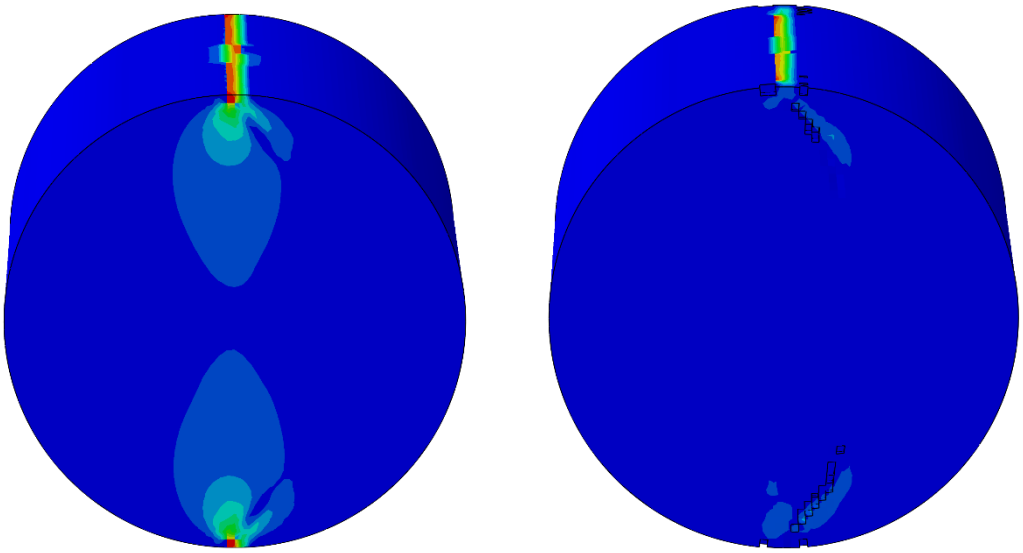

(a) Deformation mode before failure. (b) First crack generation.

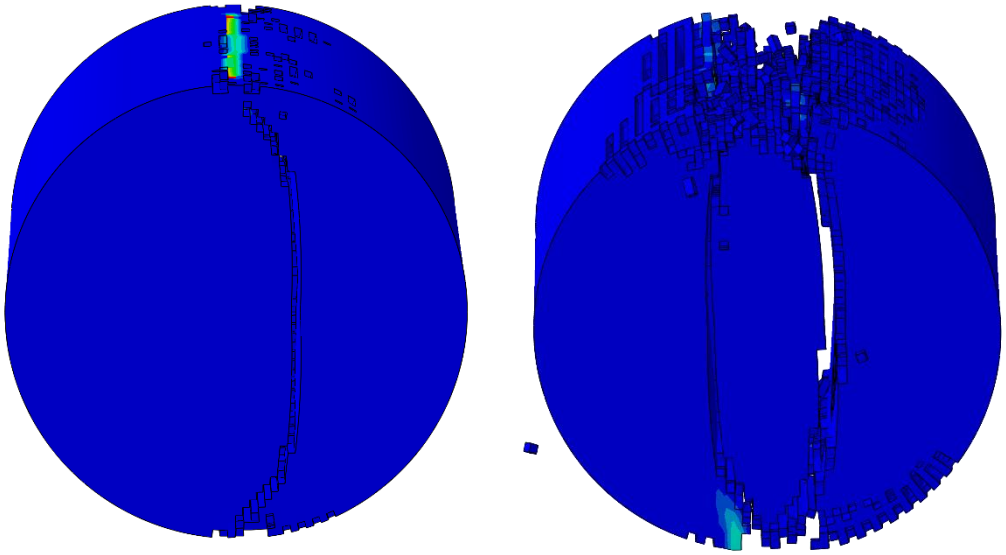

(c) Crack propagation and failure of material. (d) Final damaged specimen.

(e) Real failure of material. (f) Final real damaged specimen.

Figure V.16. Damage propagation until failure in simulation and experimental for quasi-static split compression test.

The stress-strain curve in Figure V.17 presents a comparison between the experimental results (S1, S2, and S3) and the simulation data for the same material under tensile loading. The plot effectively illustrates the material's response to increasing displacement, showing how the force builds up as the material is stretched, ultimately leading to failure.

The experimental data points (S1, S2, and S3) and the simulation curve closely align up to the maximum displacement of approximately 0.024 mm, with very small deviations between the curves. This close agreement suggests that the JH2 material model used in Abaqus accurately captures the tensile behavior of the material up to failure. The model reproduces both the elastic response and the linear behavior as the material approaches its strength limit. From 0 to 0.005 mm of displacement, the force increases linearly with displacement. This linear relationship indicates that both the simulation and experiments remain in the elastic region. The nearly perfect overlap of the simulation curve with the experimental data in this region validates the accuracy of the elastic modulus defined in the simulation model. Beyond 0.005 mm, the curve begins to deviate from linearity, signifying the onset of plastic deformation. At this stage, the material undergoes permanent deformation, and the force required to continue the deformation increases at a lower rate. The simulated curve captures this nonlinear behavior precisely, with excellent correlation to the experimental data (S1, S2, S3). This agreement indicates that the plasticity model in the simulation is well-calibrated, likely using appropriate yield stress and strain hardening parameters that reflect the actual material behavior.

Near the maximum displacement of 0.024 mm, the force peaks at around 3100 N. The experimental data points (S1, S2, S3) and the simulation both show similar peak force values, indicating that the simulation accurately predicts the material's tensile strength. Following the peak, the simulation indicates a rapid drop in force, represented by the sharp downward trend, which corresponds to material failure. This drop is typical of brittle materials, where failure occurs suddenly after reaching the maximum load. The consistency of the peak force values between the simulation and experiment is a strong indicator of the model's accuracy in predicting the failure behavior of the material.

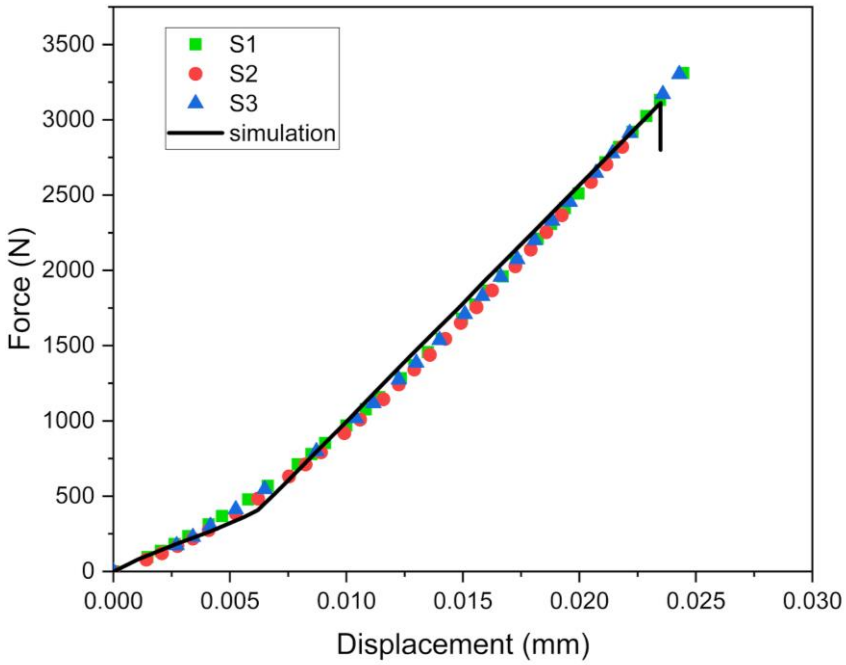

Figure V.17. Simulation and experimental stress strain curve of split tests.

Numerical and Experimental Investigation of Micromachining

In the second phase of the numerical simulation, the JH-2 model was applied to simulate the micro-milling process using Abaqus/Explicit. The workpiece was modeled with dimensions of 0.5 mm × 0.5 mm × 0.3 mm, with two different tool diameters, each performing a cutting depth of 10 µm. As illustrated in Figure V.18, a simplified 3D conception of the milling tool was used, focusing on its lower section. A refined mesh size of 0.005 mm was applied to the deformable region to capture fine details of the material behavior. Tool wear was considered to ensure consistency with experimental conditions.

The wear was observed only after extended cutting lengths, remaining negligible within the tested machining range. The tool was treated as a rigid body to reduce computational cost. The boundary conditions were set to fully constrain the bottom surface of the workpiece, preventing any movement in the X and Y directions, while allowing free displacement in the active milling direction, Z. A constant angular velocity of 30,000 RPM was applied to the tool to simulate the dynamic cutting motion along the specified path. This parameter was kept constant across all tests to eliminate any variability in tool speed. Additionally, an explicit dynamic analysis was employed to model the high-speed surface-to-surface interaction between the rigid tool and the workpiece, capturing the cutting forces and deformation behavior while incorporating the JH-2 material model to simulate damage evolution and fracture in the hard, brittle material. This setup provided a highly detailed representation of the micro-milling process, ensuring a balance between computational efficiency and accuracy while facilitating the validation of the model with the known behavior of brittle materials. To evaluate the accuracy and effectiveness of the JH-2 model in simulating the micro-milling process, we performed simulations using different milling parameters, starting by varying the feed rates (10 mm/min and 100 mm/min), the depth of cut (10 μm and 20 μm), and then the tool diameter (D= 0.2 mm and 0.4 mm). These varying parameters allowed us to assess the model's response to different cutting conditions, providing insight into how well the simulation captured the cutting forces, material deformation, and overall behavior under different machining scenarios.

Figure V.19 presents the evolution of the Von Mises stress distribution during the micro-milling process. The sequence of images captures the material response at different time steps, highlighting the development of localized stress concentrations at the tool-workpiece interface. As the tool advances, the stress levels increase near the cutting edge, particularly along the shear zones where material removal occurs. At later stages, stress redistribution is observed, leading to crack initiation within the brittle material. This visualization demonstrates the interplay between cutting forces and stress accumulation, providing insight into the material removal mechanisms governing the machining of BGO.

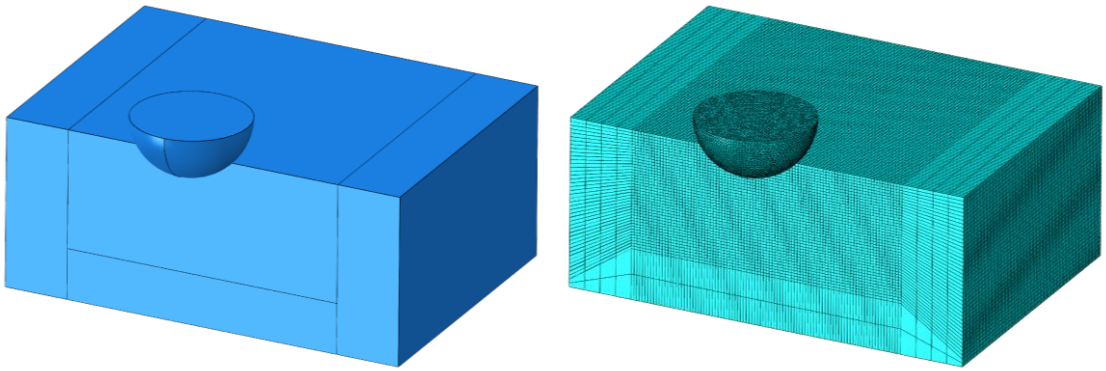

Figure V.18. The geometric structure and boundary condition of the three-dimensional (3D) finite element model (FEM) of the milling process.

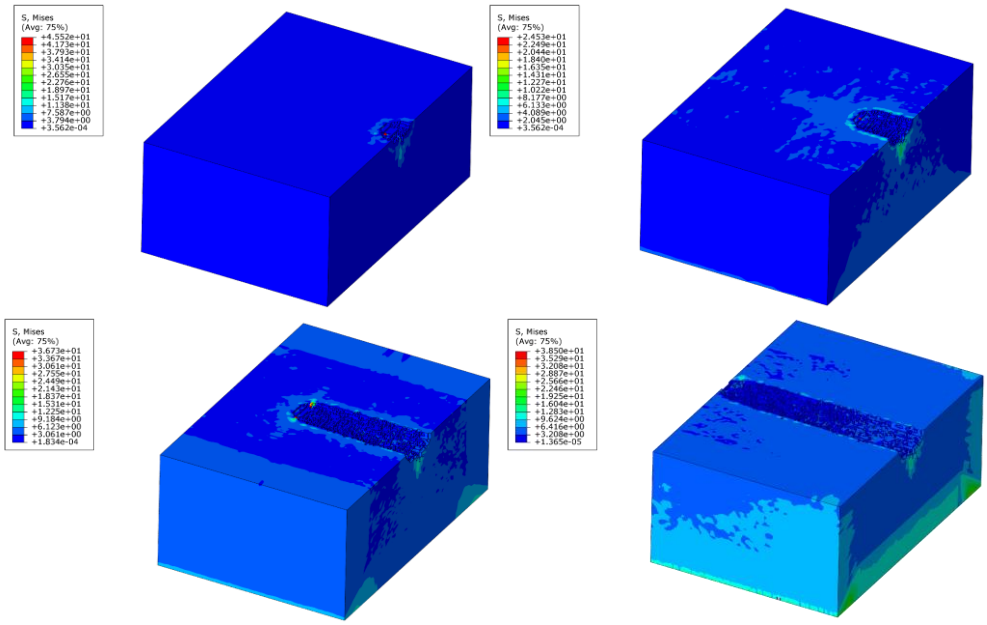

Figure V.19. Von mises variation during milling process at different times during machining.

Figure V.20 illustrates the impact of feed rate during the milling of BGO. At a lower feed rate of 10 mm/min, the milling process demonstrates enhanced stability, characterized by reduced cutting forces and minimal disturbance to the brittle material. As the feed rate increases to 100 mm/min, while maintaining constant milling conditions, there is a noticeable rise in dynamic force fluctuations, despite the overall cutting forces remaining low (below 0.03 N). This behavior aligns with established findings on machining brittle materials, where the feed rate plays a critical role in determining the quality of the finished surface.

Lower feed rates tend to produce finer surfaces by maintaining force stability, reducing crack propagation, and minimizing surface roughness, thus yielding a higher quality finish. Higher feed rates often introduce instability, adversely affecting surface integrity and increasing subsurface stress, and elevate the potential for defect propagation of structural damage to the brittle material [103-105].

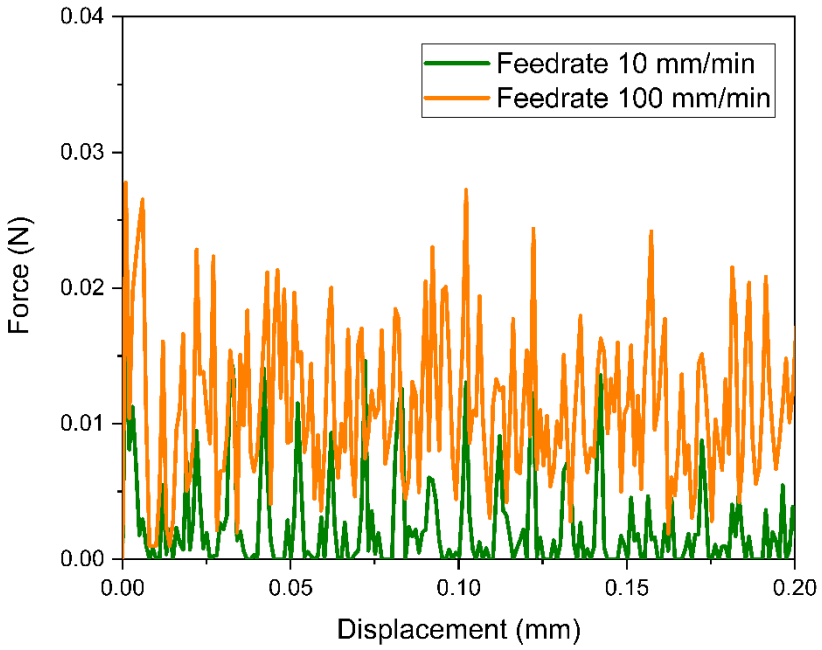

Figure V.20. Cutting force displacement curve of milling process using two different Feed rates.

Figure V.21 shows the impact of depth of cut during the milling of BGO. Increasing the depth of cut to 20 µm results in a significant rise in cutting forces. Deeper cuts generally produce higher forces, which in turn elevates the risk of fractures. The high fluctuations suggest that the material encounters localized stress concentrations exceeding its fracture toughness threshold, which can precipitate crack initiation and propagation within the machined surface. These findings align with prior studies on brittle materials, where maintaining a controlled depth of cut is essential to minimize subsurface damage, reduce crack formation, and achieve superior surface finish [103].

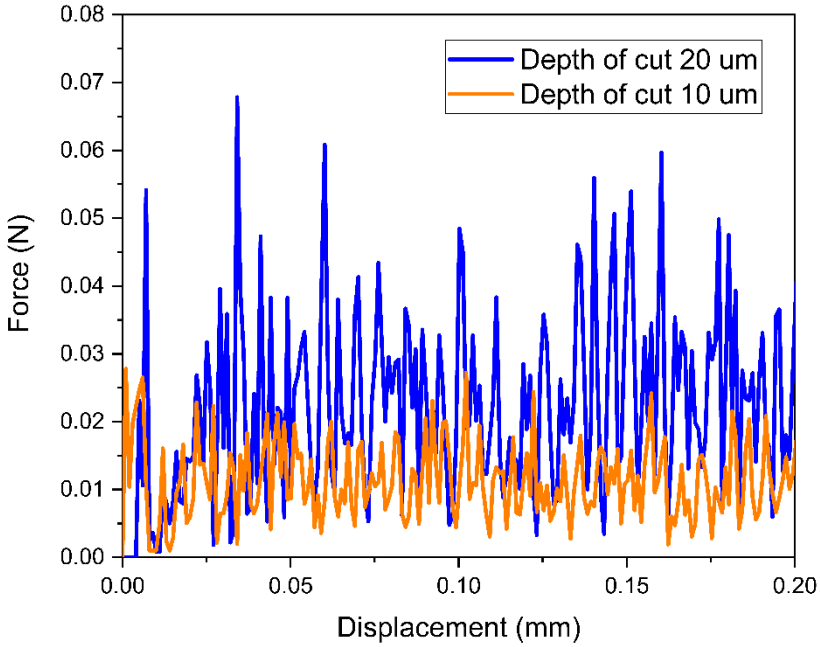

Figure V.21. Cutting force displacement curve of milling process using two different depth of cuts.

The use of a larger tool diameter (0.4 mm) results in more stable cutting forces compared to a smaller tool diameter (0.2 mm) under identical conditions. As shown in Figure V.22. Simulation results reveal that the 0.4 mm tool produces smoother force-displacement curves with fewer fluctuations, indicating a more consistent cutting process. This suggests that the larger diameter facilitates better force distribution under the given conditions, reducing the risk of sudden force spikes and potential brittle fractures. In contrast, the 0.2 mm tool diameter exhibits more force fluctuations and instability, increasing the risk of microcracking and surface roughness during milling. Overall, the larger tool diameter maintains a more stable interaction with the material, thereby minimizing the risk of force-induced damage [106,107].

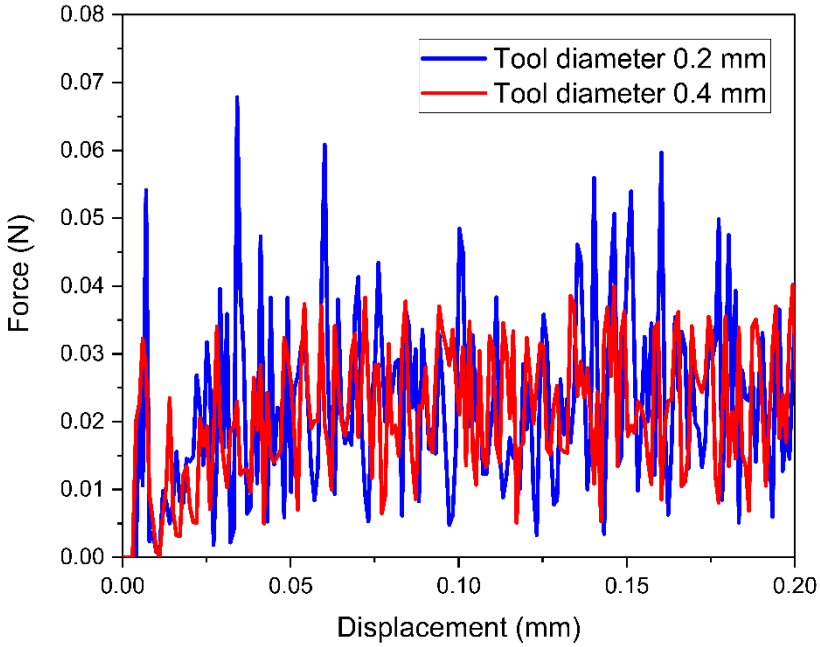

Figure V.22. Cutting force displacement curve of milling process using two different tool diameters.

IV.4. Conclusion

This chapter has explored the machinability of single- crystal Bismuth Germanate (BGO) under diverse micro-machining conditions, providing critical insights into its behavior as a brittle material used in high-precision applications. By varying key process parameters in the micro-milling and micro-drilling processes, we observed the material's response to different machining environments, confirming BGO's machinability across a range of conditions.

Detailed material characterization through quasi-static compression tests allowed for the accurate determination of the mechanical properties necessary for defining the Johnson-Holmquist 2 (JH-2) material model, which was subsequently integrated into finite element analysis (FEA) simulations using Abaqus. These simulations, designed to replicate quasi-static compression, splitting, and micromachining tests, were systematically compared with experimental data, leading to a robust validation of the JH-2 model for BGO.

The close agreement between the simulated and experimental results confirms the validity of the JH-2 model in capturing the key aspects of BGO's mechanical behavior under different machining regimes. The FEM model for BGO, validated through both literature and experimental results, confirms its reliability in predicting the effects of tool diameter, feed rate, and depth of cut during micro-milling.

The investigation of surface integrity confirmed that machining parameters critically influence surface morphology in BGO. Lower feed rates (10 mm/min) and larger tool diameters (0.4 mm) produced smooth, continuous machining tracks with minimal defects, while higher feed rates (100 mm/min) led to brittle fracture, chipping, and irregular tool marks, especially with the 0.2 mm tool. SEM analysis showed that controlled cutting conditions resulted in better surface quality, whereas excessive cutting forces caused surface damage and irregular machining patterns.

These findings emphasize the importance of optimized micro-milling parameters to achieve precision machining with minimal surface damage in BGO. The computational framework developed in this study can serve as a reference for exploring the machinability of other brittle scintillator materials, aiming to enhance the manufacturing of high-precision components for PET imaging and similar applications.

GENERAL CONCLUSION

GENERAL CONCLUSION

This doctoral thesis presented an extensive parametric and modeling study of ultra-precision machining processes applied to Bismuth Germanate (BGO), a brittle scintillator crystal widely used in Time-of-Flight Positron Emission Tomography (TOF-PET). The research was designed to address the core challenge of achieving optical-grade surface quality while minimizing machining-induced damage, essential for improving the timing resolution and light collection efficiency of TOF-PET detectors.

The experimental part of this study focused on a multi-stage material preparation sequence involving wire sawing, lapping, and mechanical polishing. A series of controlled tests, based on a Taguchi design of experiments, was conducted to optimize the polishing process. Three main parameters: abrasive grain size, applied pressure, and relative velocity, were investigated. The optimal combination resulted in a surface roughness of approximately 3.3 nm, which significantly enhanced the optical transmittance of BGO at the emission wavelength of 420 nm. This improvement directly contributes to better scintillation performance and increased detector efficiency in TOF-PET imaging systems.

Complementing the experimental investigations, a high-fidelity micromachining simulation framework was developed using the Johnson-Holmquist II (JH-2) material model in Abaqus/Explicit. The model was successfully validated against experimental results and was able to accurately predict cutting forces, stress distributions, and crack propagation under ultra-precision conditions. The simulation provided deep insight into the material's fracture behavior and response to machining at micro-scale, offering a valuable tool for virtual experimentation and predictive process optimization.

The dual approach adopted in this work, combining rigorous experimental characterization with robust numerical modeling enabled a detailed understanding of the interaction between process parameters and surface quality in brittle crystals. The findings offer a new benchmark for machining BGO and lay the groundwork for broader applications in precision optics and radiation detection.

Furthermore, the methodologies developed in this research are not limited to BGO. They can be extended to other scintillator and optical materials that require nanometric surface finishes and high optical transparency. The experimental techniques, statistical optimization

methods, and numerical simulation strategies established in this thesis constitute a comprehensive process for advancing ultra-precision manufacturing in high-performance optical and medical imaging components.

This work stands as a meaningful contribution to the fields of precision engineering, scintillator fabrication, and micro-scale modeling. It supports future developments in TOF-PET technology and sets the stage for more advanced processing of brittle materials where surface perfection is a critical performance criterion.

References

[1] Zhang, S., et al., A review of surface roughness generation in ultra-precision machining. International Journal of Machine Tools and Manufacture, 2015. 91: p. 76-95.

[2] Obata, K., Single-crystal diamond cutting tool for ultra-precision processing. SEI Tech. Rev, 2016. 82: p. 82-88.

[3] Lucca, D.A., M.J. Klopfstein, and O. Riemer, Ultra-precision machining: cutting with diamond tools. Journal of Manufacturing Science and Engineering, 2020 142(11): p. 110817.

[4] Kumar, A. and S.N. Melkote, Diamond wire sawing of solar silicon wafers: a sustainable manufacturing alternative to loose abrasive slurry sawing. Procedia Manufacturing, 2018. 21: p. 549-566.

[5] Gao, Y., et al., Material removal and surface generation mechanisms in diamond wire sawing of silicon crystal. Materials Science in Semiconductor Processing, 2019. 103: p. 104642.

[6] PU, Tianzhao, GAO, Yufei, WANG, Liyuan, et al. Experimental investigation on the machining characteristics of fixed-free abrasive combined wire sawing PV polycrystalline silicon solar cell. The International Journal of Advanced Manufacturing Technology, 2020, vol. 107, p. 843-858.

[7] Li, A., et al., Recent Advances in Precision Diamond Wire Sawing Monocrystalline Silicon. Micromachines, 2023. 14(8): p. 1512.

[8] Suzuki, T., Y. Nishino, and J. Yan, Mechanisms of material removal and subsurface damage in fixed-abrasive diamond wire slicing of single-crystalline silicon. Precision Engineering, 2017. 50: p. 32-43.

[9] Rahman, A.A., A. Mamat, and A. Wagiman, Effect of machining parameters on hole quality of micro drilling for brass. Modern applied science, 2009. 3(5): p. 221-230.

[10] Egashira, K. and K. Mizutani, Micro-drilling of monocrystalline silicon using a cutting tool. Precision Engineering, 2002. 26(3): p. 263-268.

[11] Pattanayak, S. and S. Panda, Laser beam micro drilling–a review. Lasers in Manufacturing and Materials Processing, 2018. 5(4): p. 366-394.

[12] Neugebauer, R. and A. Stoll, Ultrasonic application in drilling. Journal of materials processing technology, 2004. 149(1-3): p. 633-639.

[13] SINGH, Prithpal, PRAMANIK, A., BASAK, A. K., et al. Developments of non-conventional drilling methods—a review. The International Journal of Advanced Manufacturing Technology, 2020, vol. 106, no 5, p. 2133-2166.

[14] Hasan, M., J. Zhao, and Z. Jiang, A review of modern advancements in micro drilling techniques. J Manuf Process 29: 343–375. 2017.
[15] Hyacinth Suganthi, X., U. Natarajan, and N. Ramasubbu, A review of accuracy enhancement in microdrilling operations. The International Journal of Advanced Manufacturing Technology, 2015. 81(1-4): p. 199-217.
[16] Campanelli, S., et al., Experimental analysis of the laser milling process parameters. Journal of Materials Processing Technology, 2007. 191(1-3): p. 220-223.
[17] Hinduja, S. and J. Pattavanitch, Experimental and numerical investigations in electro-chemical milling. CIRP Journal of Manufacturing Science and Technology, 2016. 12: p. 79-89.
[18] Gomes, M.C., M.B. da Silva, and M.A.V. Duarte, Experimental study of micromilling operation of stainless steel. The International Journal of Advanced Manufacturing Technology, 2020. 111: p. 3123-3139.
[19] Wang, S., et al., A study of the fabrication of v-groove structure in ultra-precision milling. International Journal of Computer Integrated Manufacturing, 2014. 27(11): p. 986-996.
[20] Chen, N., et al., Advances in micro milling: From tool fabrication to process outcomes. International Journal of Machine Tools and Manufacture, 2021. 160: p. 103670.
[21] O'Toole, L., C.-W. Kang, and F.-Z. Fang, Precision micro-milling process: state of the art. Advances in Manufacturing, 2021. 9: p. 173-205.
[22] Huang, W. and J. Yan, Effect of tool geometry on ultraprecision machining of soft-brittle materials: a comprehensive review. International Journal of Extreme Manufacturing, 2023. 5(1): p. 012003.
[23] Azizur Rahman, M., M. Rahman, and A. Senthil Kumar, Influence of relative tool sharpness (RTS) on different ultra-precision machining regimes of Mg alloy. The International Journal of Advanced Manufacturing Technology, 2018. 96: p. 3545-3563.
[24] Arif, M., M. Rahman, and W.Y. San, A study on the effect of tool-edge radius on critical machining characteristics in ultra-precision milling of tungsten carbide. The International Journal of Advanced Manufacturing Technology, 2013. 67: p. 1257-1265.
[25] ARAMCHAROEN, A. et MATIVENGA, P. T. Size effect and tool geometry in micromilling of tool steel. Precision Engineering, 2009, vol. 33, no 4, p. 402-407.
[26] Ruibin, X. and H. Wu, Study on cutting mechanism of Ti6Al4V in ultra-precision machining. The International Journal of Advanced Manufacturing Technology, 2016. 86: p. 1311-1317.

[27] Kwok, T., et al., Analysis of surface generation in ultra-precision machining with a fast tool servo. Proceedings of the Institution of Mechanical Engineers, Part B: Journal of Engineering Manufacture, 2010. 224(9): p. 1351-1367.
[28] MEIJER, Alexander, KREBS, Eugen, WIEDERKEHR, Petra, et al. Prediction of feed-rate slowdowns in precise micromilling processes. Journal of Manufacturing and Materials Processing, 2018, vol. 2, no 1, p. 19.
[29] Shanshan, C., et al., Theoretical and experimental investigation of a tool path control strategy for uniform surface generation in ultra-precision grinding. The International Journal of Advanced Manufacturing Technology, 2019. 103: p. 4307-4315.
[30] Wang, S., et al., An integrated optimization of cutting parameters and tool path generation in ultraprecision raster milling. The International Journal of Advanced Manufacturing Technology, 2014. 75: p. 1711-1721.
[31] Gong, H., et al., Tool path generation of ultra-precision diamond turning: A state-of-the-art review. Nanotechnology and Precision Engineering (NPE), 2019. 2(3): p. 118-124.
[32] Brinksmeier, E., O. Riemer, and J. Osmer, Tool path generation for ultra-precision machining of free-form surfaces. Production Engineering, 2008. 2(3): p. 241-246.
[33] KIM, Chang-Ju, BONO, Matthew, NI, Jun, et al. Experimental analysis of chip formation in micro-milling. TECHNICAL PAPERS-SOCIETY OF MANUFACTURING ENGINEERS-ALL SERIES-, 2002.
[34] Evans, C., et al., Material removal mechanisms in lapping and polishing. CIRP annals, 2003. 52(2): p. 611-633.
[35] Lee, H., B. Park, and H. Jeong, Influence of slurry components on uniformity in copper chemical mechanical planarization. Microelectronic Engineering, 2008. 85(4): p. 689-696.
[36] Basim, G., et al., Effect of particle size of chemical mechanical polishing slurries for enhanced polishing with minimal defects. Journal of the Electrochemical Society, 2000. 147(9): p. 3523.
[37] Tsai, M.Y. and W.K. Chen, Effect of CMP conditioner diamond shape on pad topography and oxide wafer performances. The International Journal of Advanced Manufacturing Technology, 2011. 55: p. 253-262.
[38] Seo, J., A review on chemical and mechanical phenomena at the wafer interface during chemical mechanical planarization. Journal of Materials Research, 2021. 36: p. 235-257.
[39] Khatri, N., et al., An experimental study on the effect of magneto-rheological finishing on diamond turned surfaces. Journal of intelligent material systems and structures, 2014. 25(13): p. 1631-1643.

[40] Iqbal, F. and S. Jha, Experimental investigations into transient roughness reduction in ball-end magneto-rheological finishing process. Materials and Manufacturing Processes, 2019. 34(2): p. 224-231.
[41] Singh, A.K., S. Jha, and P.M. Pandey, Mechanism of material removal in ball end magnetorheological finishing process. Wear, 2013. 302(1-2): p. 1180-1191.
[42] Mali, H. and A. Manna, Current status and application of abrasive flow finishing processes: a review. Proceedings of the Institution of Mechanical Engineers, Part B: Journal of Engineering Manufacture, 2009. 223(7): p. 809-820.
[43] Sankar, M.R., V. Jain, and J. Ramkumar, Experimental investigations into rotating workpiece abrasive flow finishing. Wear, 2009. 267(1-4): p. 43-51.
[44] Sankar, M.R., J. Ramkumar, and V. Jain, Experimental investigation and mechanism of material removal in nano finishing of MMCs using abrasive flow finishing (AFF) process. Wear, 2009. 266(7-8): p. 688-698.
[45] Yuan, J., et al., Review on the progress of ultra-precision machining technologies. Frontiers of mechanical engineering, 2017. 12: p. 158-180.
[46] YAMAGUCHI, Mitsugu, FURUMOTO, Tatsuaki, INAGAKI, Shuuji, et al. Internal face finishing for a cooling channel using a fluid containing free abrasive grains. The International Journal of Advanced Manufacturing Technology, 2021, vol. 114, p. 497-507.
[47] Luo, X., W. Yang, and Y. Qian, Fixed abrasive polishing: The effect of particle size on the workpiece roughness and sub-surface damage. The International Journal of Advanced Manufacturing Technology, 2021. 115(9-10): p. 3021-3035.
[48] Zhu, H., et al., The effect of abrasive hardness on the chemical-assisted polishing of (0001) plane sapphire. Journal of materials research, 2005. 20(2): p. 504-520.
[49] Liu, N., et al., Effects of polishing pressure and sliding speed on the material removal mechanism of single crystal diamond in plasma-assisted polishing. Diamond and Related Materials, 2022. 124: p. 108899.
[50] Lee, E.S., et al., Study on the effect of various machining speeds on the wafer polishing process. Journal of Mechanical Science and Technology, 2013. 27: p. 3155-3160.
[51] Li, Z., Z. Deng, and Y. Hu, Effects of polishing parameters on surface quality in sapphire double-sided CMP. Ceramics International, 2020. 46(9): p. 13356-13364.
[52] Wang, S., et al., Effect of cutting parameters on heat generation in ultra-precision milling of aluminum alloy 6061. The International Journal of Advanced Manufacturing Technology, 2015. 80: p. 1265-127.

[53] FARH, Hassan M. Hussein, SEGHIER, Mohamed El Amine Ben, et ZAYED, Tarek. A comprehensive review of corrosion protection and control techniques for metallic pipelines. Engineering Failure Analysis, 2023, vol. 143, p. 106885.
[54] HASHMI, M. Saleem J. Comprehensive materials processing. Newnes, 2014.
[55] OLANIYAN, Tirimisiyu, FAISAL, Nadimul, et NJUGUNA, James. Recent Developments in Mechanical Ultraprecision Machining for Nano/Micro Device Manufacturing. Micromachines, 2024, vol. 15, no 8, p. 1030.
[56] Bhushan, B., Surface roughness analysis and measurement techniques, in Modern tribology handbook, two volume set. 2000, CRC press. p. 79-150.
[57] MESSINESE, Elena, CASANOVA, Luca, PATERLINI, Luca, et al. A comprehensive investigation on the effects of surface finishing on the resistance of stainless steel to localized corrosion. Metals, 2022, vol. 12, no 10, p. 1751.
[58] GADELMAWLA, Elamir S., KOURA, Monir M., MAKSOUD, Talal MA, et al. Roughness parameters. Journal of materials processing Technology, 2002, vol. 123, no 1, p. 133-145.
[59] Gong, Y., J. Xu, and R.C. Buchanan, Surface roughness: A review of its measurement at micro-/nano-scale. Physical Sciences Reviews, 2018. 3(1): p. 20170057.
[60] Grochalski, K., et al., Differences in Roughness Parameter Values from Skid and Skidless Contact Stylus Profilometers. Advances in Science and Technology. Research Journal, 2021. 15(1): p. 58-70.
[61] SUSHIL, K., RAMKUMAR, J., et CHANDRAPRAKASH, C. Surface roughness analysis: A comprehensive review of measurement techniques, methodologies, and modeling. Journal of Micromanufacturing, 2025, p. 25165984241305225.
[62] LIU, Hao, ZHANG, Jianqiu, JIANG, Qinghong, et al. Material Removal Mechanisms in Ultra-High-Speed Machining. Engineering, 2025.
[63] MENG, Fanzhen, ZHOU, Hui, ZHANG, Chuanqing, et al. Evaluation methodology of brittleness of rock based on post-peak stress–strain curves. Rock Mechanics and Rock Engineering, 2015, vol. 48, p. 1787-1805.
[64] HUANG, Shizhan, JIANG, Feng, ZHANG, Tao, et al. Advances in polycrystalline diamond (PCD) micro drills for efficient micro-hole machining in hard-brittle materials: a review of design, fabrication, and performance. Materials and Manufacturing Processes, 2025, vol. 40, no 1, p. 117-143.
[65] SOLEIMAN DEHKORDI, M., LAZEMI, H. A., et SAEEDMODAGHEGH, H. R. Estimation of the drop modulus using the brittleness index of intact rock and geological strength

index of rock mass, case studies: Nosoud and Zagros tunnels in Iran. Modeling Earth Systems and Environment, 2019, vol. 5, no 2, p. 479-492.
[66] OLANIYAN, Tirimisiyu, FAISAL, Nadimul, et NJUGUNA, James. Recent Developments in Mechanical Ultraprecision Machining for Nano/Micro Device Manufacturing. Micromachines, 2024, vol. 15, no 8, p. 1030.
[67] MAMEDOV, Ali, DINC, Ali, GULER, Mehmet Ali, et al. Tool wear in micromilling: a review. The International Journal of Advanced Manufacturing Technology, 2025, p. 1-19.
[68] A. Mamedov, Machining of brittle materials: micro milling of glass, J. Mech. Sci. Technol. 35 (9) (2021) 4143–4148.
[69] GROEB, Marvin, HAGELÜKEN, Lorenz, GROEB, Johann, et al. Experimental Analysis of Ductile Cutting Regime in Face Milling of Sintered Silicon Carbide. Materials, 2022, vol. 15, no 7, p. 2409.
[70] QI, Huan, SHI, Liwu, TENG, Qi, et al. Subsurface damage evaluation in the single abrasive scratching of BK7 glass by considering coupling effect of strain rate and temperature. Ceramics International, 2022, vol. 48, no 6, p. 8661-8670.
[71] ZHANG, Tao, JIANG, Feng, HUANG, Hui, et al. Towards understanding the brittle–ductile transition in the extreme manufacturing. International Journal of Extreme Manufacturing, 2021, vol. 3, no 2, p. 022001.
[72] ANTWI, Elijah Kwabena, LIU, Kui, et WANG, Hao. A review on ductile mode cutting of brittle materials. Frontiers of Mechanical Engineering, 2018, vol. 13, p. 251-263.
[73] SHEN, Jian, LIU, Shouhua, YI, Kui, et al. Subsurface damage in optical substrates. Optik, 2005, vol. 116, no 6, p. 288-294.
[74] GU, Yan, ZHU, Wenhui, LIN, Jieqiong, et al. Subsurface damage in polishing process of silicon carbide ceramic. Materials, 2018, vol. 11, no 4, p. 506.
[75] MEDEL-RUIZ, Carlos Israel, CHIU, Roger, SEVILLA-ESCOBOZA, Jesús Ricardo, et al. Nanoscale Surface Roughness Effects on Photoluminescence and Resonant Raman Scattering of Cadmium Telluride. Applied Sciences, 2024, vol. 14, no 17, p. 7680.
[76] CAO, Hongbing, PENG, Xing, SHI, Feng, et al. Advances in Subsurface Defect Detection Techniques for Fused Silica Optical Components: A Literature Review. Journal of Materials Research and Technology, 2025.
[77] Bar-Shalom, R., A.Y. Valdivia, and M.D. Blaufox. PET imaging in oncology. in Seminars in nuclear medicine. 2000. Elsevier.
[78] Saha, G.B., Basics of PET imaging: physics, chemistry, and regulations. 2015: Springer.

[79] Alauddin, M.M., Positron emission tomography (PET) imaging with 18F-based radiotracers. American journal of nuclear medicine and molecular imaging, 2012. 2(1): p. 55.
[80] Herrmann, K., et al., Imaging gastric cancer with PET and the radiotracers 18F-FLT and 18F-FDG: a comparative analysis. Journal of nuclear medicine, 2007. 48(12): p. 1945-1950.
[81] Townsend, D., Physical principles and technology of clinical PET imaging. Annals-Academy of Medicine Singapore, 2004. 33(2): p. 133-145.
[82] Al-Sharify, Z.T., T.A. Al-Sharify, and N.T. Al-Sharify. A critical review on medical imaging techniques (CT and PET scans) in the medical field. in IOP Conference Series: Materials Science and Engineering. 2020. IOP Publishing.
[83] Vandenberghe, S., et al., Recent developments in time-of-flight PET. EJNMMI physics, 2016. 3: p. 1-30.
[84] Surti, S., Update on time-of-flight PET imaging. Journal of Nuclear Medicine, 2015. 56(1): p. 98-105.
[85] Karp, J.S., et al., Benefit of time-of-flight in PET: experimental and clinical results. Journal of Nuclear Medicine, 2008. 49(3): p. 462-470.
[86] Yanagida, T., Inorganic scintillating materials and scintillation detectors. Proceedings of the Japan Academy, Series B, 2018. 94(2): p. 75-97.
[87] Melcher, C.L., Scintillation crystals for PET. Journal of Nuclear Medicine, 2000. 41(6): p. 1051-1055.
[88] Tessitore, G., et al., The role of lanthanide luminescence in advancing technology. RSC advances, 2023. 13(26): p. 17787-17811.
[89] Rogers, E.G., et al., Two-dimensional perovskite functionalized fiber-type heterostructured scintillators. Applied Physics Letters, 2023. 122(8).
[90] Krause, P., E. Rogers, and G. Bizarri, Advances in Design of High-Performance Heterostructured Scintillators for Time-of-Flight Positron Emission Tomography. Advanced Theory and Simulations, 2023: p. 2300425.
[91] Mohr, P., et al., Image reconstruction analysis for positron emission tomography with heterostructured scintillators. IEEE Transactions on Radiation and Plasma Medical Sciences, 2022. 7(1): p. 41-51.
[92] Krause, P., et al., Design rules for time of flight Positron Emission Tomography (ToF-PET) heterostructure radiation detectors. Heliyon, 2022. 8(6).
[93] Pagano, F., et al., Advances in heterostructured scintillators: toward a new generation of detectors for TOF-PET. Physics in Medicine & Biology, 2022. 67(13): p. 135010.

[94] Orfano, M., et al., Fast emitting nanocomposites for high-resolution ToF-PET imaging based on multicomponent scintillators. arXiv preprint arXiv:2309.14968, 2023.
[95] MAJORANA, E., RAPAGNANI, Piero, RICCI, Fulvio, et al. Anelastic and elastic properties of a synthetic monocrystal of bismuth germanate Bi4Ge3O12 at low temperatures. Journal of alloys and compounds, 1994, vol. 211, p. 640-643.
[96] SURUCU, Gokhan, ISIK, Mehmet, GENCER, Aysenur, et al. Experimental and theoretical investigation of the mechanical characteristics of sillenite compound: Bi12GeO20. Journal of Alloys and Compounds, 2021, vol. 882, p. 160686.
[97] G.R. Johnson, T.J. Holmquist, An improved computational constitutive model for brittle materials, in: AIP conference proceedings, 309, American Institute of Physics, 1994, July, pp. 981–984.
[98] Q. Fu, Y. Wang, R. An, Z. Xin, X. Cheng, J. Zhang, A possible mechanism for the difference in ballistic performance between sapphire and spinel, J. Eur. Ceram. Soc. 43 (14) (2023) 6234–6246.
[99] D.S. Cronin, K. Bui, C. Kaufmann, G. McIntosh, T. Berstad, D. Cronin, Implementation and validation of the Johnson-Holmquist ceramic material model in LS-Dyna, Proc. 4th Eur. LS-DYNA Users Conf. 1 (2003) 47–60.
[100] G.I. Kanel, S.J. Bless, A.M. Rajendran, Institute for Advanced Technology, The University of Texas at Austin. Behavior of brittle materials under dynamic loading, Tech. Rep. IAT. R, 2000, p. 219.
[101] P. Baranowski, M. Kucewicz, J. Janiszewski, JH-2 constitutive model of sandstone for dynamic problems, Sci. Rep. 14 (1) (2024) 3339.
[102] R. Zhang, P.Y. Li, X.D. Zhi, Y.H. Wang, F. Fan, Johnson–Holmquist-II model of annealed glass and its verification in dynamic compression test, in: Structures, 53, Elsevier, 2023, pp. 396–407.
[103] A. Mamedov, Machining of brittle materials: micro milling of glass, J. Mech. Sci. Technol. 35 (9) (2021) 4143–4148.
[104] M. Groeb, L. Hagelüken, J. Groeb, W. Ensinger, Experimental analysis of ductile cutting regime in face milling of sintered silicon carbide, Materials 15 (7) (2022) 2409.
[105] H. Qi, L. Shi, Q. Teng, T. Hong, V. Tangwarodomnukun, G. Liu, H.N. Li, Subsurface damage evaluation in the single abrasive scratching of BK7 glass by considering coupling effect of strain rate and temperature, Ceram. Int. 48 (6) (2022) 8661–8670.

[106] S.M. Afazov, D. Zdebski, S.M. Ratchev, J. Segal, S. Liu, Effects of micro-milling conditions on the cutting forces and process stability, J. Mater. Process. Technol. 213 (5) (2013) 671–684.
[107] J. Munoa, M. Zatarain, I. Bediaga, Determination of the cutting performance and dynamic behaviour of universal milling machines by means of a stability model, ISMA2006-Int. Conf. Noise Vib. Eng. (2006) 3789–3804.

الملخص: تتناول هذه الرسالة موضوع التشغيل فائق الدقة لبلورات الجرمانيوم البزموثي(BGO) ، وهي مادة هشة تُستخدم كمكون أساسي في كواشف التصوير المقطعي بالإصدار البوزيتروني مع قياس زمن الرحلة .(TOF-PET) ونظرًا لصلابتها وضعف متانتها ضد الكسر، تواجه هذه المادة تحديات كبيرة أثناء عمليات التشغيل الميكروي .تم تطوير منهجية تجمع بين التجارب العملية والنمذجة العددية. خضعت عينات BGO لعمليات تحضير ميكانيكي وتلميع، حيث تم دراسة تأثير حجم الحبيبات الكاشطة والضغط والسرعة على خشونة السطح وشفافية الضوء. وقد تم إثبات وجود علاقة قوية بين جودة السطح وتحسين نفاذية الضوء . كما تم إنشاء نموذج محاكاة باستخدام طريقة العناصر المحدودة اعتمادًا على نموذج Johnson-Holmquist II (JH-2) لمحاكاة سلوك القطع، وتمت مقارنته بنتائج تجارب الحفر والطحن الميكروي للتحقق من دقته. تناولت الدراسة آليات إزالة المادة، قوى القطع، وانتقال المادة من السلوك الهش إلى السلوك اللدن .تُقدم هذه النتائج توجيهات واضحة لتقليل تلف التشغيل وتحسين أداء مادة BGO في أنظمة .TOF-PET وتسهم هذه الدراسة في تطوير تقنيات التصنيع الدقيق للمواد الهشة وهو عم التقدم في تقنيات التصوير الطبي.

الكلمات المفتاحية: التشغيل فائق الدقة، الجرمانيوم البزموثي، خشونة السطح، النفاذية البصرية، التلميع الميكانيكي، المواد الوماضة، النمذجة بالعناصر المحدودة، التصوير المقطعي بالإصدار البوزيتروني وقت الطيران

Abstract: This thesis investigates the ultra-precision machining of **brittle Bismuth Germanate (BGO) single crystals,** a key material in **Time-of-Flight Positron Emission Tomography (TOF-PET)** detectors. Due to its hardness and low fracture toughness, BGO presents significant challenges during micromachining. A combined **experimental and numerical approach** was developed. Mechanically prepared BGO samples underwent **polishing process**, evaluating the effects of abrasive size, pressure, and speed on surface roughness and optical transmittance. A strong link was established between improved surface quality and enhanced light transmission. To model BGO's cutting behavior, a **finite element simulation using the Johnson-Holmquist II (JH-2) model** was implemented and validated with micro-milling and drilling experiments. The study analyzed material removal mechanisms, cutting forces, and the brittle-to-ductile transition. The results offer clear guidelines for minimizing machining damage and improving BGO performance in TOF-PET systems. This work contributes to precision manufacturing of brittle materials and supports advancements in medical imaging technologies.

Keywords: ultra-precision machining, Bismuth Germanate (BGO), surface roughness, optical transmittance, mechanical polishing, scintillator materials, finite element modeling, Time-of-Flight Positron Emission Tomography (TOF-PET).

Résumé : Cette thèse porte sur l'usinage ultra-précis du germanate de bismuth (BGO), un cristal monocristallin fragile largement utilisé comme scintillateur dans les détecteurs Time-of-Flight en tomographie par émission de positons (TOF-PET). En raison de sa dureté et de sa faible ténacité à la rupture, le BGO présente d'importants défis en micromécanique. Une approche combinant expérimentations et modélisation numérique a été développée. Des échantillons de BGO ont été préparés mécaniquement, puis soumis à un processus de polissage, en évaluant l'effet de la taille des abrasifs, de la pression et de la vitesse sur la rugosité de surface et la transmission optique. Un lien fort a été établi entre la qualité de surface et l'amélioration de la transmission lumineuse. Le comportement d'usinage du BGO a été modélisé à l'aide d'une simulation par éléments finis basée sur le modèle Johnson-Holmquist II (JH-2), validée par des expériences de micro-fraisage et de micro-perçage. L'étude a permis d'analyser les mécanismes d'enlèvement de matière, les forces de coupe et la transition fragile-ductile. Les résultats offrent des recommandations claires pour limiter les dommages d'usinage et améliorer les performances du BGO dans les systèmes TOF-PET. Ce travail contribue à la fabrication de précision des matériaux fragiles et à l'amélioration des technologies d'imagerie médicale.

Mots-clés: usinage ultra-précis, germanate de bismuth (BGO), rugosité de surface, transmittance optique, polissage mécanique, matériaux scintillateurs, modélisation par éléments finis, tomographie par émission de positons (TOF-PET)